CONFORMAL RADIOSURGERY AND RADIOTHERAPY PLANNING USING INTENSITY MODULATED PHOTON BEAMS

By

SANFORD L. MEEKS

A DISSERTATION PRESENTED TO THE GRADUATE SCHOOL
OF THE UNIVERSITY OF FLORIDA IN PARTIAL FULFILLMENT
OF THE REQUIREMENTS FOR THE DEGREE OF
DOCTOR OF PHILOSOPHY

UNIVERSITY OF FLORIDA

1994

LD
1780
1994
.M494

ACKNOWLEDGEMENTS

I would like to express my sincere appreciation for the guidance provided by the members of my supervisory committee. Special thanks are due to my committee chairman, Dr. Frank Bova, who has taught me a great deal about medical physics, and whom I will always respect and admire. I would also like to thank the Nomos corporation for its support, and its technical staff for assisting me overcome numerous obstacles caused by computer and/or operator error. I am also grateful to Dr. John Buatti, Dr. Gerald Kutcher and Dr. Andrzej Niemerko for insightful discussions regarding the dose-response modelling required for quantitative plan comparisons, and Dr. John Buatti, Dr. Yvonne Mack, Dr. William Mendenhall and Dr. Robert Zlotecki for assistance with delineation of target volumes. Finally, I would like to thank all of my family, friends and co-workers who have supported me emotionally and helped make this work enjoyable. In particular, I would like to thank my parents for their gentle prodding throughout my educational experience, and my wife, Allyson, for her patience and also for allowing me the greatest joy I've ever known by giving me a son, Alton.

TABLE OF CONTENTS

ACKNOWLEDGEMENTS ii

ABSTRACT v

CHAPTERS

1 INTRODUCTION 1

Conventional External Beam Radiotherapy 1
Stereotactic Radiosurgery 2
Conformal Radiotherapy 3

2 REVIEW OF THE LITERATURE 9

Inverse Radiotherapy Planning Algorithms 9
Clinical Treatment Planning Studies 21

3 UNIVERSITY OF FLORIDA TREATMENT PLANNING 27

Conventional Treatment Planning 27
Three Dimensional Planning (Virtual Simulation) 30
Stereotactic Radiosurgery Treatment Planning 31

4 INVERSE RADIOTHERAPY TREATMENT PLANNING 37

MIMIC 37
Peacock Plan™ 41
Verification of Dosimetry Algorithm 47

5 TECHNIQUES FOR QUANTITATIVE PLAN EVALUATION 52

Dose Volume Histograms 52
Normal Tissue Complication Probability 56
Tumor Control Probability 60
Dosimetric Statistics 64
Biologically Normalized Dose Fractionation 65

Score Functions 67
Delivery Efficiency 68

6 CLINICAL TREATMENT PLANNING STUDIES 69

Stereotactic Radiosurgery Patients 73
Head and Neck Carcinomas 93
Intact Breast 94
Lung Cancer 96
Carcinoma of the Prostate 98
Discussion 99

7 PHYSICAL REQUIREMENTS OF INTENSITY MODULATION DEVICE 130

Computer Simulation of Intensity Modulator 130
Derivation of Semiempirical Dose Model 131
Description of Computer Algorithm 136
Vane Width 137
Step Resolution 145
Clinical Resolution Requirements 152

8 CLINICAL EFFICACY OF TOMOTHERAPY 171

9 THE EFFECT OF RANDOM POSITIONAL ERRORS ON INVERSE RADIOTHERAPY PLANS 189

10 DISCUSSION 199

APPENDICES

A CALCULATION OF NORMAL TISSUE COMPLICATION PROBABILITY 209

B CALCULATION OF TUMOR CONTROL PROBABILITY 222

C OPTIMIZATION OF INTENSITY MODULATION FUNCTIONS . . . 236

REFERENCES 263

BIOGRAPHICAL SKETCH 272

Abstract of Dissertation Presented to the Graduate School
of the University of Florida in Partial Fulfillment of the
Requirements for the Degree of Doctor of Philosophy

CONFORMAL RADIOSURGERY AND RADIOTHERAPY PLANNING USING INTENSITY MODULATED PHOTON BEAMS

By

Sanford L. Meeks

December 1994

Chairperson: Frank J. Bova, Ph.D.
Major Department: Nuclear Engineering Sciences

This paper investigates the efficacy of inverse radiosurgery and radiotherapy planning in the clinical environment. Inverse radiotherapy plans were generated for patients with lesions at various anatomical sites using the Peacock treatment planning system, which determines the optimal conformal radiotherapy plan through backprojection and simulated annealing. These treatment plans were then compared to two- and/or three-dimensional conventional treatment plans generated for actual patient treatment. Plan comparisons were accomplished through conventional qualitative review of two-dimensional dose distributions in conjunction with quantitative techniques such as dose volume histograms, dosimetric statistics, normal tissue complication probabilities, tumor control probabilities, numerical scoring and treatment delivery efficiency. The physical limitations of modulation devices based on multileaf collimators were studied through computer simulation of these devices in addition to examination of their utility in the clinical environment. Other treatment parameters which affect the clinical efficacy of conformal radiotherapy plans that were also studied include the use of noncoplanar beams versus single arc conformal therapy (tomotherapy) and uncertainty in patient positioning.

CHAPTER 1
INTRODUCTION

Conventional External Beam Radiotherapy

Radiation therapy is a clinical specialty devoted to the treatment of patients with malignant or benign neoplasms through the use of ionizing radiation. The primary goal of radiotherapy is to deliver a therapeutic dose to the targeted lesion with minimal dose to surrounding normal tissue, resulting in uncomplicated eradication of the tumor. Unfortunately, the dose required for tumor control often leads to a finite probability of undesirable side effects in normal tissue. Nonetheless, radiation therapy is an appealing alternative to surgery in many instances where surgical resection may produce unacceptable anatomical, physiological or cosmetic results or for extensive lesions that cannot be surgically resected. Radiotherapy also serves as a powerful adjunct to other treatment modalities such as surgery and chemotherapy. Radiotherapy is often used preoperatively to shrink the tumor prior to resection, or alternatively, postoperatively in order to eradicate microscopic disease left in the area of the gross tumor. Similarly, chemotherapy is used in conjunction with radiation therapy in order to reduce the initial number of clonogenic cells before irradiation, or to eradicate distant metastases which may not be within the irradiated volume [Per92].

Radiation was first used for cancer treatment by Grubbe in 1896, shortly after Roentgen's discovery of x rays in 1895 and the Curies' discovery of radium in 1896

[Wal88]. Technological advances in radiotherapy equipment have accrued steadily since that initial experience with improved x-ray generators followed by cyclotrons, synchocyclotrons, betatrons and linear accelerators [Per92]. Modern radiotherapy relies primarily on high energy gamma rays from ^{60}Co beams and high energy x rays and electrons produced by linear accelerators, although other particulate and electromagnetic irradiations are frequently utilized.

Stereotactic Radiosurgery

Stereotactic radiosurgery is a technique in which small focused beams of radiation are utilized to treat intracranial targets. Radiosurgery is an attractive treatment modality because it can be used to treat patients who have lesions which are not suitable for conventional neurosurgical techniques, there is little risk of infection or hemorrhage, and the procedure may be performed quickly on an outpatient basis [Win88]. At the University of Florida, arteriovenous malformations are the most common lesions treated with stereotactic radiosurgery, but a variety of solid lesions exist which are suitable for treatment by radiosurgery. These include pituitary tumors, pinealomas, acoustic neuromas, small malignant neoplasms and craniopharyngiomas [Fri89].

Stereotactic radiosurgery was first described by Lars Leksell of the Karolinska Hospital in 1951. He first experimented with the use of finely collimated beams of 200 kVp x rays, but it was clear that higher energy radiation should be utilized [Lek51]. With the help of two physicists, Kurt Liden and Borje Larsson, Leksell experimented with the use of proton beams and linear accelerators, but he decided these devices were inadequate for radiosurgery. He and his coworkers then developed the Gamma Knife™, which uses multiple ^{60}Co sources focused at a central point [Lek83]. Using the Leksell Gamma Unit, these and other researchers have reported impressive control rates for a variety of small lesions [Lek87]. This high rate of success has been limited to small targets, however, since the maximum Gamma Knife field size has an 18 mm diameter. Since the average radiosurgery is approximately 24 mm, larger targets are treated with many small shots from the Gamma Knife. The overlap of these small circular shots can lead to an undesirable large dose inhomogeneity within the targeted region. In spite of this success, the Gamma Knife is not practical for use in most radiotherapy clinics since it is a costly dedicated unit with two hundred one ^{60}Co sources which must be maintained and periodically reloaded.

In order to construct an effective radiosurgical system that would be less expensive yet flexible, researchers investigated the use of linear accelerators. These systems utilize multiple noncoplanar arcs of radiation which intersect at the target to achieve a steep dose gradient outside of the target. This allows one to achieve a high dose within the targeted region while maintaining minimal dose to normal tissues outside of the target [Fri92]. One such system has been developed at the University of Florida by Friedman and Bova. This system has the highest proven treatment accuracy of the linac systems currently used. It has a radiation beam accuracy of 0.2 ± 0.1 mm [Fri89].

Conformal Radiotherapy

In order to reduce toxicity to normal tissues from radiotherapy, it is critical that the high dose region be shaped to fit the intracranial target volume in all dimensions. The contouring of the target region with the high dose region is known as conformation therapy [Bra82]. Various methods have been utilized in an attempt to conform the dose distribution to the shape of the target.

In conventional radiotherapy, combinations of weighted fields are used to help shape the isodose distribution. Wedged fields are sometimes used in conjunction with these weighted fields in order to produce dose gradients which help to further conform the distribution. Combination of different radiation qualities and modalities (photons and electrons) is a powerful tool often exploited in order to force dose deposition in a region of interest and maximize dose falloff outside of this region.

Field shaping devices are employed to contour these radiation beams to the shape of the targeted lesion. One common method of field shaping is the use of custom low melting alloy blocks for each treatment field. These blocks may be designed using either radiographic or computer generated Beam's Eye-View techniques (BEV). Radiographic techniques have historically been more common, since the physician need simply outline the shape of the block on radiographs taken through the target volume. CT scan data are often used to aid the radiotherapist in delineation of target and critical structures on the plane radiograph, but use of this data forces the physician to mentally integrate the two dimensional CT slices into a three dimensional image [She87].

The BEV technique more fully exploits the information obtained from CT scans by digitally reconstructing the data set in an arbitrary plane such that the observers eye may be hypothetically placed at the radiation source. By viewing the patient along the central axis of the radiation beam, the relative positions of anatomical structures may be easily determined and the target may be accurately delineated [Goi83].

Obviously, these custom blocks can only be used for static radiotherapy treatments which utilize a limited number of fields. Multileaf collimators may be utilized to increase the number of static fields since the projections of the leaves into the field approximate the smooth contour of custom shielding blocks. Dynamic multileaf collimation has been proposed in order to combine the benefits of arc therapy with BEV conformal techniques [Mos92]. Using the BEV, the leaves of these collimators may be adjusted to conform to the projected area of the target as the gantry and/or treatment couch are moving.

Similar conformation methods are employed in stereotactic radiosurgery. Various sizes of circular collimators are available which adequately conform the radiation beam to the shape of spherical lesions. Beam weighting and arc manipulations allow the spherical distribution to be elongated and rotated to better conform the high dose region to oblong target shapes. For highly irregularly shaped targets, more complicated techniques such as the use of multiple isocenters may be required. The use of multiple isocenters does often yield a conformal plan, but also leads to a large dose inhomogeneity (e.g., hot spots where the spherical distributions overlap) within the target volume. This appears to be undesirable since a retrospective study performed by Nedzi et al. indicates that dose inhomogeneity is associated with an increased risk of complications for the radiosurgery patient [Ned91]. McGinley et al. have designed an adjustable collimator to tailor the shape of the high dose region to the shape of irregular target volumes. This device consists of a circular collimator which was modified to allow the manual insertion of lead blocks in order to alter the beam shape and cause an elongation of the dose distributions [McG92]. The dose distribution can be elongated along the rotation axis or perpendicular to this axis. Elongation along other axes is not possible, which limits the clinical usefulness of this collimating device.

Dynamic field shaping is also under investigation for use in conformal radiosurgery. A retrospective study by Bova and Leavitt of over forty patients treated with radiosurgical techniques concluded that "over 2/3 of the patients would have received a reduced radiation dose to the normal brain through use of conformational field shaping techniques, had these capabilities been available" [Lea91,pg.1249]. Conceptual studies have been performed by Moss [Mos92] and Nedzi et al. [Ned92]. Moss investigated the viability of dynamic multileaf collimation. Using computer simulations, he compared the dose distributions that would result from the use of two and four jaw multileaf collimating systems to shape the fields for treatment of a variety of target shapes. He determined that either one of these systems would provide better conformal therapy than a rotating collimation system [Lea91] or the circular collimating system currently employed.

Nedzi et al. performed a computer modeling study which compared the use of five different field shaping devices. They determined the dose distributions that would result from utilizing these devices for the treatment of 43 tumors that had been previously treated at the Joint Center for Radiation Therapy of Harvard Medical School. They concluded that although an ideal multileaf collimator yields the best conformal plan, even simple field shaping devices offer an advantage over the circular collimating devices that are currently used. This improvement was most noticeable with irregularly shaped targets that previously required multiple isocenters, where simple field shaping devices can provide homogeneous dose distributions and adequate field shaping [Ned92].

One of these simple collimating devices is a rotating jaw collimator. A prototype rotating jaw collimator has been designed and constructed by Leavitt et al. [Lea91]. This device has two sets of rectangular collimators upstream from the existing circular collimator. The rectangular collimators are mounted on rotating tables such that both rotation and translation of the jaws are possible. Thus, this collimating system may define a polygonal field shape having up to four straight and four curved edges. Obviously, this device can not be used to effectively treat concave field shapes of lesions that are extremely irregular. It is very simple mechanically, however, and has been shown by Moss, Nedzi and Leavitt to be useful for many situations.

Although these techniques provide an attempt at conformal therapy, it is impossible to design a collimation system which can exactly tailor the shape of the dose distribution to the projected area of the target at every point on the target. These collimation schemes also fail to conform to the shape of treatment volumes that contain concave regions [Bor90]. A new conformation technique known as inverse radiotherapy planning has been proposed which theoretically alleviates some of the problems associated with current conventional techniques. Standard techniques in conformal therapy set up the beams desired for treatment and then compute a dose distribution based on these beams. If the distribution is not satisfactory, the beam set up is altered in an iterative fashion until the distribution is satisfactory. In contrast, inverse radiotherapy techniques begin with the desired dose distribution and calculate the fluences necessary to produce this distribution [Bor90]. This treatment technique is analogous to the filtered backprojection technique used for reconstruction of images in computed tomography (CT).

In CT, the two-dimensional density distribution of tissue within the patient is projected onto one-dimensional lines. These projections may be filtered and then backprojected resulting in a set of two-dimensional slice images. Analogously, inverse radiotherapy planning starts with a set of prescribed two-dimensional dose distributions which are projected onto lines. These projections may be mathematically filtered to obtain an intensity modulation function (IMF), and irradiation of the patient ("backprojection" of the IMF) results in the desired dose distribution. As with CT imaging, other methods have been attempted to solve this problem, and results of these research efforts will be discussed further.

In radiotherapy and radiosurgery, once the high dose region has been defined by the physician's outline of the target volume, the application of inverse planning has two primary components: 1) determine the beam fluences necessary to produce the desired dose distribution and 2) design a method of physically modulating the intensity of the radiation beam in order to produce these intensities. Once adequate solutions are obtained for these two components, inverse radiotherapy can theoretically produce a dose distribution which is not only BEV conformal, but conformal to the target shape in all dimensions. This research will investigate the efficacy of this conformal planning technique for achieving the aforementioned goal of radiation therapy.

CHAPTER 2
REVIEW OF THE LITERATURE

Inverse Radiotherapy Planning Algorithms

As mentioned previously, inverse radiotherapy planning offers a unique approach to conformal therapy in which the beam fluences necessary to create the desired dose distribution within a patient can be calculated from this very dose distribution. This technique was first examined by Brahme et al. in 1982 [Bra82]. The aim of this investigation was to determine the one-dimensional lateral dose profile required for an incident beam to produce a desired radial dose distribution after one complete rotation about the axis of symmetry of a cylindrical phantom. To further simplify the problem, a plane parallel beam was assumed and depth dose was approximated by a simple exponential characterized by a practical attenuation coefficient, μ. Buildup near the surface of the phantom was also disregarded. These simplifying assumptions allow the desired dose distribution following one complete rotation to be computed as

$$D(r) = \oint d(x) \exp(-\mu z) \frac{d\varphi}{\pi}$$

where d(x) describes the lateral dose distribution (dose variation along the x-axis), z is the distance from the center of the cylinder along the beam axis (perpendicular to the x-axis) and r is the radial distance from the center of the cylinder to any point within the cylinder. Through use of a transformation to polar coordinates, this integral may be rewritten as

$$D(r)=\frac{2}{\pi}\int_{0}^{r}\frac{d(x)\cosh[\mu(r^2-x^2)^{\frac{1}{2}}]}{(r^2-x^2)^{\frac{1}{2}}}dx.$$

which is the well known Abel integral equation. In order to obtain a solution for the lateral dose distribution, d(x), of the incident beam the Abel equation can be transformed into a convolution equation through another change of variables. The Laplace transform was applied to this convolution equation, and after a return to the original variables the explicit solution to the equation is

$$d(x)=\frac{d}{dx}\int_{r_0}^{x}\frac{\cos[\mu(x^2-r^2)^{\frac{1}{2}}}{(x^2-r^2)^{\frac{1}{2}}}D(r)rdr.$$

Thus, if the dose distribution, D(r) is known to be a continuously differentiable function, the lateral dose distribution of the incident beam may be calculated.

This simplified statement of the inverse problem allowed Brahme et al. to draw several important conclusions. First, they realized that the solution to this problem is nearly identical to the problem of filtered backprojection in CT scanning. Thus, algorithms already in use may be adapted to fit the inverse problem. The use of these algorithms can present problems, however, since they can lead to the need for physically unrealistic negative fluences when used for the inverse problem. Negative beam fluences are a recurring obstacle when one attempts to determine the beam fluences required to produce an ideal dose distribution (eg., a high dose region surrounded by a zero dose region). Obviously, it is physically impossible to have a high dose region surrounded by a zero dose region because the radiation beam deposits some finite dose as it traverses the region surrounding the target. Purely mathematical solutions to the inverse problem thus yield negative beam fluences which essentially subtract dose from the regions surrounding the target in order to produce the ideal dose distribution. Brahme et al. suggest that this problem can be avoided in practice with the use of higher energy beams. The lower attenuation coefficients associated with such beams lessens the need for negative beam fluences.

Cormack [Cor87a] attempted to extend the work of Brahme for use with dose distributions which are not circularly symmetric. Cormack utilized virtually the same simplifying assumptions as were used in the previous work. Buildup near the surface was ignored, as was scattering. These assumptions allow the dose to be directly proportional to the beam intensity. Beam divergence was also ignored, which is a reasonable approximation if the source is a large distance from the surface. This work further simplified the problem into what was termed the zeroth approximation. This approximation assumed that $\cosh(\mu x)=1$, where μ is the attenuation coefficient and x is the distance from the lesion to the surface. This assumption leads to a small error when used with higher energy beams ($\geq$ 10 MeV), but can cause a rather large error with lower energies. Mathematically, the zeroth order attempt was formulated as follows. The dose, D, delivered during a complete rotation at a point, P, with polar coordinates (p,φ) is

$$D(p,\varphi)=\frac{1}{\pi}\int_{\varphi-\pi/2}^{\varphi+\pi/2} f[p\cos(\theta-\varphi),\theta]d\theta,$$

where f denotes the fluence delivered along a single line during the rotation, as depicted in Figure 2-1.

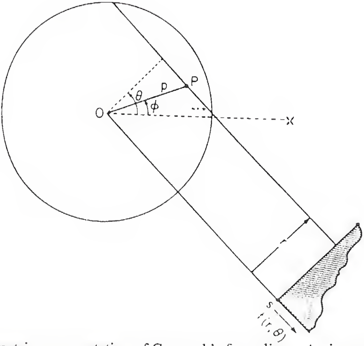

Figure 2-1: Geometric representation of Cormack's formalism. An intensity distribution f produces a constant dose along the line through P. The line OS makes an angle $\pi/2$ - θ with the x-axis. Reproduced with permission from Elsevier Science Ltd., UK [Cor87a, pg. 625, Figure 2].

Thus, this problem takes the form of a Radon transform, which is simply the problem of determining a function from its integrals along straight lines. Radon transforms have a well established mathematical form which can be extended for use with the inverse problem. The desired result can be obtained by expanding D in orthogonal functions, and directly deriving the expansions of f_l. The resulting equation is

$$f_l=\sqrt{\pi}\frac{(l+n)!\Gamma(l+n+2m+2)}{(l+n+r)!\Gamma(l+n+m+3/2)}sG_{l+n+m}(\lambda,\frac{3}{2},s^2)$$

where s is the distance from the center of the patient to the intensity distribution, r is the distance from the intensity distribution to the x-axis, G is a shifted Jacobi polynomial, and l, m, n, and λ are integers.

Cormack also noted the requirement for negative beam intensities which is imposed by the mathematical formalism. To deal with this problem, the beam intensity was set equal to zero where negative intensity was required by the theory. Although this approach fails to yield the ideal dose distribution, it is "perhaps no worse than the trial and error method presently used in treatment planning" [Cor87a, pg. 630].

Cormack and Cormack [Cor87b] proceeded to a solution for what was termed the first-order approximation. The first order approximation used the same formalism and utilized many of the same assumptions (e.g., ignored scatter, buildup, and divergence) as were used in the zeroth approximation. The first order approximation was extended to include use with larger attenuation coefficients, and thus be useful with lower energy beams. Thus the form of the equation required to solve for the integral dose after one complete rotation is very similar to the one previously seen:

$$D(p,\varphi)=\frac{1}{\pi}\int_{\varphi-\frac{\pi}{2}}^{\varphi+\frac{\pi}{2}} f[p\cos(\theta-\varphi),\theta]\exp[-\mu(R^2-r^2)^{\frac{1}{2}}]\cosh[\mu p\sin(\theta-\varphi)]d\theta.$$

It was determined that the first order approximation was in the form of an attenuated circular Radon transform. The problem was then solved for several specific dose distributions with an axis of symmetry, but a general solution was not obtained due to the mathematical difficulty encountered in solving this problem.

In 1988, Brahme attempted to apply the inverse approach in order to obtain optimal dose distributions for dynamic therapy. The desired dose distribution was modeled as a density of point irradiations, and the fluences required by at each gantry position were obtained by backprojection of these densities on the position of the radiation source. The optimal dose distribution was subdivided into basic optimal distribution densities for point targets. The desired dose distribution could then be computed as the convolution of these point dose densities with the point irradiation intensities,

$$D(\vec{r})=\iiint_{V}\varphi(\vec{r}_c)d(|\vec{r}-\vec{r}_c|)d^3r_c$$

where d is the point dose density, phi is the point irradiation intensity, r is the distance from the center of the phantom to the point of dose calculation, and r_c is the center coordinate for each point irradiation. This convolution was performed in Fourier space, which eased the inversion of the equation since we now have a simple product of two Fourier transforms

$$F\{D(\vec{r})\}=F\{\varphi(\vec{r}_c)\}\cdot F\{d(|\vec{r}-\vec{r}_c|)\}.$$

Inversion of this equation yields the irradiation intensities in Fourier space. Taking the inverse Fourier transform yields the point intensities, but also results in zeros which cause large oscillations in the intensity function. Analogous to CT filtered backprojection, introduction of a low pass filter, Z(s,λ) in Fourier space smooths the intensity function resulting in the following form for solution of the point irradiation intensities:

$$\varphi_\lambda(\vec{r})=F^{-1}\{Z(\vec{s},\lambda)\frac{\tilde{D}(\vec{s})}{\tilde{d}(\vec{s})}\}$$

These point irradiation densities may then be decomposed into thin pencil beams and convolved back with the point dose distributions taking into account the true patient geometry. This allowed the production of isodose lines, which were simply the reverse of the procedure just completed multiplied by a correction for beam absorption during backprojection. A comparison of the results from use of this technique with conventional radiotherapy techniques can be seen in Figure 2-2. As seen in the figure, only complex conventional treatments can provide adequate conformation in cases involving concave targets. If the dose rate is varied along with the field size, however, Brahme theorized that even simple treatments such as two or three field techniques are sufficient.

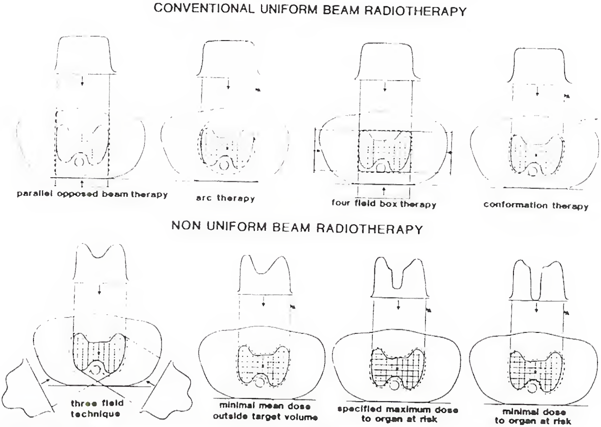
CONVENTIONAL UNIFORM BEAM RADIOTHERAPY
parallel opposed beam therapy
arc therapy
four field box therapy
conformation therapy
NON UNIFORM BEAM RADIOTHERAPY
three field technique
minimal mean dose outside target volume
specified maximum dose to organ at risk
minimal dose to organ at risk

Figure 2-2: Schematic comparison of inverse radiotherapy planning with conventional radiotherapy techniques. Modulation of beam fluence allows dose conformation (---) to targets (shaded) as well as minimization of dose to critical organs. Reproduced with permission from Elsevier Science Ltd., UK [Bra88, pg. 138, Figure 7].

Barth [Bar90] extended this work to the case of ideal dose distributions for convex phantoms of arbitrary shape. The general approach was to represent arbitrary dose distributions as numerous small radially symmetric dose distributions (see Figure 2-3). The problem was then broken down into a summation of attenuated Radon transforms, so the mathematical formalism was very similar to that used by Cormack and Cormack [Cor87]. The inversion of these transforms lead to the required beam fluences. Scatter, buildup and divergence were again ignored in order to simplify the problem. The difficulty of negative beam fluences was again encountered, and these were simply set to zero as usual.

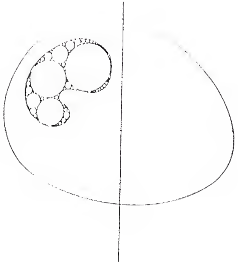

Figure 2-3: A convex phantom of arbitrary shape with an arbitrarily shaped dose distribution comprised of N small radially symmetric dose distributions. Reprinted with permission from Elsevier Science Ltd., UK [Bar90, pg. 429, Figure 4].

Barth felt that these explicit methods of fluence calculation can not be used to determine the final treatment plan due to the numerous simplifying assumptions which must be employed in order to perform the calculations. Instead, he felt that this technique would be useful as a starting point for traditional forward iterative methods of plan optimization. Consequently, several methods have developed which exploit the use of both analytical and iterative techniques. For example, Bortfeld et al. [Bor90] applied image reconstruction techniques to the inverse problem. The required beam fluences, or intensity modulation functions (IMF), were calculated utilizing two well established CT algorithms: filtered backprojection and the iterative reconstruction technique (IRT). Scattering, buildup, divergence and inhomogeneities were ignored. To perform backprojection, the prescribed dose distributions were first projected onto lines, which is basically a simple summation of dose densities along ray lines. A two-dimensional Fourier transform of these lines was performed, and a high pass filter was applied. Backprojection was then performed to obtain the IMF, and negative values of the IMF were set to zero. It was determined that this procedure did not significantly effect the isodose lines.

This explicit approach does not force the isodose lines to exactly fit the target. To further optimize the dose distribution, IRT was applied using the filtered backprojection solution as its initial guess. The following criteria were deemed important for the optimization process.

1) Target dose should be close to prescribed dose.

2) Target dose should be homogeneous.

3) Dose to sensitive organs should be below their tolerance level.

4) Dose to normal tissues surrounding the target should be low.

An objective function was formulated to mathematically incorporate the first two criteria. The third requirement was stated as a constraint and the fourth is already required by the conformal technique. The mathematical formulation of the objective function was as follows:

$$F_1 = \sum_{i \in T} (d_i - p)^2 = minimum$$

where d_i is the calculated dose and p is the prescribed dose. The summation was taken over all target points, and the function was minimized to obtain the best dose conformation. Seven iterative steps with the objective function lead to adequate conformation for complex targets, including convex shapes such as a horseshoe targets. The authors felt that extremely complex targets, however, might require additional iterative steps.

Holmes et al. have devised an iterative filtered backprojection algorithm based on the analogy between SPECT image reconstruction and rotational radiotherapy [Hol94]. The initial beam profile is obtained through inversion of the ideal dose distribution. This inversion is essentially a filtered fourier deconvolution of the dose distribution and a monte carlo generated energy deposition kernel, which results in the incident energy fluence. All negative fluence values are initialized to zero, and the forward dose is calculated using a filtered Fourier convolution of this inversely obtained incident energy fluence with the energy deposition kernel. The dose distribution thus obtained is then compared against dose constraints for regions of interest, and if all points in the distribution are within the constraints, the calculation is accepted. If the calculation is deemed unacceptable, the residual dose in the regions of interest is utilized to determine a new fluence profile. Dose is recalculated using this new energy fluence, and this process continues iteratively until an acceptable solution is obtained.

Harmon also explored a compromise between analytic and iterative techniques by combining deconvolution and optimization [Har94]. This approach offers more flexibility than some others since it can calculate beam fluences for either rotational therapy or multiple static beams. In order to determine a two-dimensional fluence profile for each beam portal chosen by the user, deconvolution of a monte carlo generated single voxel energy deposition kernel from the desired dose distribution is performed. This results in a TERMA (total energy released to matter) profile for each beam, which can be used to calculate the physical characteristics of the intensity modulator by ray tracing back toward the radiation source. This ray trace includes inverse square, attenuation in phantom and an effective attenuation through the modulation device. With this TERMA profile in hand, forward dose calculation proceeds via convolution of the TERMA with the aforementioned kernel. If multiple beam portals are designated, relative beam weighting for each portal is determined by an optimization routine which varies all weightings until the best fit to the desired dose distribution is obtained.

Purely iterative techniques have also been explored for solution of the inverse radiotherapy planning problem, as exemplified by Webb's use of simulated annealing to optimize the required beam configurations [Web89, Web91a, Web91b, Web92]. This method "mimics the way a thermalized system . . . achieves its ground state as the temperature slowly decreases" [Web89, pg. 1352]. Webb's initial approach begins with a two-dimensional dose prescription and assuming that the treatment volume is axially uniform, the dose in each small elemental beam is projected along one dimensional lines. Scatter and buildup are ignored, and the dose is then calculated as the product of beam weighting and exponential attenuation. The beam weighting is allowed to start at zero, and weighting is slowly added iteratively until the desired weighting for each elemental beam is determined. Later papers in the series extended Webb's initial work by including scatter in the two-dimensional technique [Web91a] and determining optimal elemental beam weightings for three-dimensional conformal treatment planning [Web91b, Web92]. Scatter is never included in Webb's three-dimensional technique. Interestingly, this iterative technique represents a purely forward approach to solution of an inverse radiation transport problem.

Inverse radiotherapy planning based on this technique has been commercialized by the Nomos Corporation [Nom94]. Nomos models the elemental beams as 1x1 cm^2 measured finite size pencil beams and calculates dose for each of these pencil beams using a simple model based on tissue-maximum ratios and off-axis ratios. Optimal beam weightings for these pencil beams are determined using a two-dimensional simulated annealing algorithm. These two-dimensional optimized slices are then summed in order to determine a three-dimensional dose calculation. Although two-dimensional optimization does not guarantee an optimal three-dimensional treatment plan, time required for execution of the three-dimensional optimization using computer hardware currently available renders it impractical for this approach.

Clinical Treatment Planning Studies

Historically, treatment plans were designed utilizing a relatively limited number of radiation field arrangements and the dose delivered from these fields was then superimposed on only one or at most a select few transaxial images of the patient. Comparison of rival treatment plans was thus relatively straightforward and based primarily on the physician's experience and basic dosimetric endpoints such as target dose uniformity and maximum critical organ dose as represented on this limited number of axial slices [Kut92]. The advent of three dimensional and conformal treatment planning systems and the complexity inherent in plans generated using such systems has sparked interest in more sophisticated methods of plan evaluation. The principal complicating factor in evaluation of such treatment plans rests in the large volume of data generated by such systems. As opposed to the single slice evaluation required for conventional treatment plans, three dimensional treatment planning systems often superimpose the dose distribution on fifty or more contiguous axial CT slices. Although displays are developing with tools which aid in the graphical comparison of rival treatment plans, it remains extremely tedious and time consuming to correlate and analyze the dose distributions on multiple axial slices of the patient [Mun91]. Conformal treatment planning systems have further complicated plan evaluation by presenting the clinician with dose distributions which deviate substantially from those typically utilized for patient treatment.

Various numerical evaluation techniques have developed, but have historically been associated primarily with computerized optimization routines [Nie93, Kal92, Moh92, Web92]. These algorithms, some of which were discussed in the preceding section, attempt to quantify the relative merit of plans through the use of dosimetric and or biological parameters which are formulated into objective functions. The various computerized algorithms then attempt to minimize or maximize the objective function, which should result in the ideal plan. Niemierko et al., for example, optimized the beam weightings for portals chosen by the user utilizing objective function based on normal tissue complication probability (NTCP) and tumor control probability (TCP) [Nie93]. Reportedly, these researchers have studied over forty clinical treatment plans and found that on average their optimization routine could quickly determine a better plan than one constructed by an experienced treatment planner. Similarly, Mohan et al. designed an algorithm based on simulated annealing that varies beam weightings in order optimize an objective function based on NTCP and TCP [Moh92]. Demonstrating their algorithm using a case of prostate cancer, the researchers found that their algorithm could design a plan with higher TCP and lower NTCP than the plan used to treat the patient. Webb [Web92] and Kallman [Kal92] both experimented with the use of dose response functions in their respective optimizations and both presented clinical examples. Neither compared these results to treatment plans designed by an experienced treatment planner and were used simply to demonstrate the use of their respective algorithms.

The first wide-scale attempt at quantitative evaluation of clinical treatment plans was undertaken by the Collaborative Working Group on the Evaluation of Treatment Planning for External Beam Radiotherapy (CWG) and reported on in the International Journal of Radiation Oncology Biology Physics. In their study of three dimensional treatment planning systems, the CWG developed and or improved treatment plan evaluation tools such as dose volume histograms (DVH) [Drz91], NTCP [Kut91a], TCP and a subjective numerical scoring system [Mun91a]. In addition, the CWG reviewed two-dimensional dose distributions superimposed on reconstructed axial, sagittal and coronal planes within the patient. These tools were then used for the evaluation of three-dimensional treatment plans generated for eight separate treatment sites: nasopharynx [Kut91b], larynx [Coi91], intact breast [Sol91], Hodgkin's disease [Bro91], lung [Ema91b], para-aortic node [Mun91b], prostate [Sim91] and postoperative rectum [Sha91b]. Comparison of the three-dimensional plans with conventional plans used for treatment of these lesions proved 3-D planning a useful tool which ensured proper delineation of the target in all dimensions as opposed to one axial plane, and also allowed clinicians to better avoid critical organs near the treatment volume.

Conformal radiotherapy planning has not enjoyed the benefit of thorough investigation by a collaborative working group, although several researchers have studied the efficacy of this approach. Due to the high incidence of acute and chronic toxicities associated with conventional radiotherapy of the prostate, many researchers have studied this disease site for conformal radiotherapy. In these studies, conformal is defined as treatment in which fields are designed using a beam's eye view display (BEV). Several use only a standard four field box technique with blocks designed using the BEV utility [Vij93, Sha91a, Sof92], while others add oblique fields to this standard technique in order to attain better distributions [San91]. These studies showed that dose to nearby critical structures such as the bladder and rectum could be reduced by up to 31% and

25%, respectively, when compared to clinical controls [Sof92]. In addition, clinical trials have proven that incidence of acute toxicity is reduced using BEV conformal techniques for radiotherapy of prostate carcinoma. Based on these results, several researches are initiating dose escalation studies in hopes of increasing local tumor control without increasing normal tissue toxicity above acceptable levels.

Similarly, a group at Memorial Sloan Kettering Cancer Center has investigated the use of three-dimensional conformal radiotherapy for prostate, nasopharynx and lung lesions [Lei91, Arm93]. These studies also defined conformal therapy as treatment using field shaping blocks designed with aid of the BEV utility. Rather than a clinical trial, however, the investigators used the quantitative evaluation tools developed by the CWG in order to compare their conformal and conventional therapy results. Similar to the prostate clinical trials, these analyses suggest that three-dimensional conformal radiotherapy may provide a clinical advantage over conventional techniques. For example, a study of nine lung patients showed both an increase in the minimum target dose and a significant decrease in the calculated NTCPs when conformal treatment planning was used [Arm93].

Conformal stereotactic radiosurgery techniques have also been studied to determine their efficacy for clinical treatments. Moss studied the use of multileaf collimators, both real and hypothetical, for small intracranial lesions [Mos92]. Using dose distributions, DVHs and the integrated logistic function, which is a dose-effect model based on NTCP theory, he concluded that clinically useful conformal therapy for small targets could only be achieved through the construction of multileaf collimators with 5 mm wide leaves (size projected to isocenter) as opposed to the 1 cm wide leaves currently manufactured. Nedzi et al. used forty-three patient data sets to study treatment plans designed using five dynamic field shaping devices for stereotactic radiosurgery: fixed circular collimators, two independent jaw collimator, four independent jaw collimator, four independent rotatable jaw collimator and an ideal multileaf collimator [Ned92]. Comparison of rival plans was accomplished via DVHs and a construct they termed the treatment volume ratio, TVR. The TVR is defined as the target volume divided by the volume receiving at least the minimum target dose. As expected, the ideal multileaf collimator provides the best field shaping, but even simple BEV field shaping devices provide a clinical advantage over fixed circular collimators.

Clearly, the literature indicates that the initial step towards acceptance of novel treatment methods is to establish that they are clinically superior to the status quo. Interestingly, however, this has not yet occurred with inverse radiotherapy planning. Physicists have repeatedly demonstrated the utility of inverse radiotherapy planning for fitting arbitrary desired dose distributions. Various conic sections [Woo93, Har94] and concave targets [Hol94, Har94] are the most often matched by inverse planning investigators. A few investigators have attempted clinical examples, but have not compared these examples to conventional treatment plans [Har94]. The following investigation will attempt to bridge the gap left between laboratory novelty and clinical viability.

In so doing, it is also hoped that this work will contribute to the growing body of knowledge that has been made possible by the advent of three-dimensional treatment planning systems which adequately model dose deposition. Since accurate dose volume data is only available through the use of such systems, radiotherapy treatment planning has historically been based primarily on the training and experience of the physician. Through this and other similar studies, more detailed dose-volume data can be obtained for both the current state of the art in radiotherapy, and for potential future improvements on the state of the art. Armed with these facts rather than dogma, hopefully the art of radiotherapy treatment planning can some day be transformed into a true science.

CHAPTER 3
UNIVERSITY OF FLORIDA RADIOTHERAPY TREATMENT PLANNING

Traditionally, the term radiotherapy treatment planning has been used to describe computation of the dose distribution for one or a few transaxial sections within the patient. Recent advances have improved the way in which treatments are planned, however. Improved imaging modalities such as computed tomography (CT) and magnetic resonance imaging (MRI) coupled with improved computer assisted planning techniques permit three-dimensional treatment planning based upon realistic representation of the patient's anatomy [Goi88]. Recognizing the effect of these advances on treatment planning, the term now generally includes target localization and delineation in addition to field design and dose calculation. This chapter will briefly discuss treatment planning for the three primary teletherapy planning methods used at the University of Florida's Shands Cancer Center: conventional planning, three-dimensional beam's eye view planning (virtual simulation) and radiosurgery treatment planning.

Conventional Treatment Planning

Numerous imaging modalities, most notably CT and MRI, are utilized to determine the extent of disease and its position relative to normal structures. Definitive treatment field design is accomplished, however, via use of a treatment simulator, which incorporates a diagnostic x-ray tube into an apparatus that duplicates the geometrical and mechanical properties of the treatment unit. Although information obtained from CT and

MRI studies can be used as an aid for target delineation, conventional treatment planning cannot fully exploit this three-dimensional data base due mainly to the fact that the geometrical relationship between the patient's anatomy and the radiation beam cannot be duplicated using a standard diagnostic x-ray unit [Kha84]. The simulator has fluoroscopic capabilities which allow dynamic visualization of the patient's anatomy and ensure proper positioning of the treatment fields. After the fields have been positioned, plane radiographs are taken and the irregular fields which encompass the target are designed on these films and digitized into the treatment planning computer system (Theraplan, Version 5, produced by Theratronics International Limited). Dose calculation requires not only information regarding the irregular field shapes, but also the patient's external contour. This information is obtained via placement of solder wire around the patient and passing through the central axes of the treatment fields. Since the wire is quite malleable it easily conforms to the contour of the patient. This contour information may then be digitized into the treatment planning computer to generate a central axis slice of the patient (generally transaxial).

After input of these treatment data, Theraplan calculates dose from photon fields using a two-dimensional semiempirical model which separates dose deposition into its primary and scattered components. The primary dose may simply be modeled as [The90]

$$D_{pri} = f(d,x,y) \cdot D_A(d) \cdot TAR(d,0)$$

where f(d,x,y) = a function which describes the beam intensity profile in air at depth d,
D_A = the dose in free space at depth d and
TAR(d,0) = the zero area tissue air ratio, which describes attenuation of the primary beam by a thickness, d, of tissue.

The scatter dose contribution, which is deposited by photons which undergo at least one interaction before depositing dose, is calculated using a Clarkson integration technique [Joh83]. Since this scatter component is dependent both on field size and shape, the field is divided into n equal sectors with an angle, θ, between each. The scatter components from all n sectors are then summed as follows

$$D_{sca} = \frac{\theta}{2\pi} \cdot \sum_{i}^{n} SAR_i(d,r)$$

where SAR(d,r)= scatter air ratio for circular field size r at depth d = TAR(d,r) - TAR(d,0). After performing these two calculations, the scatter and primary contributions are reassembled in order to determine the total dose calculation.

Electron dose calculation is performed in Theraplan by first dividing each electron beam into square pencil beams measuring 0.5 cm on each side. Using a modification of a semiempirical method derived from the age diffusion equation [Kaw75], the dose contribution, D, from each pencil at a point (x,y,z) is calculated as [The90]

$$D(x,y,z,\tau) = A \cdot \left[erf\left(\frac{X_0(z)-x}{2\sqrt{\kappa\tau}}\right) + erf\left(\frac{X_0(z)+x}{2\sqrt{\kappa\tau}}\right)\right] \cdot \left[erf\left(\frac{Y_0(z)-y}{2\sqrt{\kappa\tau}}\right) + erf\left(\frac{Y_0(z)+y}{2\sqrt{\kappa\tau}}\right)\right]$$
$$\cdot \cos\left(G_1 \cdot \frac{z^2}{R_p^2} + G_2 \cdot \frac{z}{R_p} + G_3\right) \cdot \exp\left(\frac{2\pi}{3R_p} \cdot \sqrt{\kappa\tau}\right)^2 \cdot \left(\frac{SSD}{SSD+z}\right)^2$$

where $X_0(z)$ = half the pencil width at depth z
$Y_0(z)$ = half the pencil length at depth z
x = distance from pencil center to calculation point in direction of field width
y = distance from pencil center to calculation point in direction of field length
z = depth in tissue
R_p = practical range for electrons = intersection of depth dose curve with bremsstrahlung background
$\kappa\tau = (C/R_p + 0.05^{1/N})^{2N}$
SSD = distance form source to surface of patient

G_1, G_2, G_3, C, N, and A = parameters which Theraplan varies in order to obtain the best fit to measured data. After calculation of the dose contribution from each pencil beam, each pencil is weighted depending on its position relative to the field edge. The weighted doses from all the pencil beams are then summed to determine the total dose given to the point (x,y,z).

Three-dimensional Treatment Planning (Virtual Simulation)

Although CT scanners provide detailed information about the anatomy of a patient, it is not in a practical form for radiotherapy treatment planning. When utilizing these scans as an aid to treatment planning, the radiotherapist must "mentally integrate a set of 2D shapes into a 3D structure, visualize the intersection of his prescribed treatment beams with that structure, visualize the resulting film, correlate that imagined film with the actual simulation film, and determine what if any adjustments need to be made." [She87, pg 433]. Virtual simulation more adequately integrates the CT scanner into the treatment planning process and thus allows the radiation oncologist to better exploit the 3D data set by reconstructing a virtual patient from the CT data transferred to Theraplan.

In order to ensure accurate coordinate transfer between the CT scanner, treatment planning computer and treatment machine, CT scans must be performed with the patient immobilized in the treatment position. Position information is registered in an images_info file that is stored along with the image data. These CT simulation scans are transferred to the treatment planning computer, where delineation of target and critical structures can be performed. Although Theraplan allows the user to now digitize the fields into the system from simulation films, the strength of virtual simulation is that it allows the user to design radiation portals utilizing a beam's eye view display.

Theraplan's BEV utility places the user's eye at the radiation source, and permits interactive portal design while the user looks along the central axis of the beam. From this vantage point, the radiotherapist can view the full 3D anatomy at once and examine the relative positions of anatomical structures as seen by the primary beam [Goi88]. This option provides a superior display from which to vary field size and also to design field shaping blocks to match the patient's anatomy. Unfortunately, the time investment required for collaboration of physician and dosimetrist to perform virtual simulation prohibits its use except for cases in which portal design is especially difficult.

Dose calculation in Theraplan is performed the same for virtual simulations as it is for conventional treatment planning situations. Although the system performs all calculations in 2D, it can perform a pseudo 3D calculation. This option calculates the 2D dose distribution on all of the transaxial slices within the data set and presents a 3D dose distribution. Using this tool, the radiotherapist may calculate the 3D dose distribution from portals he has designed, and then interactively alter these portals if this distribution is deemed unacceptable.

Stereotactic Radiosurgery Treatment Planning

Stereotactic radiosurgery was the first clinical application of virtual simulation since treatment plans are designed exclusively using a virtual patient recreated from imaging studies of the actual patient. In order to accurately localize the lesion, a frame of reference known as the Brown-Roberts-Wells^{TM} (BRW) ring must be attached to the patient's head. This device is a metal ring which attaches to the patient's head via four aluminum pins [Fri89]. Once this frame is attached, it becomes the reference point for all localization and enables accurate coordinate transfer between imaging devices, treatment planning system and linear accelerator.

To obtain CT images, the BRW ring is affixed to the CT couch and a localizer is then attached to the BRW ring via three tooling balls. The CT localizer consists of nine rods; three pairs which are aligned with the patient and angled rods between each pair [Saw87]. After a scout image has been obtained, transverse slices are obtained in the region of the lesion. The localizer rods also appear in each image slice. Since the spacing of the rods is known, the position of any object within the CT localizer can be determined [Saw87].

Certain types of lesions require other diagnostic localization techniques. For example, arteriovenous malformations often require the use of contrast angiography in addition to CT. A special angiographic localizer cage is required for radiographic localization. This localizer has four lucite plates which each contain fiducial marks. These fiducial marks act as the reference points for localization [Sid87]. After the BRW ring is attached to an immobilization mount and the localizer, a standard angiogram is performed. After numerous biplane images are obtained, the anteroposterior (AP) and lateral images where the nidus is best defined are selected.

Another special localization technique is the use of magnetic resonance imaging (MRI). This technique is most often utilized for the localization of acoustic neuromas or tumors which are near a bone that could cause an artifact in CT localization. Since high magnetic fields are used in MRI, a special BRW head ring made of aluminum is attached to the patient's head with nonmagnetic pins. Once again, a special localizer cage is required. Geometrically, this cage is exactly the same as the CT localizer cage. Due to the magnetic fields, however, the cage is composed of plastic. The localizer rods on the MRI localizer are filled with a contrast material, propandiol, so that they may be seen on the scan. To improve the signal-to-noise ratio of the scan, a special head coil was designed for use in stereotactic localization. Once the BRW ring is attached to the localizer cage and a special bracket on the head coil, the MRI scan proceeds as a normal head scan.

A three-dimensional treatment planning system is utilized which runs on a SUN SPARCstation. CT images are transferred to the SUN system via a network connection. The nine localization rods must be identified in the first slice, and each pixel is mapped into stereotactic space. The computer program automatically locates the position of the rods in subsequent slices. The neurosurgeon then uses a mouse to outline the target in the axial, coronal and sagittal planes. A treatment plan is designed which will focus noncoplanar arcs of radiation such that they intersect at the center of the target, which is known as the treatment isocenter. Figure 3-1 illustrates the location of arcs relative to the patient's external contour. The intersection of these arcs at the isocenter concentrates the dose in the targeted region while spreading low dose throughout the normal tissue, thus creating a very steep dose gradient outside of the target.

Typically the first step in treatment design is selection of a standard treatment plan which contains default values for the number of arcs, table angle, gantry start and stop angles and weighting for each arc. These treatment variables are then altered such that the dose distribution best conforms to the projected area of the target in three dimensions. For example, the collimator size is chosen such that it will produce a circular beam which best fits the size of the target. Arcs and/or table angles may be altered or deleted which changes the shape of the distribution. For nonspherical lesions multiple isocenters are sometimes employed, although as stated earlier, the dose inhomogeneity introduced by this technique may be undesirable. This iterative technique is repeated until the dose distribution fits the shape of the lesion with minimal dose to normal tissues. The 80% isodose line is generally chosen as the portion of the dose distribution which should best conform to the shape of the lesion. The fit may be examined by starting at the first CT slice and having the computer step through the subsequent slices in 1 mm increments. The system computes and displays the isodose lines for each slice as it steps through the images.

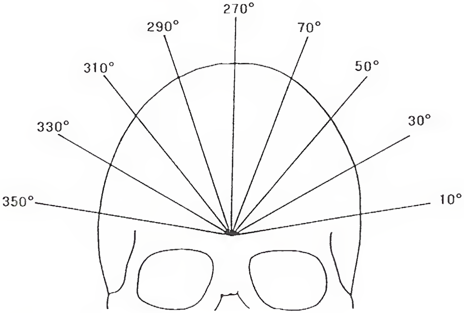

Figure 3-1: Location of nine standard table angles relative to patient's head. Typically, arcs are 100 degrees in length at each table angle. Figure redrawn from [Spi92].

The dose algorithm uses tissue-phantom ratios (TPR), off axis ratios (OAR), and the inverse square law to compute the dose anywhere along the beam [Bov90]. TPR gives the relationship of the dose along the central axis of the beam, OAR is used to determine the relative intensity along the cross section of the beam, and the inverse square law gives the variation of the intensity of the beam with distance from the source. Thus, the dose at any point, p, in a circular field may be computed from [Suh90]:

$$D_p(c,STD,d,r) = D_{ref} \cdot ROF(c) \cdot TMR(w,d) \cdot OAR(c,STD,d,w) \cdot \left(\frac{SAD}{STD}\right)^2$$

where c = field size at SAD
STD = source-to-target distance
d = depth of point p
r = off axis distance
w = field size at point p
D_{ref} = reference dose
and ROF = relative output factor.

Similar treatment planning techniques are employed with MRI and angiographic localization. MRI images are transferred via the network system and treatment planning proceeds as it does with the CT localization. Since the images obtained through use of MRI can have spatial inaccuracies, planning is also performed using the stereotactic CT images, and the end plans are correlated to ensure accuracy.

The procedure is slightly different when angiographic localization is used. Since the angiographic images are not stored digitally, the AP and lateral plane films chosen during localization are utilized for treatment planning. The films are placed on a digitizer and the positions of the fiducial marks are entered. The digitizer is then used to outline the nidus in both projections. Using this data, the computer can calculate the geometric center and the center of mass of the target. Angiography presents several problems that make it inadequate for localization by itself. These problems include errors in determining target size and shape [Bov91]. For example, there is a risk of underestimating the true maximum target diameter by as much as 41% [Bov91]. Thus, when angiographic localization is utilized, it must be used in conjunction with CT localization in order to avoid significant errors which can lead the unnecessary treatment of a large amount of normal tissue [Bov92].

Since the stereotactic CT scans are always utilized, the planning system allows the user to plan and evaluate the plan in three dimensions using interpolated reformatted CT scans. Through the use of this technique, the full set of anatomic data is available to the user. The system allows the user to contour lesions and anatomical structures, but these tools are not commonly utilized since they are very time consuming and unnecessary for evaluation of a given treatment plan. Without these contours, however, it is impossible to obtain dose volume histograms for the structures of interest. For purposes of comparison within this project, these data were obtained for several stereotactic radiosurgery patients.

CHAPTER 4
INVERSE RADIOTHERAPY TREATMENT PLANNING

Inverse radiotherapy treatment planning may be performed using the Peacock Plan™ system developed by the Nomos corporation. This treatment planning system is part of an integrated 3D conformal planning/multivane intensity modulating system. Treatment plans produced using Peacock Plan generate a set of beam weights which allow the multivane intensity modulating compensator (MIMIC) to deliver a conformal treatment [Nom93].

MIMIC

The operation of the treatment planning system is best understood if one first has some understanding of the device which is simulated by Peacock Plan. The MIMIC consists of twenty independent vanes which each project a 1x1 cm block at the machine isocenter. It attaches directly to a linear accelerator and modulates the intensity of a slit collimated radiation beam. Intensity modulated slit irradiation, in conjunction with the rotation of the gantry about the patient, allows for a slice of the patient to be treated with a radiation dose that conforms to the shape of the target volume within the slice. After this slice has been treated, the table is indexed and the next slice is treated. This procedure may then be repeated until all slices within the target volume have been treated. Obviously, this treatment modality is analogous to the method in which CT scanners image in a slice by slice fashion. In order to shorten the required treatment time, the MIMIC is capable of modulating two one centimeter thick slices per gantry rotation.

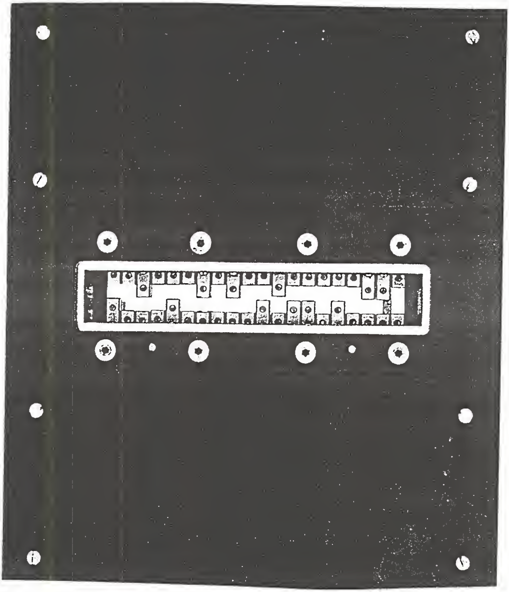

Figure 4-1: Beam's Eye View (BEV) of MIMIC, which contains two sets of twenty 1 cm wide independent tungsten vanes.

The MIMIC shapes the intensity of the beam through temporal modulation. Each of the singly focused vanes may be independently addressed and translated into the path of the radiation beam via use of pneumatic pistons. Since the eight cm tall tungsten vanes allow minimal transmission of the primary beam (approximately 2% for 10 MV x rays), the intensity of the beam underneath a vane will be proportional to the amount of time that the vane is open during irradiation. The Peacock Plan™ allows for eleven different dwell times, which leads to effective transmittance values ranging from 0 (actually 2) to 100 percent in ten percent increments. For computer simulation purposes this number of transmittances may be varied, and if found to significantly effect the treatment plans it could easily be modified for the MIMIC.

This all or nothing approach to dynamic beam compensation has two primary advantages. First, beam transmission is determined by the dwell time of full height tungsten vanes, so beam hardening effects need not be considered as they must be with conventional compensation techniques and collimators which spatially modulate the beam. Secondly, unlike spatial modulating collimators, accurate distance encoding is not necessary for the vanes since the vanes have only two positions (in or out) [Mac94].

As with any one-dimensional multivane dynamic modulator, the MIMIC has several limitations. These problems are due primarily to the inefficiency of dose delivery through these devices. Modulation of the beam intensity requires blockage of a majority of the beam for the patient treatment. Thus, to deliver the same dose, the beam on time is much more than with conventional treatments. Since there is a small transmission through the vanes, a small background dose will be present within the patient. Further, since the beam on time is lengthened, there will be an increase leakage dose from the linear accelerator which may necessitate increased shielding thickness of the secondary barriers in the treatment vault or increase in linac head shielding. These are engineering details which can be examined if intensity modulated treatments prove beneficial. In fact, with clever design, some of the current disadvantages of intensity modulation could possibly become advantages. For example, utilizing a two-dimensional modulator can potentially increase the efficiency of treatment under certain situations such as with stereotactically treated brain lesions which require multiple isocenters [Har94].

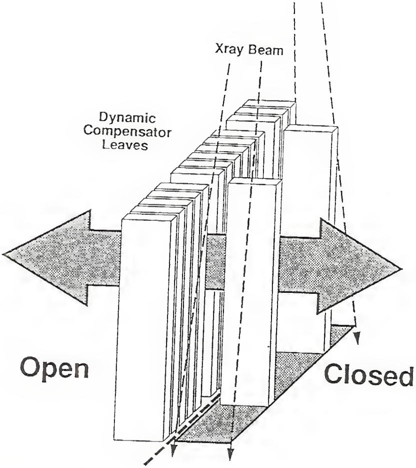

Figure 4-2: Illustration of MIMIC operation. Reproduced with author's permission [Mac94, pg. 1711, Figure 3].

Peacock Plan™

The general concept of inverse radiotherapy planning allows the user to specify the desired result, and then the treatment planning system automatically computes a plan that satisfactorily produces this distribution. In order to specify this desired result, Peacock Plan™ has various tools which allow the user to delineate the contour of the target tissue and any critical structures that appear on CT data which have been transferred to the system. It is imperative that this image overlay data contain all structures pertinent to the planning process, since the inverse planning process relies on information about the sensitivity of critical structures near the treatment volume and their importance (weighting) relative to the target. Peacock also requires input of dose prescribed to target (cGy), desired treatment complexity and safety margins which take into account setup inaccuracies and the possibility of microscopic disease surrounding the target.

Once these data are input, the planning process is performed automatically by the computer. The isocenter is determined as the geometric center of the defining rectangle of the target. Peacock Plan™ then simulates the MIMIC by subdividing each beam portal into 20 one by one centimeter pencil beams. An initial guess for the weight of each of these pencil beams is obtained through a backprojection technique

$$Beam\ Weight = \frac{Volume_{target}}{TMR[d_{target}]} \tag{4-1}$$

where $\mathrm{Volume}_{\mathrm{target}}$ is the volume of the target that is intercepted along the ray line of the pencil beam and $\mathrm{d}_{\mathrm{target}}$ is the depth at which the target is first intercepted along the ray line of the pencil beam. Although this backprojection technique yields only a crude approximation to the required beam weightings, accuracy is not that important at this juncture since these weightings will serve as input to an optimization routine that will determine the best plan.

Optimization is performed using simulated annealing, a method which mathematically models the annealing process of metals in which the many final crystalline configurations are possible depending on the rate of cooling [Boh86]. According to the general principles of statistical mechanics, any system that is cooled sufficiently slowly will seek its state of minimum energy. Assuming that the cooling rate is chosen correctly, simulated annealing will avoid local traps and minimize the objective function for a given situation.

The annealing process is mathematically modelled as a biased random walk that samples the objective function. The first sampling is performed using the objective function calculated using the beam weights obtained from the initial backprojection. A random pencil beam is then chosen, and a step of ten percent transmission (a beam "grain") is taken in a random direction. The objective function is then recalculated. This new step is always accepted if the new objective function is smaller than the first. If the new objective function is not smaller, however, there is still a finite probability of acceptance given by

$$p = e^{-\beta(\varphi_{new} - \varphi_{old})} \tag{4-2}$$

where φ is the objective function and β is inversely proportional to the temperature of the system. This probability of accepting a detrimental step follows directly from the statistical mechanics of annealing, in which the probability that the system will transit from a state of lower energy to one of higher energy is

$$p = e^{-\frac{\Delta E}{kT}} \tag{4-3}$$

where k is Boltzmann's constant (8.62 x 10^{-5} ev/K) and T is the absolute temperature of the system.

Conditional acceptance is unique to simulated annealing, and is the feature which makes it so powerful. Unlike purely downhill optimization methods which greedily accept local minima, the probability of accepting a bad move allows the system to step back out of a local minimum. As the temperature is decreased, the probability of accepting an uphill step is also decreased and the steps should become confined to the global minimum of the function. This is extremely important in radiotherapy optimization, since the solution space can be extremely complex and many local minima may exist near the global optimum solution. An example of this complexity can be seen in the fact that a single arc optimized by Peacock may have as many as 200 dimensions to randomly vary while it attempts to minimize the following average square deviation objective function

$$\begin{aligned} \varphi = & \sum_{i}^{n_{targets}} \left\langle \frac{(D_{\max_i} - D_{Rx_i})^2}{D^2_{\max_i}} \right\rangle \cdot weight_{target_i} + \\ & \sum_{j}^{n_{structures}} \left\langle \frac{D^2_{structure_j}}{D^2_{structure\,limit_j}} \right\rangle \cdot weight_{structure_j} \end{aligned} \tag{4-4}$$

where

n_x = number of targets or critical structures, weight$_x$ = user defined weight for each target or structure ($0.0 \leq$ weight ≤ 2.0) and

D_x = maximum target dose or dose goal for target i or structure j

The brackets (< >) denote an average over all i target voxels or j structure voxels. Obviously this function, in its attempt to achieve high consistent target dose and low critical structure dose, can contain a large number of local minima.

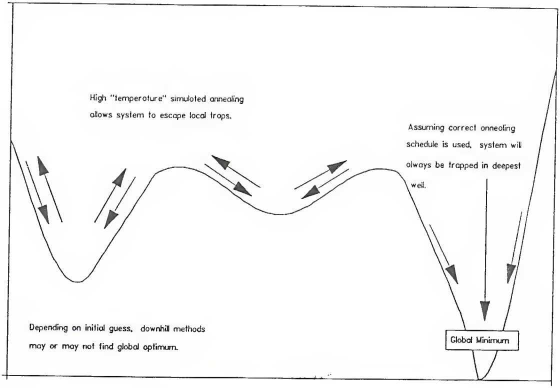
High "temperature" simulated annealing
allows system to escape local traps.
Assuming correct annealing schedule is used, system will always be trapped in deepest well.
Depending on initial guess, downhill methods
may or may not find global optimum.
Global Minimum

Figure 4-3: Downhill methods (dotted arrows) seek nearest well and are easily trapped in local minima. Conditional acceptance of bad steps allows simulated annealing (solid arrows) to escape these traps and find the best global solution.

Peacock Plan's optimization has some limitations, however. Although simulated annealing is widely accepted as a reliable optimization method, there are situations in which it can get trapped in local minima. The problem generally lies in the definition of an annealing schedule that cools the system sufficiently slowly. Success is often determined by the choice of annealing schedule, and the choice is quite often problem dependent [Pre91]. Given an infinite amount of time and iterations, simulated annealing can find the global optimum for any problem. For example, logarithmic cooling schedules have been proven to always approach the absolute minimum, but these schedules are far too slow for routine clinical use [Pre91]. In an effort to speed the optimization, Peacock Plan™ uses a simple inverse cooling schedule which results in an algorithm known as the Fast Simulated Annealing optimization method. At each iteration, the temperature is determined by

$$T = kT_0 \frac{10 \cdot n_{dimensions}}{n_{iterations}} \tag{4-5}$$

where kT_0 is set to 0.1 and $n_{iterations}$ is the number of iterations completed before this iteration. Using fast simulated annealing the plan may be computed in a reasonable amount of time, but there is also a possibility that the final result will actually be a local minimum rather than the global optimum solution.

Another limitation within the system is that Peacock Plan™ develops its 3D plan as a series of two-dimensional slices that overlap the target volume. Since optimization is such a slow process and computational time increases rapidly with the number of dimensions in an optimization, the optimization is performed on a slice by slice basis. After the beam weighting has been optimized for each slice, the dose is computed using a three-dimensional dose model. The inherent assumption is that the sum of optimized slice plans yields an optimized plan. This assumption, however, has not been proven.

The forward dose calculation algorithm uses measured finite size pencil beam data (MFSPB) and is based loosely on a model developed by Luxton for stereotactic radiosurgery [Lux91]. The actual calculation is

$$D(d,r,d_{isoc}) = TMR(d) \cdot OAR(r') \cdot \left[\frac{SAD^2}{STD^2} \right] \tag{4-6}$$

This model assumes that the MIMIC is composed of separate 1x1 cm pencil beams, each having the same off axis ratios (OAR) across the pencil. Tissue-maximum ratios (TMR), however, are assumed to vary for each pencil due to spectral changes across the beam axis, and separate TMRs must be measured for each pencil beam. SAD is the distance from source to isocenter distance, STD is the distance along the beam central axis and r' is the off axis distance of the calculation point from the central ray at depth d_{max} (assuming that OARs are measured at d_{max})and is equal to

$$r' = r \cdot \frac{(SAD + d_{isoc})}{STD} \tag{4-7}$$

where r is the actual off axis distance of the calculation point. Noticeably absent from the calculation is an output factor to account for field size dependence as multiple vanes are open during irradiation. This factor is implicitly included in the calculation since the off-axis ratio data are acquired in the penumbral region outside of the one centimeter width of the pencil beam in order to account for side scatter from each pencil beam. The doses from pencil beams are then summed and the penumbral overlap found in this summation accounts for the output factor (see Fig 4-4).

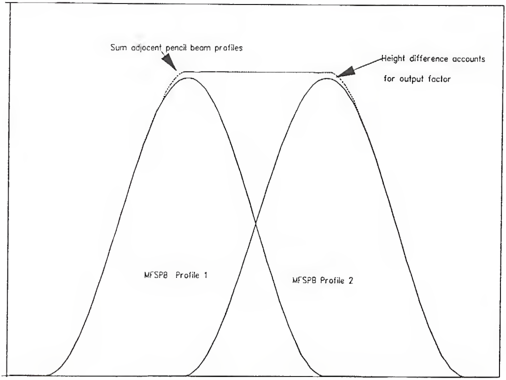
Sum adjacent pencil beam profiles
Height difference accounts for output factor
MFSPB Profile 1
MFSPB Profile 2

Figure 4-4: Overlap of measured finite size pencil beams yields effective output factor (field size dependence) when their profiles are summed.

Dose is calculated separately for each pencil beam using equation 4-6, and these doses are all summed. As with conventional treatment planning systems, the dose is then normalized to the maximum value within the calculation grid and two dimensional dose distributions may be superimposed on the reconstructed CT images in the axial, coronal and sagittal planes.

Verification of Dosimetry Algorithm

Peacock Plan^{TM} currently models beam data for the MIMIC attached to a 10 MV linear accelerator at Methodist Hospital in Houston, Texas. Experimental verification of the system was performed at Methodist Hospital [Gra94], and required production and execution of several different treatment planning scenarios. A cubic film phantom containing Kodak XV-2 film was placed in the beam during execution of the treatment plan, and film dosimetry was performed utilizing a Helium-Neon laser scanning densitometer. Two example plan verifications are illustrated in Figures 4-5 and 4-6: a small spherical treatment and a U shaped distribution, respectively. Isodose distributions on three planes are represented for each test to allow qualitative evaluation. The first shown is the central axis slice, while the other two plots represent planes that are ± 6 mm off of the central axis.

Recent quality assurance documents have recommended acceptable criteria for the uncertainty of treatment planning algorithms dependent upon the dose in the region of interest and the dose gradient within this region [Van93]. The primary criteria of concern are that the uncertainty not exceed ± 4% in a low dose gradient, high dose region and that positional uncertainty of isodose contours within a high dose gradient remain less than 4 mm [Van93]. VanDyk et al. define high dose as > 7% of the normalization (prescribed) dose, while a high dose gradient is defined as > 30%/cm. Data from the two cases presented are tabulated in Table 4-1. As seen in the table, data on the central axis slice is very good, while off axis the uncertainty increases. Also, it is suspected that the one very bad data point may be the result of positional errors during film readout.

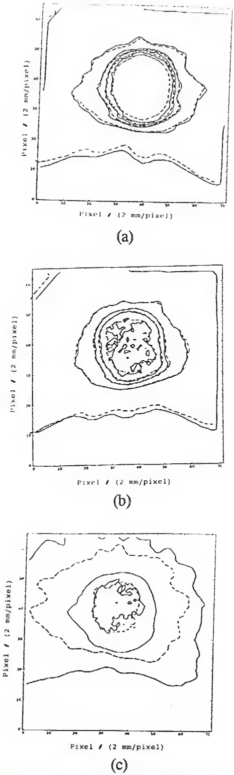

(a)

(b)

(c)

Figure 4-5: Isodose plots for a planned circluar distribution on (a) the central axis, (b) +6 mm off axis, and (c) -6 mm off axis. Dashed lines represent the planned distribution, while the solid lines were measured from XV-2 film.

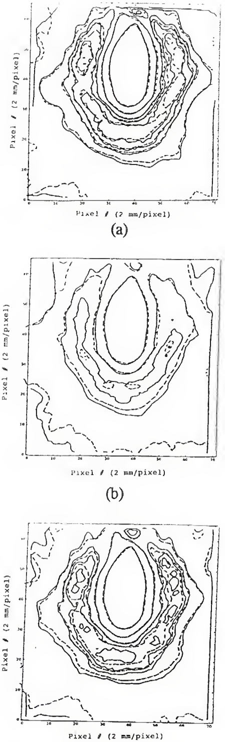

(a)

(b)

(c)

Figure 4-6: Isodose plots for planned U-shaped distribution on (a) the central axis, (b) +6 mm off axis, and (c) -6 mm off axis. Dashed lines represent the planned distribution, while the solid lines were measured from XV-2 film.

Table 4-1: Average uncertainties in Peacock Plan dosimetry for circle and U on the central axis (CA), 6 mm off the central axis and -6 mm off of the central axis for the treatment plan [Gra94].

	Circle CA	Circle 6 mm	Circle -6 mm	U CA	U 6 mm	U -6 mm
High dose, low gradient	1.86%	0.85%	12%	2.5%	4.5%	4.3%
High gradient	3.8mm	2.7mm	3.0mm	2.8mm	4.4mm	3.8mm
Total Volume	1.9%	0.8%	12.2%	2.2%	4.2%	3.6%

CHAPTER 5
TECHNIQUES FOR QUANTITATIVE PLAN EVALUATION

As conformal therapy techniques have developed, their ability to produce arbitrary dose distributions has been thoroughly investigated [Har94, Car93, Mos92, Hol94]. The true test of the utility of inverse radiotherapy planning will be in its ability to produce clinical treatment plans which are superior to those produced through conventional treatment planning. The comparison of such plans is quite difficult, however, due to the large amount of data which must be reviewed for a full three-dimensional evaluation [Kut91a]. Historically, treatment plan evaluation has been achieved through the graphical display of the two-dimensional dose distributions superimposed on the patient contour. In addition to these dose distributions, tools for quantitative plan evaluation have been developed. Some of these tools will be discussed in the following sections.

Dose Volume Histograms

Dose volume histograms effectively condense the dose distribution data by graphically displaying the volume of tissue irradiated through execution of a given treatment plan. There are two common forms for dose volume histograms which may be found in the literature: differential and cumulative. Differential dose volume histograms are plotted as histograms according to the mathematical definition, with dose binned along the abscissa and the height of each bin proportional to the volume of the organ which receives a dose within that range (see Figure 5-1). Alternatively, cumulative dose volume histograms are frequency distributions which represent the fractional volume of an organ receiving a dose greater than or equal to a specified dose as a function of dose (see Figure 5-2).

Since differential dose volume histograms represent the volume in each dose bin directly, they can facilitate comparison of dose intervals between rival plans. Also, the finer structure provided by true histograms offers more detail for quantitative analysis than that given by cumulative frequency distributions. The appearance of differential histograms can become confusing, however, when one attempts to use them for comparison of rival plans [Drz91]. Cumulative dose volume histograms can alleviate this problem when presented as smooth line graphs. Thus, cumulative dose volume histograms will be used as the graphic display for visual comparison of rival plans, while quantitative analysis of plans will require the finer structure provided by differential dose volume histograms. In order to remain consistent with the literature, the term dose volume histogram (DVH) will be applied to the cumulative frequency distribution [Kut92].

DVHs are generally computed for the target volume and each organ within the irradiated volume. Ideal DVHs for target and critical structure are shown in Figures 5-3a and 5-3b. Thus, DVHs for rival plans may be compared simply by plotting them on the same graph and noting how closely each approximates the ideal graph. This comparison can become muddled, however, if the DVHs cross each other as in Figure 5-4 so that it is not clear which histogram is better [Kut92]. The presence of multiple critical organs within the irradiated volume also increases the complexity of treatment

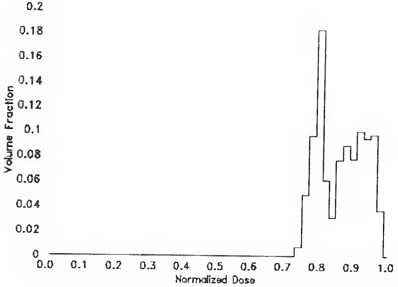

Figure 5-1: Example differential dose volume histogram for target volume.

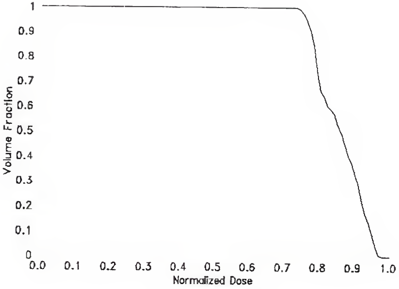

Figure 5-2: Cumulative DVH corresponding to Fig 5-1.

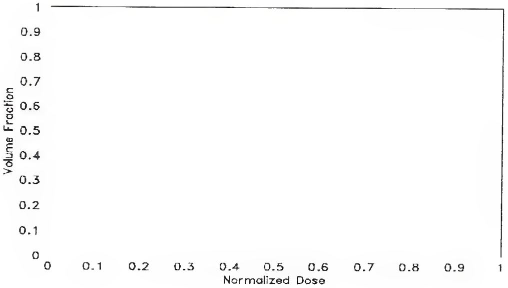

(a)

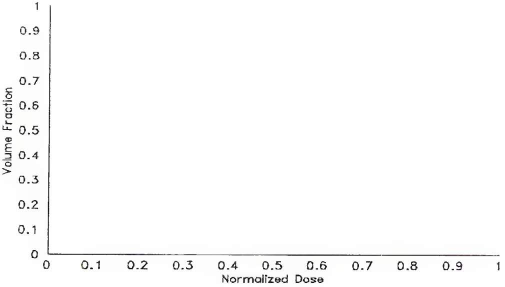

(b)

Figure 5-3: Ideal DVH for (a) target volume and (b) normal tissue volume.

plan comparison via DVHs. A further limitation of DVHs exists in their inability to provide spatial information regarding the location of hot and cold spots within the irradiated volume [Drz91]. Thus, if hot or cold spots are detected using a DVH, their position must be obtained through the use of spatial dose distributions. Nevertheless, dose volume histograms are a powerful tool for evaluation of many treatment planning situations due to their ability to condense a vast amount of information into a limited number of distributions.

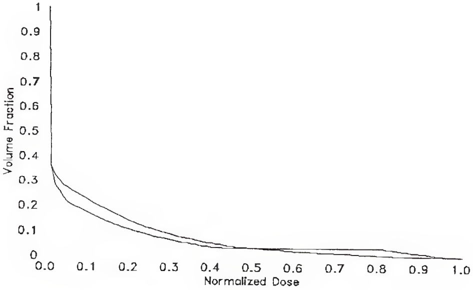

Figure 5-4: Crossing dose volume histograms for normal tissue volume.

Normal Tissue Complication Probability

Although DVHs provide very accurate information about the dosimetric properties of treatment plans, it may be difficult to infer the clinical significance from differences in rival DVHs [Kut92]. Therefore, a means of quantifying the clinical importance of rival plans is desireable. One method of quantifying the biological implications of a given treatment plan is to estimate the radiation toxicity to normal tissues through the calculation of normal tissue complication probabilities (NTCPs). Ideally, this calculation could then be balanced with the tumor control probability to provide an absolute numerical value which represents the validity of a given treatment plan [Moh92]. Unfortunately, these calculations are still under development and may provide probabilities which are highly uncertain. However, these calculations represent an attempt to model the clinical relevance of a given treatment plan and have proven worthwhile in the comparison of rival treatment plans [Kut92].

New models under development start from basic biological principles and should prove more accurate than current models [Jac93]. The most promising new model assumes that organs are comprised of functional subunits (FSUs), for example the kidney is comprised of nephrons, and the radiosensitivity of the organ depends on the radiosensitivity of the FSUs as well as their organization. FSU organization may be classified broadly as serial or parallel. Organs with a serial architecture have a chance of complication when a very small volume is irradiated since their function is disrupted if a single FSU is destroyed. Parallel organs have a threshold volume which must be irradiated before a complication arises since a certain number of FSUs must be destroyed before organ function is disrupted. Since many organs fall somewhere in between, their behavior is described using a parameter related to their relative seriality.

Since this model is still under development and many of the requisite parameters are unknown for specific tissues, NTCP may be calculated utilizing a four parameter model suggested by Lyman [Lym85] and used by the collaborative working group in their study [Kut91a]. This model estimates the complication probability arising from uniform irradiation of a partial organ by fitting a general sigmoidal function to the available clinical data for dose volume relationships. Although this model does not explicitly contain the radiological parameters of other models, all relevant radiobiological aspects are implicitly taken into account within the NTCP calculation [Lym85].

Two general sigmoidal functions have been investigated for analytic representation of the response of an organ to irradiation: a logistic function and the integrated standard normal distribution. It has been shown that these two functions differ by less than 0.9% over their entire range, however, so the choice is essentially irrelevant [Sch85]. Following the model originally proposed by Lyman, the integrated standard normal distribution may be used to determine the NTCP for an organ of volume V_{ref}, with partial volume V irradiated to a homogeneous dose D as

$$NTCP = \frac{1}{\sqrt{2\pi}} \int_{-\infty}^{t} e^{-0.5t'^2} dt' \qquad (5\text{-}1)$$

where t, the normal deviate, represents the number of standard deviations D is away from the tolerance dose and may be determined from

$$t = \frac{[D - TD_{50}(v)]}{TD_{50}(v) \cdot m} \;, \qquad (5\text{-}2)$$

where

$$v = \frac{V}{V_{ref}} \qquad (5\text{-}3)$$

and TD_{50} is the tolerance dose at which 50% of patients can expect a radiation related complication within five years after treatment. The partial and whole volume tolerance doses are related by a power law relationship [Sch83]

$$TD(v) = TD(V_{ref}) \cdot v^{-n} . \tag{5-4}$$

Two fitting parameters, n and m, which govern the volume and dose dependence of NTCP, respectively, may be found in a report by Burman et al. [Bur91]. Tolerance doses for a variety of organs were compiled by Emami et al. based on data available in the literature [Ema91]. The fourth parameter required by the model, V_{ref} can be obtained from the CT data if the entire organ is included in the scan, or alternatively, a standard value may be utilized. Data used for these calculations are shown in table 5-1.

In order to utilize this model for clinically realistic situations in which the organ is inhomogeneously irradiated, it is necessary to convert the nonuniform dose distribution into a uniform distribution. The effective volume histogram reduction method proposed by Kutcher et al. transforms a nonuniform differential DVH into a one step histogram with an effective volume V_{eff} and dose equal to the maximum dose of the histogram, D_M [Kut91]. Assuming that each volume element, V_i with dose D_i, of the differential DVH independently obeys the same dose volume relationship as the whole organ, each interval may be transformed into an effective volume with dose D_M through the power law relationship

$$V_{eff,i} = V_i \cdot (D_i/D_M)^{n^{-1}} . \tag{5-5}$$

This procedure is repeated for each interval of the dose volume histogram, and the total effective volume may be found from the sum of equation 5-5

$$V_{eff} = \sum_i V_i \cdot (D_i/D_M)^{n^{-1}} = \sum_i V_{eff,i} \ . \tag{5-6}$$

The effective volume, V_{eff}, found using this method may then be substituted for V in equations (5-2) through (5-4) in order to calculate the NTCP for inhomogeneous partial organ irradiation.

Table 5-1: Normal tissue endpoints and tolerance parameters [Bur91].

Organ	V_{ref}	n	m	TD_{50}	End Point
Bladder	Whole organ	0.5	0.11	80	Symptomatic contracture
Brain	Whole organ	0.25	0.15	60	Necrosis
Brain Stem	Whole organ	0.16	0.14	65	Necrosis
Femur	Whole organ	0.25	0.12	65	Necrosis
Heart	Whole organ	0.35	0.10	48	Pericarditis
Lens	Whole organ	0.30	0.27	18	Cataract
Lung	Whole organ	0.87	0.18	24.5	Pneumonitis
Optic Nerve	Whole organ	0.25	0.14	65	Blindness
Rectum	Whole organ	0.12	0.15	80	Proctitis/necrosis
Retina	Whole organ	0.20	0.19	65	Blindness
Skin	100 cm^2	0.10	0.12	70	Necrosis/ulceration
Spinal Cord	20 cm	0.05	0.17	66.5	Myelitis/necrosis

Tumor Control Probability

While minimizing normal tissue toxicity is an important goal of conformal therapy, it is also important to determine the probability of tumor sterilization using rival treatment plans. As with NTCP, currently there is no model which can provide an accurate assessment of the absolute tumor control probability (TCP). Models do exist, however, which should be useful in comparison of rival treatment plans that are similar in nature. The model used is based on that developed by Goitein [Goi94,Goi83] and Niemierko [Nie94] which assumes that the tumor consists of non-interacting clonogens which all must be killed in order to control the tumor. The probability of killing a clonogen after a single treatment fraction is estimated by determining the surviving fraction using the following variation of the linear quadratic formula

$$SF_d = SF_2^{\frac{d}{2}\cdot\left[\frac{\alpha/\beta+d}{\alpha/\beta+2}\right]} \tag{5-7}$$

where d is the dose per fraction to the clonogen, SF_2 is the probability that the clonogen will survive a dose of 2 Gy and α/β is the ratio of linear quadratic parameters which determine the curvature of the dose survival curve for a cell population. The clonogen's survival probability after undergoing n fractions may then be expressed as

$$SF = SF_2^{\sum_{k=1}^{n}\frac{d_k}{2}\cdot\left[\frac{\alpha/\beta+d_k}{\alpha/\beta+2}\right]} \quad . \tag{5-8}$$

The model further assumes that clonogens within an individual's tumor may differ in their radiation sensitivities, and this variation may be expressed as a gaussian distribution of $SF_{2,\mathrm{ind}}$ around the tumor mean with a standard deviation σ_{ind}

$$\overline{SF} = \frac{1}{\sqrt{2\pi}\,\sigma_{ind}}\int e^{-(\frac{SF_{2,ind}-\overline{SF}_{2,ind})^2}{2\cdot\sigma_{ind}^2}}\cdot SF\cdot d(SF_{2,ind}) \quad . \tag{5-9}$$

Assuming that a tumor is composed of NC clonogens, an individual's tumor control probability may then be calculated as

$$TCP_{ind} = e^{-NC\cdot\sum_{i=1}^{NB} v_i\cdot\overline{SF}_i} \tag{5-10}$$

where the sum is taken over the NB bins of the differential dose volume histogram, each with a fractional volume v_i. In addition to the intratumoral variation in cell sensitivities, Goitein's model also assumes there exists an interpatient heterogeneity which may be expressed as a gaussian distribution. Inclusion of this function yields the following final version of the TCP calculation

$$TCP = \frac{1}{\sqrt{2\pi}\cdot\sigma_{pop}}\int e^{-\frac{(\overline{SF}_{2,ind} - \overline{SF}_{2,pop})^2}{2\cdot\sigma_{pop}^2}}\cdot TCP_{ind}\cdot d(\overline{SF}_{2,ind}) \quad . \tag{5-11}$$

In order to perform the preceding calculation, certain biological parameters must be input. The first is the slope of the dose response curve, gamma-50, as defined by Brahme [Bra84]

$$\gamma_{50} = TCD_{50}\frac{d(TCP)}{dD}\bigg|_{D=TCD_{50}} \tag{5-12}$$

where TCD_{50} represents the dose required to achieve TCP of fifty percent. TCD_{50} is not a well known parameter, while gamma-50 has been tabulated for many tumors [Mun91a, Tha92]. Thus, it is often easier to reverse the calculation. For example, physicians can generally estimate the TCP for a treatment assuming that the entire tumor is homogeneously irradiated to the prescription dose. This dose is the TCD_{TCP}, or the dose required to eradicate TCP percentage of such tumors. Assuming that the values are on the linear portion of the dose response curve, the TCD_{50} can then be approximated from

$$TCD_{50} = TCD_{TCP_{est}} \cdot \frac{\gamma_{50}}{\gamma_{50} + 0.01 \cdot (TCP_{est} - 50)} \quad . \tag{5-13}$$

In addition to the dose response, the model requires a parameter, λ, which characterizes the variation of TCD_{50} with volume. The model also requires input of the linear quadratic parameters α and β, which have been tabulated for many tumors.

Using these input radiobiological parameters, all other parameters within the model can be easily calculated. Internal parameters calculated from these input values include the number of clonogens NC,

$$NC = ln2 \cdot 10^{\frac{TCD_{50}}{\lambda}} \tag{5-14}$$

and the surviving fraction at 2 Gy, SF_2

$$SF_2 = 10^{-2/\lambda} \quad . \tag{5-15}$$

After utilization of such a model to determine the TCP for a malignancy, Munzendrider et al. have observed that in regions of microscopic or suspected disease TCP is underestimated [Mun91a]. This is because there is a finite probability that no tumor exists in such regions, and thus there is non-zero probability of tumor control even with zero dose delivered to the region. To compensate for this possibility, the calculated probability is modified using

$$TCP = P_{no\ tumor} + (1 - P_{no\ tumor}) \cdot TCP_0 \tag{5-16}$$

where $P_{no\ tumor}$ is the probability that no tumor exists in the targeted region.

Dosimetric Statistics

As previously mentioned, the ideal radiotherapy treatment would result in homogenous irradiation of the targeted region to the prescribed dose. In general, however, it is physically impossible to homogenously irradiate the tumor while homogeneously sparing normal tissue. Thus, treatment of the entire lesion to the prescription dose produces hot spots within the volume. These hot spots can help destroy the lesion, but they can also damage or necrose the underlying tissue stroma and increase the risk of complications. For example, Nedzi et al. have correlated stereotactic radiosurgery tumor dose inhomogeneity and the corresponding increase in maximum tumor dose with increased complication rates [Ned91]. Unfortunately, this effect is not well understood and varies widely according to the type and location of tumor. For example, primary tumors located in the breast [Lim89] and larynx [Par94] have exhibited susceptibility to radiation damage from hot spots within the irradiated volume, while locations such as the nasopharynx [Par94] and prostate [Lei94, Per94] do not seem particularly sensitive to radiation dose escalation. Further, it is difficult to determine whether increased risk is due to necrosis of the target stroma or due to increased dose to surrounding normal tissue. Due to the vagueness of this problem, radiation oncologists typically avoid the situation by limiting the allowable target dose inhomogeneity and no method has been proposed for determining the probability of damaging the connective tissue and fine vasculature that may be associated with the target volume. Since the algorithm within Peacock Plan places no constraint on the dose inhomogeneity, large hot spots can result which complicate the comparison with rival conventional plans.

In order to provide some idea of dose inhomogeneity for plans presented in this work, dose statistics such as minimum dose, mean dose and maximum dose will be included. To further quantify the tumor dose inhomogeneity, researchers have often simply reported dose endpoints such as the D_{95}, which is the dose received by at least 95% of the region of interest and D_5, which is the dose received by at least 5% of this volume [Kut92]. Presentation of such data provides a clear indication of tumor coverage and the magnitude of hot or cold spots within the tumor volume and critical structures, and should help clarify the information found in DVHs and previously described biologically based statistics. While these statistics do not provide an absolute score to ease plan comparison, they do provide enough information that a physician can easily discern whether or not he is comfortable with the use of a given treatment plan.

Biologically Normalized Dose Fractionation

Dosimetric information for NTCP and TCP calculations is entered through differential dose volume histograms as described previously. Normal tissue tolerance has only been tabulated for conventional fractionation schedules of 180-200 cGy [Ema91]. In addition, the NTCP and TCP calculations are valid only if the dose per fraction is equal at each calculational point [Nie94]. In order to account for differences in fractionation schedules and the radiosensitivity of various tissues, a biologically normalized dose volume histogram (BNDVH) may be calculated from the differential dose volume histogram, and then input into the TCP calculation [Nie92]. This transformation follows directly from a manipulation of the linear quadratic formula which yields the following rule of thumb for the dose response of tissue to variable fractionation schedules [Wit83]:

$$\frac{D'}{D} = \frac{d + \alpha/\beta}{d' + \alpha/\beta} \tag{5-17}$$

where D is the total dose given in fractions of size d. The BNDVH normalizes the differential DVH to 2 Gy per fraction by using a variant of this calculation [Nie91]:

$$BND_i = D_i \cdot \frac{(d_i + \alpha/\beta)}{(2\,Gy + \alpha/\beta)} \tag{5-18}$$

where D_i is the dose for bin i of the differential DVH, d_i is the corresponding fractionated dose and BND_i is the total dose for bin i normalized to 2 Gy per fraction.

NTCP calculations for variable fractionation schedules require a modification of the TD_{50} in order to normalize these tolerance data to 2 Gy/fraction. For this work, the biologically normalized tolerance dose, $BNTD_{50}$, will be defined as:

$$BNTD_{50} = TD_{50} \cdot \frac{\alpha/\beta + 2\ Gy}{\alpha/\beta + d_{Rx}} \tag{5-19}$$

using the same manipulation of the linear quadratic equation as before. The TCD_{50} used for the TCP calculation in this work need not be similarly normalized, since this parameter is determined uniquely for each case subsequent to user input of pertinent data.

Although normalization of these data facilitates NTCP and TCP calculations for treatment schedules other than 2 Gy/fraction, it should be noted that such normalization contributes additional error to the probability calculations. This matters little for comparison of the rival plans in this study, since the fractionation schedules will remain constant for each comparison. Thus, normalization of these dosimetric parameters should enhance the realism of calculations for variable fractionation schedules, but discretion should be exercised when comparing calculated probabilities with those expected.

Score Functions

Although the tools discussed previously are very effective in condensing the amount of information required for treatment plan evaluation, a method of numerically scoring each plan such that a single number may quantify the merit of a given plan is desired to further reduce the amount of information. The simplest objective score function is the probability of uncomplicated tumor control [Sch85]. This function, although objective, is based on NTCP and TCP calculations, and is therefore limited in its ability to achieve an absolute probability. It is, however, a simple calculation that yields a single number with which to quantify the merit of a particular treatment plan. This score function, S, may be expressed as a product of the fractional probability of effect for each organ within the irradiated volume [Kut92]:

$$S = \prod_{i} (1 - P_i) \qquad (5\text{-}20)$$

where

$$P_0 = 1 - TCP \quad , \qquad P_{i>0} = NTCP \qquad (5\text{-}21)$$

Delivery Efficiency

In addition to dose conformity, any system clinically utilized must have the ability to deliver treatments quickly and efficiently. All methods of intensity modulation of the radiation beam will result in an increase in monitor units required for a treatment, and it is important to appreciate the effect this can have in clinical situations. The delivery efficiency of a conformal treatment system can be quantified via modification of an expression suggested by Galvin et al [Gal93]:

$$Efficiency = \frac{MU_{conventional\,Txplan}}{MU_{conformal\,Txplan}} \tag{5-22}$$

This efficiency factor reveals several features of the conformal treatment plan in relation to its conventional counterpart. First, beam on time increases linearly with an increase in monitor units, which possibly leads to a prolonged treatment session. Conformal treatment systems may, however, reduce time required for patient set up and compensate for this increased beam on time. Decreasing the delivery efficiency may have even more severe consequences on shielding requirements. A system which requires a large number of monitor units may effect linear accelerator design in terms of transmitted radiation through the primary and secondary collimators, as well as increase the leakage contribution to the room shielding requirements.

CHAPTER 6
CLINICAL TREATMENT PLANNING STUDIES

After consulting staff physicians at University of Florida, it was determined that several treatment sites could best demonstrate the potential benefit from conformal therapy and should be included in the clinical study; these sites and respective patient designations appear in Table 6-1. CT scans were obtained of the diseased region, and staff physicians delineated the regions of gross tumor and suspected disease. This volume has been designated the biological target volume (BTV) by the photon treatment planning collaborative working group [Smi91]. The physicians also designated any margin necessitated by set up uncertainties and organ motion. Including this margin around the BTV yields the mobile target volume (MTV).

Table 6-1: Treatment sites chosen for study and the respective patient designations.

Site	Patient Designations
Intracranial lesions treated stereotactically	SRS-1, SRS-2, SRS-3, SRS-4, SRS-5, SRS-6
Head and Neck	HN-1, HN-2
Intact Breast	B-1, B-2
Lung	L-1
Prostate	P-1, P-2

Three separate treatment plans were generated for each patient with the first being the conventional treatment plan as described in Chapter 3. These conventional plans were used for actual patient treatment, and thus represent the optimum plan as designed by the attending physician and dosimetrist or physicist. A 3D plan was then generated with traditional field arrangements but using the full volumetric CT information to design the fields instead of just a central axis slice. The conventional and 3D plans are the same for stereotactic radiosurgery and other virtual simulation applications, so only two plans were designed for these cases. The third and final plan is the conformal plan generated utilizing the Peacock Plan™ system.

Table 6-2: Default five table angle plan parameters for Peacock. Table angles are given using the 360 degree convention described in Figure 3-1.

Site	Table Angles (degrees)	Arc Length (degrees)
Head	0 30 & 330 60 & 300	290 245 215
Head and Neck	0 15 & 345 30 & 330	290 245 215
Abdomen/Thorax	0 15 & 345 30 & 330	290 245 215

All conformal plans generated using Peacock were designed using five table angles. When the user selects five table angles, Peacock starts with the default sets shown in Table 6-2, and determines the actual arcs used through its optimization process. Intuitively, the optimal dose gradient is obtained when the beam entrance points are evenly distributed over the entire surface of the patient. To approximate this, the treatment planning system starts with long arcs which can be altered by the system. Given a perfect optimization algorithm or alternatively a large amount of computer time, this is the best approach since beams which deleteriously effect the dose distribution will be discarded. However, experience with stereotactic radiosurgery has shown that when the irradiation geometry is reduced from 4-π it must be reduced to less than 2-π in order to avoid parallel opposed beams which decrease the steepness of the dose falloff [Pik90]. Since Peacock currently allows these opposing fields, suboptimal plans with a poor dose gradient can result. Since this effect was most obvious for the intracranial plans, these plans were all run utilizing the three different arc sets shown in Table 6-3: the Peacock default arc set, the Peacock set with shortened arcs and a default five arc set used in the University of Florida stereotactic radiosurgery program. These three plans were compared and the best was chosen. For one patient (SRS-3) the shortened arc sets never resulted in a plan which adequately conformed to the target and the default arc set was used. Comparing the dose gradient achieved with this plan (see Figure 6-6) with the dose gradient in other plans, the effect of the opposing fields becomes obvious. For all other plans, one of the shortened arc set plans was utilized.

Table 6-3: Arc sets used for planning intracranial cases in Peacock system.

Name	Table Angles	Arc Lengths
Peacock Default	0 30 & 330 60 & 300	290 245 215
Shortened Peacock Default	0 30, 60, 300 & 330	160 110
UF SRS Default	20, 55, 270, 305 & 340	100

Upon completion of the treatment planning process, Peacock specifies the minimum dose to the target. Although this could be chosen as the prescription isodose for the plan, the manufacturer suggests that the user slightly increase the prescription line which allows the prescription dose to slightly clip the target volume. This seems reasonable since the underdosed regions are generally comprised of individual voxels protruding from the delineated target and modern tumor dose response models have found a stronger correlation between mean tumor dose and TCP than between minimum target dose and TCP [Bra87, Kut92, Nie93]. Thus, by slightly increasing the prescription line, one can decrease the normal tissue dose and magnitude of hot spots within the tumor without profoundly effecting the probability of tumor control. In order to maintain consistency, all plans were prescribed to an isodose line which underdosed no more than 1.5% of the tumor volume.

As previously mentioned, three-dimensional planning generates a large amount of data which can complicate plan comparison. In order to condense this information, the quantitative tools discussed in Chapter 5 will be used along with displays of two dimensional slices through the lesion for selected representative patients. All treatment plans were designed to match the MTV, while target DVH and TCP calculations were performed for the BTV only. When viewing these plans it is important to remember that the conventional and conformal treatment planning systems contain inherent inaccuracies, and the dose calculations are not exact. This study is not designed to examine these inadequacies, but rather the clinical efficacy of inverse radiotherapy planning. If this method is deemed beneficial, then it will be appropriate to allocate the necessary resources to develop more sophisticated methods of dosimetry calculation. Following are the parallel planning studies for the chosen treatment sites.

Stereotactic Radiosurgery Patients

SRS-1 is a 40-year-old male with a centrally located posterior third ventricle area arteriovenous malformation (AVM). Conventional treatment was executed through a single isocenter plan using 9 arcs delivered through a 20 mm collimator to a total dose of 1500 cGy prescribed to the 80% isodose line. The conformal treatment plan achieved high target dose homogeneity with the prescription dose delivered to the 94% isodose line. The inferior dose gradient provided by the intensity modulation device, however resulted in a spread in the low isodose lines and a higher average critical structure dose. Although TCP calculations were not necessarily designed for AVMs, TCP was still calculated in order to provide relative scores for the rival treatment plans. For this and the other AVM examples, it is especially important to recall that TCP does not represent a true probability, but rather a quantitative evaluation of a proposed treatment plan.

Table 6-4: Conventional treatment plan designed for SRS-1.

Arc	Isocenter	Collimator	Angle	Arc Start	Arc Stop	Weight
1	1	20	10	30	130	1
2	1	20	30	30	130	1
3	1	20	50	30	130	1
4	1	20	70	30	130	1
5	1	20	350	230	330	1
6	1	20	330	230	330	1
7	1	20	310	230	330	1
8	1	20	290	230	330	1
9	1	20	270	230	330	1

SRS-2 is a 59-year-old female with metastatic adenocarcinoma of the lung to the right frontal lobe of her brain. A dose of 1750 cGy was delivered to the 80% isodose line through a nine arc single isocenter plan which used both the 20 and 24 mm collimators. Since the lesion is fairly spherical, it may be easily treated through conventional stereotactic radiosurgery using spherical collimators. The plan designed by Peacock is also quite conformal and treats the lesion with a more homogeneous dose distribution, although the average brain dose experiences a significant increase. This increase is partially offset by a decrease in the maximum brain dose, but still represents an undesirable increase.

Table 6-5: Conventional treatment plan for SRS-2.

Arc	Isocenter	Collimator	Table	Arc Start	Arc Stop	Weight
1	1	20	10	30	130	1
2	1	20	30	30	130	1
3	1	24	50	30	130	1
4	1	24	70	30	130	1
5	1	20	350	230	330	1
6	1	20	330	230	330	1
7	1	24	310	230	330	1
8	1	24	290	230	330	1
9	1	24	270	230	330	1

SRS-3 is a 62-year-old male with a left trigone AVM. Due to the highly irregular shape of the AVM nidus, the treatment plan generated utilizing the SRS software required two isocenters. The first isocenter consisted of nine arcs treated with a 24 mm collimator, while the second isocenter required 4 arcs using the 12 mm collimator. The resultant distribution from the combination of the two isocenters delivered 1500 cGy normalized to the 70% isodose line. Peacock again generated a homogenous distribution, but the overlapping and opposed fields also resulted in an inferior dose gradient.

Table 6-6: Conventional treatment plan for SRS-3

Arc	Isocenter	Collimator	Table	Arc Start	Arc Stop	Weight
1	1	24	10	30	230	1
2	1	24	30	80	130	1
3	1	24	50	80	130	1
4	1	24	70	100	130	2
5	1	24	350	230	280	1
6	1	24	330	230	280	1
7	1	24	310	230	280	1
8	1	24	290	230	260	1
9	1	24	270	230	260	2
10	2	12	10	10	130	1.5
11	2	12	30	10	130	1.5
12	2	12	350	230	330	1.5
13	2	12	330	230	330	1.5

SRS-4 is a 50-year-old female with 2 metastatic brain lesions. This patient provides an interesting test of the conformal radiotherapy system, since it has the ability to treat both lesions through a single isocenter. The conventional treatment plan required two isocenters consisting of 7 arcs each. Both isocenters utilized the 10 mm collimator, since the lesions were compact, and a dose of 1500 cGy was prescribed to the 80% isodose line. Peacock designed a plan which delivered the 1500 cGy to the 79% line. As can be seen from the statistics, the dose to critical structures (brain) is again increased in the

Peacock plan relative to conventional SRS planning. This two target plan illustrates one distinct advantage of inverse radiotherapy planning, however; the ability to treat multiple lesions using a single isocenter. Unfortunately, the MIMIC treats in a slice by slice manner and cannot take full advantage of this ability. Two dimensional modulation devices which treat the entire volume in one arc, however, could easily treat both lesions in one arc and increase delivery efficiency [Har94].

Table 6-7: Conventional treatment plan for SRS-4

Arc	Isocenter	Collimator	Table	Arc Start	Arc Stop	Weight
1	1	10	30	30	130	1
2	1	10	50	30	130	1
3	1	10	70	30	130	1
4	1	10	330	230	330	1
5	1	10	310	230	330	1
6	1	10	290	230	330	1
7	1	10	270	230	330	1
8	2	10	30	30	130	1
9	2	10	50	30	130	1
10	2	10	70	30	130	1
11	2	10	330	230	330	1
12	2	10	310	230	330	1
13	2	10	290	230	330	1
14	2	10	270	230	330	1

SRS-5 is a 73-year-old female with a right petroclival meningioma which presented a significant treatment planning challenge. The lesion was treated using a 3 isocenter plan with 15 total arcs and 4 separate collimators: 22, 26 and 12 mm, respectively. As is characteristic of multiple isocenter plans, there was significant dose inhomogeneity within the target volume and the dose was prescribed to the 70% isodose line. Due to the target's proximity to the brain stem, a relatively low target dose of 10 Gy was prescribed. The plan designed by Peacock provided better and more homogeneous target coverage than did the conventional plan, resulting in dose prescription at the 83% isodose level. It did, however result in a higher dose delivered to critical normal structures.

Table 6-8: Conventional treatment plan for SRS-5.

Arc	Isocenter	Collimator	Table	Arc Start	Arc Stop	Weight
1	1	22	10	50	80	1
2	1	22	350	230	260	1
3	1	22	330	230	260	1
4	1	22	310	240	300	1
5	1	26	290	260	310	1
6	1	26	270	260	310	1
7	1	26	70	50	80	1
8	2	12	10	60	90	.75
9	2	12	80	60	80	.75
10	2	12	350	230	290	.75
11	2	12	330	240	290	.75
12	3	12	10	60	90	.75
13	3	12	30	60	90	.75
14	3	12	350	240	290	.75
15	3	12	330	240	290	.75

SRS-6 is a 65-year-old male with an AVM located in the right anterior portion of the corpus callosum. Since the nidus was fairly compact and regular, treatment was delivered in a single isocenter with the 16 mm collimator through nine arcs. A dose of 1500 cGy was prescribed to the 80% line. Peacock designed a five arc plan which would deliver the 1500 cGy to the 89% line, thus lowering the tumor dose inhomogeneity and maximum brain dose.

Table 6-9: Conventional treatment plan for SRS-6.

Arc	Isocenter	Collimator	Table	Arc Start	Arc Stop	Weight
4	1	16	10	30	130	1
2	1	16	30	30	130	1
3	1	16	50	30	130	1
4	1	16	70	30	130	1
5	1	16	350	230	330	1
6	1	16	330	230	330	1
7	1	16	310	230	330	1
8	1	16	290	230	330	1
9	1	16	270	230	330	1

Since NTCP calculations for brain irradiation were formulated based on data from large field irradiation using conventional fractionation schedules, the NTCP parameters may not be suitable for stereotactic radiosurgery. Data from Kjellberg et al. are commonly used as standards for choosing treatment doses in linear accelerator radiosurgery [Kje83]. It has been shown that their 1% isoeffect line for brain necrosis from treatment with x rays and protons closely matches the 3% isoeffect line for brain necrosis from linear accelerator radiosurgery [Fli90]. Further, all patients with permanent radiation induced complications in the University of Florida series received doses above this line [Fri92]. As shown in Figure 6-1, NTCP calculations using the model parameters found in the literature underestimate the actual complication probability. In an attempt to force the NTCP calculations to better fit the radiosurgery data in the literature, the NTCP model parameters were modified using a simulated annealing optimization algorithm. This computer program varied the parameters governing dose (m) and volume (n) dependence to provide the best fit to Kjellberg's 1% necrosis line over the range of doses and collimators of interest. As shown in Figure 1, calculations using the modified parameters provide a much better fit to the Kjellberg's curve although the slope of the predicted isoeffect line is still less than expected.Thus, NTCP calculations for stereotactic brain irradiation were performed using these modified parameters. Results of these planning studies are shown in Figures 6-2 through 6-14.

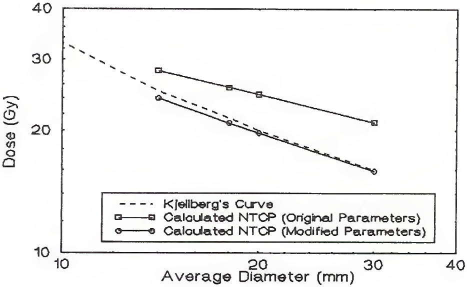

Figure 6-1: Kjellberg's isoeffect curve for 1% brain necrosis compared to 3% isoeffect curves obtained from NTCP calculations using parameters (n and m) found in the literature and modified parameters.

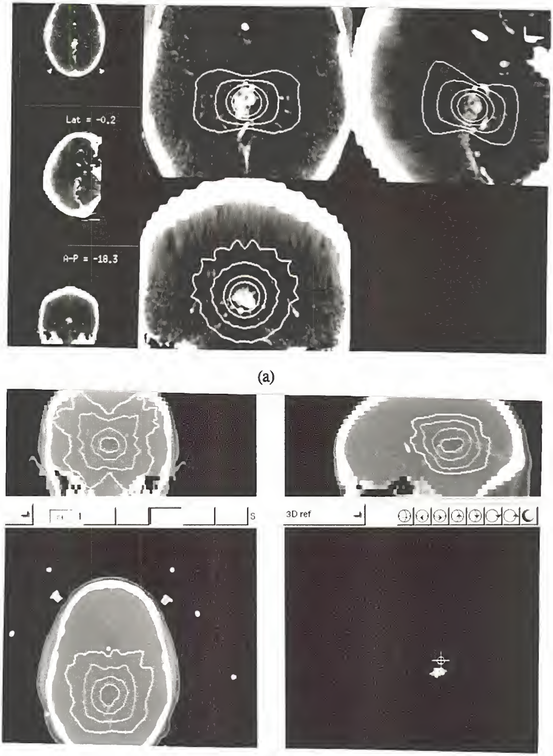

(a)

(b)

Figure 6-2: 15, 7.5, 3 and 1.5 Gy isodose lines are superimposed on axial, sagittal and coronal slices through isocenter from (a) conventional and (b) conformal plans for SRS-1.

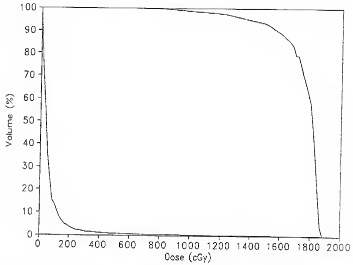

	Min	D_95	Mean	D_5	Max	NTCP/TCP
AVM	780.4	1387.5	1739.9	1856.3	1875.0	81.5
Brain	0.0	3.2	51.6	161.2	1866.1	1.1
					Score	80.5

(a)

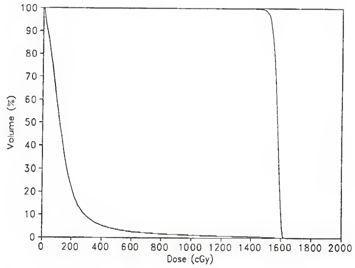

	Min	D_95	Mean	D_5	Max	NTCP/TCP
AVM	1362.9	1524.5	1566.6	1604.4	1612.9	80.8
Brain	0.0	8.2	150.7	405.7	1596.8	1.9
					Score	79.3

(b)

Figure 6-3: DVH and statistics for (a) conventional and (b) conformal plans for SRS-1.

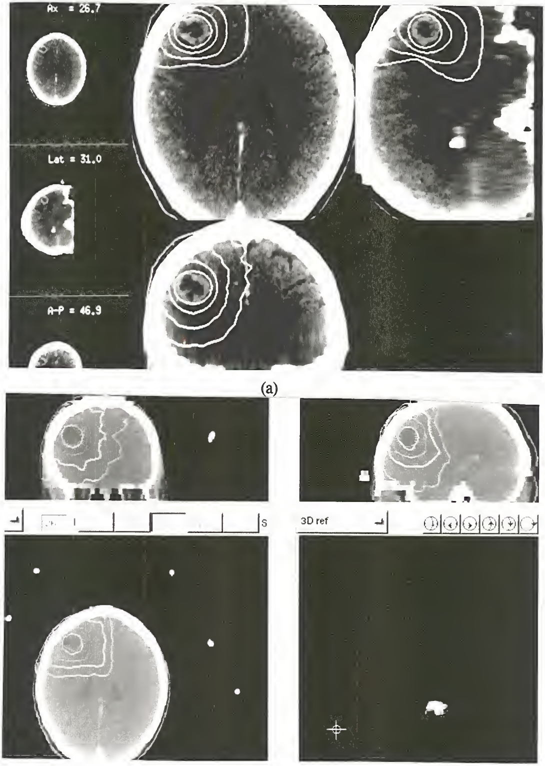

(a)

(b)

Figure 6-4: 17.5, 8.75, 3.5 and 1.75 Gy isodose lines are superimposed on orthogonal slices through isocenter from (a) conventional and (b) conformal plans for SRS-2.

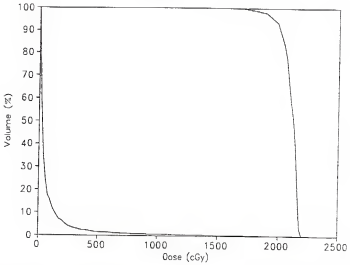

	Min	D_95	Mean	D_5	Max	NTCP/TCP
Target	1708.9	1950.0	2090.7	2175.0	2187.5	78.8
Brain	0.0	2.4	55.2	225.9	2121.4	2.5
					Score	76.8

(a)

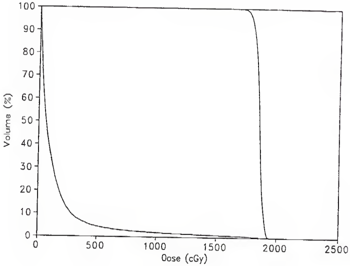

	Min	D_95	Mean	D_5	Max	NTCP/TCP
Target	1673.1	1779.3	1843.5	1903.2	1923.1	77.1
Brain	0.0	8.0	126.2	442.3	1884.6	3.3
					Score	74.5

(b)

Figure 6-5: DVH and statistics for (a) conventional and (b) conformal plans for SRS-2.

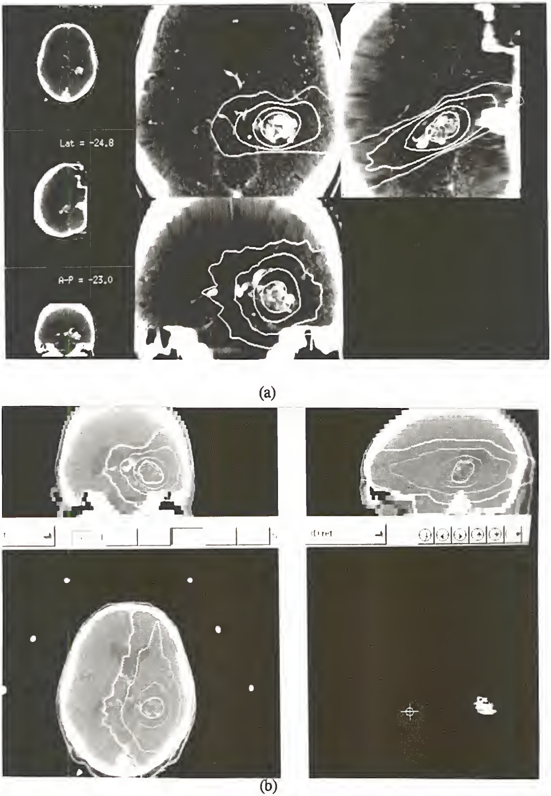

(a)

(b)

Figure 6-6: 15, 7.5, 3 and 1.5 Gy isodose lines are superimposed on axial, sagittal and coronal slices through isocenter from (a) conventional and (b) conformal plans for SRS-3.

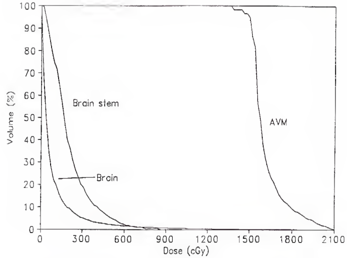

	Min	D_95	Mean	D_5	Max	NTCP/TCP
AVM	1362.9	1493.8	1601.8	1908.7	2130.8	81.0
Brain	0.0	3.0	77.5	320.0	2074.5	1.8
Brain Stem	19.4	29.1	193.6	514.6	853.1	0.0
					Score	79.6

(a)

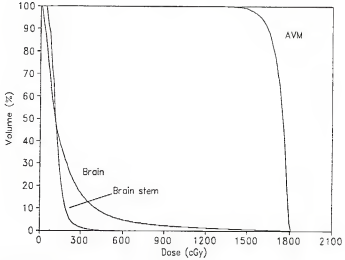

	Min	D_95	Mean	D_5	Max	NTCP/TCP
AVM	1292.2	1593.8	1724.5	1795.8	1807.2	81.5
Brain	0.0	21.6	179.8	564.8	1798.2	3.2
Brain Stem	36.1	46.2	120.1	217.4	533.1	0.0
					Score	78.8

(b)

Figure 6-7: DVH and statistics for (a) conventional and (b) conformal plans for SRS-3.

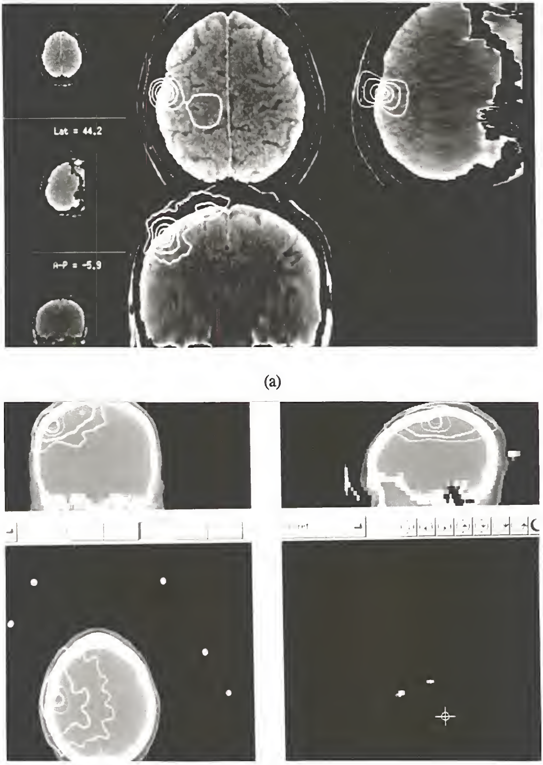

(a)

(b)

Figure 6-8: 15, 7.5, 3 and 1.5 Gy isodose lines are superimposed on orthogonal slices through isocenter one for (a) conventional and (b) conformal plans for SRS-4.

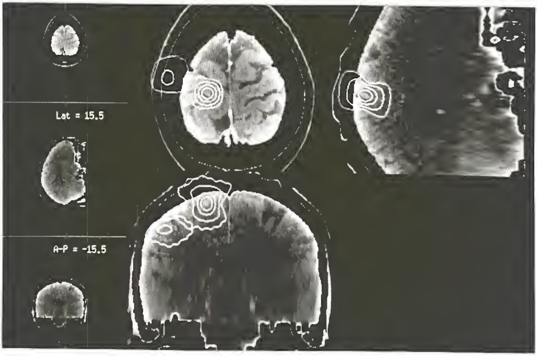

(a)

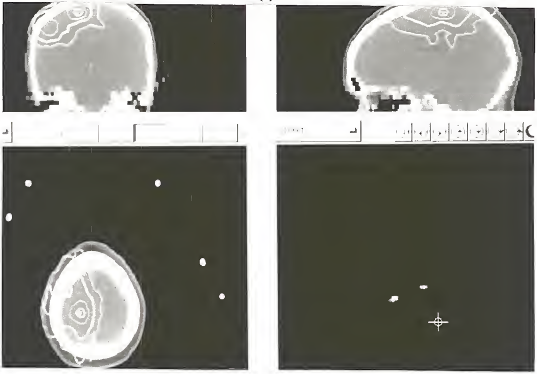

(b)

Figure 6-9: 15, 7.5, 3 and 1.5 Gy isodose lines are superimposed on orthogonal slices through isocenter two from (a) conventional and (b) conformal plans for SRS-4.

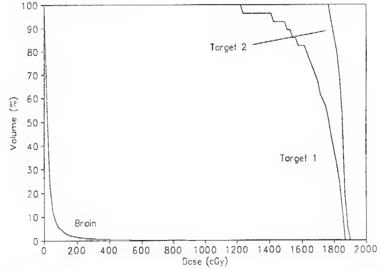

	Min	D_95	Mean	D_5	Max	NTCP/TCP
Target 1	1222.1	1395.0	1684.8	1824.8	1824.8	81.3
Target 2	1741.1	1753.1	1808.9	1858.3	1858.3	82.8
Brain	0.0	0.0	24.9	24.9	1832.1	0.9
					Score	66.7

(a)

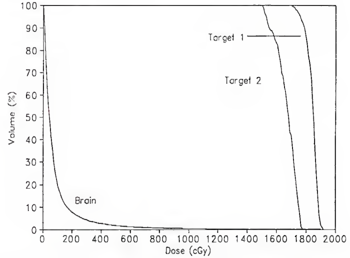

	Min	D_95	Mean	D_5	Max	NTCP/TCP
Target 1	1598.3	1652.8	1726.9	1780.2	1785.7	81.9
Target 2	1410.8	1437.1	1563.9	1654.2	1660.7	79.9
Brain	0.0	5.6	71.3	254.5	1750.1	1.4
					Score	64.5

(b)

Figure 6-10: DVH and statistics for (a) conventional and (b) conformal plans for SRS-4.

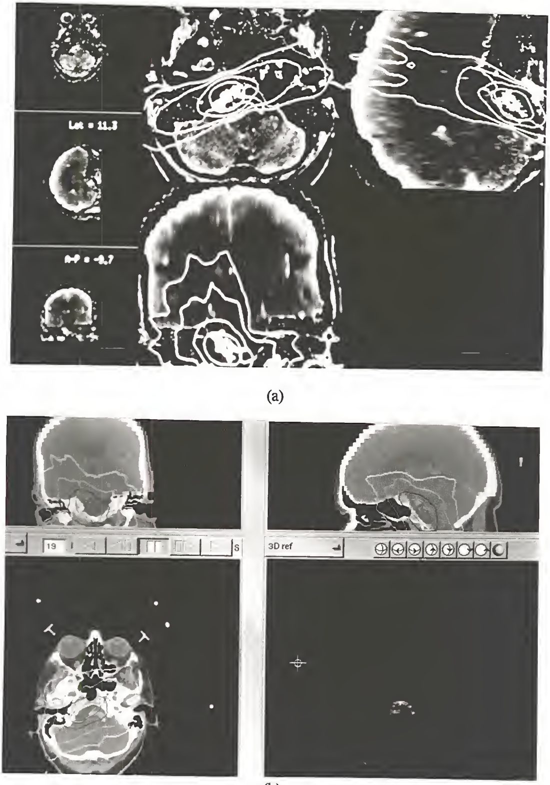

(a)

(b)

Figure 6-11: 10, 5, 2 and 1 Gy isodose lines are superimposed on axial, sagittal and coronal slices through isocenter from (a) conventional and (b) conformal plans for SRS-5.

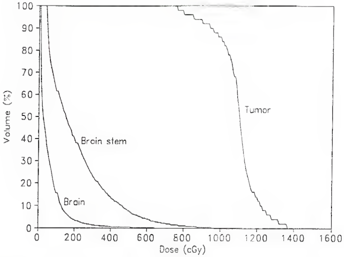

	Min	D_95	Mean	D_5	Max	NTCP/TCP
Tumor	776.8	857.1	1088.3	1285.7	1372.8	92.1
Brain	0.0	7.7	50.9	174.1	1044.6	0.6
Brain Stem	46.9	43.0	304.2	565.0	957.6	0.9
					Score	90.7

(a)

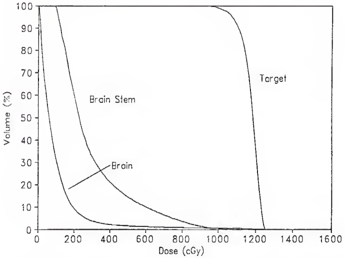

	Min	D_95	Mean	D_5	Max	NTCP/TCP
Tumor	925.0	1072.1	1171.0	1236.7	1250.0	94.4
Brain	0.0	9.5	88.8	256.3	1237.5	0.9
Brain Stem	93.8	110.0	292.3	746.4	1075.0	3.7
					Score	90.2

(b)

Figure 6-12: DVH and statistics for (a) Conventional and (b) conformal plans for SRS-5.

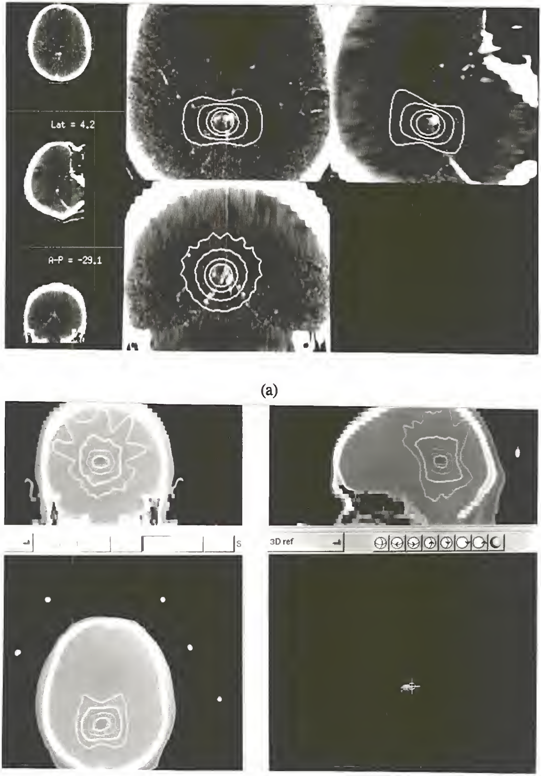

(a)

(b)

Figure 6-13: 15, 7.5, 3 and 1.5 Gy isodose lines are superimposed on axial, sagittal and coronal slices through isocenter from (a) conventional and (b) conformal plans for SRS-6.

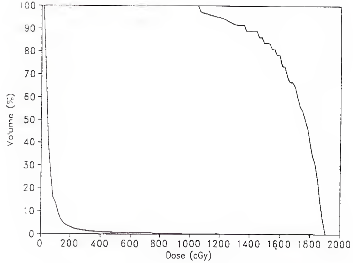

	Min	D_95	Mean	D_5	Max	NTCP/TCP
AVM	1037.9	1200.9	1661.1	1858.3	1875.0	81.2
Brain	17.0	19.6	56.2	152.7	1815.2	1.2
					Score	80.3

(a)

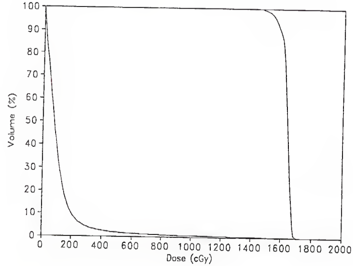

	Min	D_95	Mean	D_5	Max	NTCP/TCP
AVM	1441.0	1555.9	1628.8	1676.6	1685.4	81.1
Brain	0.0	6.9	100.9	273.1	1677.0	1.5
					Score	79.9

(b)

Figure 6-14: DVH and statistics for (a) Conventional and (b) conformal plans for SRS-6.

Head and Neck Carcinoma

The first patient studied (HN-1) is a 66-year-old female diagnosed with a T_4 left maxillary sinus adenoid custic carcinoma. Due to the extensive nature of her disease, she was not a viable candidate for surgery, and thus underwent a course of radiotherapy. She was treated to a dose of 7480 cGy in 68 fractions employing a twice daily fractionation schedule with 6 MV photons. A three field technique (AP and laterals) with wedges was used and the portals were reduced at 5060 cGy in order to reduce normal tissue toxicity. Through BEV planning the radiation portals can be designed to better match the target volume thus better sparing normal tissue and avoiding tumor underdosage. The Peacock plan further spares normal tissue, but results in a fairly significant tumor dose inhomogeneity with the dose prescribed to the 74 percent isodose line. Results of conventional, BEV and conformal plans are shown in Figures 6-15 through 6-20.

HN-2 is a 17 year-old female who suffered from T_4N_{3B} carcinoma of the nasopharynx. Using modern radiotherapy techniques, local control rates for nasopharynx carcinomas range from 80-90% for T_1 or T_2 primaries to about 50% for more advanced tumors [Kut91b]. Although this control rate is already very good using conventional techniques, the proximity of the nasopharynx to critical structures such as brain, brain stem, spinal cord and eyes leads to a high risk of complication from radiotherapy. Thus, it is attractive to use inverse radiotherapy planning in order to conformally avoid these critical structures. The conventional treatment plan required 7200 cGy in 60 fractions to the primary disease site delivered using mixed photon (^{60}Co) and electron (10 MeV) fields. In order to avoid exceeding tolerance dose to the spinal cord and brain stem, the photon fields were reduced twice during the course of treatment. Due to metastases in the lower neck nodes, the nodes on the right were prescribed to 7000 cGy while those on the left were prescribed to 6000 cGy. Thus, the treatment volume extended around the spinal cord in a horseshoe shape with the brain stem immediately posterior to the inferior portion of the primary disease site, presenting a formidable treatment planning challenge. Due to the complexity of this case, it was planned from the CT data and thus only the three-dimensional plan will be compared with the conformal treatment plan. Both the BEV and conformal plans contained a significant and comparable dose inhomogeneity, so direct comparison of the two is easier and possibly more meaningful than some of the other plan comparisons. As demonstrated in the statistics and histograms of Figures 6-21 and 6-22, the conformal system generated a plan that was far superior to that achieved even using BEV planning techniques.

Intact Breast

Intact breast treatments are performed using a modified version of the Joint Center technique [Sid81]. The Shands technique uses open and wedged tangential fields to treat the breast, chest wall and lower axilla, while open and wedged anterior fields are used to treat the upper axilla superclavicular regions. The anterior fields are rotated approximately 15^0 from vertical in order to avoid direct irradiation of the spinal cord [Sid81]. A rotatable half-beam block is used along with table and collimator rotations to match these fields. It is imperative that the field match is coplanar to avoid hot or cold spots which can effect cosmetic results or decrease the likelihood of local tumor control. Due to this field matching which must be accomplished in the simulation process, BEV planning was not utilized for breast cases. Typically, 6 MV photons are used since they produce a more homogenous dose distribution at shallow depths than can be achieved with higher energy beams.

Patient B-1 is a 72-year-old with stage T_1N_0 poorly differentiated infiltrating ductal carcinoma of the left breast. Her conventional treatment delivered 5000 cGy in 28 fractions with 6 MV open to wedged fields weighted 0.5:1. As can be seen in Figure 6-23, the posterior portion of the region targeted by the physician received a slight underdose while the remaining targeted volume received a homogenous dose. The plan designed by the Peacock system does not clip the target, but results in a significant dose inhomogeneity within the target. As previously mentioned, hot spots cause deleterious effects on the cosmetic results of radiation therapy for breast treatments. Data in the literature suggest that the TD_{50} for radiation fibrosis from overdose of the breast is approximately 80 Gy, and the incidence of fibrosis has little dependence on the volume irradiated [Arr93,Bor92,Lim89]. To account for this effect, NTCP calculations were performed for the tumor volume assuming an 80 Gy tolerance and the fitting parameters (n and m in the NTCP model) used for skin irradiation are appropriate for the risk of fibrosis. When viewing these statistics, one should also note the large increase in the TCP for the conformal case. Although this increase is computationally correct, it is an artificial inflation due to the large inhomogeneity within the targeted region. Since breast treatments have never been (and probably never will be) escalated to such a high dose, it is difficult to determine the accuracy of this calculated TCP.

Patient B-2 is a 50-year-old with stage T_2N_1 (II_B) poorly differentiated infiltrating ductal carcinoma of the left breast. Her primary course of radiotherapy was exactly the same as that for B-1, with 5000 cGy delivered in 28 fractions from 6 MV photons with open and wedged fields weighted 0.5:1. Figures 6-27 and 6-28 illustrate the conventional and conformal treatment plans for B-2. Results of these treatment plans were similar to those for B-1, with a slight underdose to a small portion of the breast using conventional techniques while the conformal technique again resulted in a significant dose inhomogeneity within the breast. Since no way to minimize this inhomogeneity currently exists within the Peacock software, this treatment modality is currently unacceptable for irradiation of the intact breast.

It is important to note that the dose calculation algorithms used for both the conventional and conformal techniques do not account for tissue inhomogeneities. Since both high density (ribs) and low density (lung) regions are in close proximity to the treatment volume, failure to account for these inhomogeneities can lead to significant error in dose calculation. It is assumed, however, that more sophisticated dose calculation algorithms can be utilized if inverse radiotherapy planning is considered advantageous. Thus, this study will concern itself more with the inverse radiotherapy technique and not the limitations of the specific dosimetry algorithm used.

Lung Cancer

L-1 is a 76-year-old male with a stage II_B undifferentiated sarcoma of the left upper lobe bronchus. The three-dimensional plan designed for treatment of the patient consisted of the use of 20 MV photons to a dose of 6400 cGy tumor dose delivered in

32 fractions through isocentric anterior and posterior treatment portals weighted 1:1. An off cord reduction was executed after 4400 cGy was delivered in 22 fractions. In addition, the patient received a 600 cGy high dose rate brachytherapy boost in 3 fractions. The contribution to the dose from this boost will be ignored for the analysis, and only the external beam treatments will be compared. The BEV treatment plan is shown in Figures 6-29 and 6-30, and obviously treats a large amount of normal tissue, most notably the left lung, spinal cord and trachea. Inverse radiotherapy planning, displayed in Figures 6-31 an 6-32, treats less normal tissue and results in lowered normal tissue toxicity. Any increased dose inhomogeneity is confined within the tumor and should have little effect on the clinical outcome.

As with breast treatments, failure to account for tissue inhomogeneities can cause significant deviation between the planned and actual dose distributions. Since neither planning system accounts for these inhomogeneities, one must be skeptical when viewing the dose distributions and realize they are not necessarily correct. Since the lung calculations are so uncertain, physicians often leave a large margin around the target and this may account for much of the extra normal tissue irradiated in the BEV treatment plan. If both systems accounted for tissue inhomogeneities, the calculated distributions would provide a truer representation of the actual dose distribution. The planned distributions are valid, however, for demonstration of the efficacy of inverse radiotherapy planning.

Carcinoma of the Prostate

P-1 is a 72-year-old with stage $T_{2a}B_{1n}$ adenocarcinoma of the prostate. The patient's treatment was designed to deliver 6840 cGy in 38 fractions from four equally weighted 20 MV photon fields: AP, PA and two lateral fields. These four fields were reduced at 5040 cGy in order to minimize the dose to nearby critical structures such as the bladder and rectum. Other structures of interest include both the right and left femoral heads which are in danger of necrosis since they are in the path of the lateral radiation beams. The resultant treatment plan is displayed in Figures 6-33 and 6-34.

Since prostate treatments are delivered using this four field "box" technique, the targeted region may easily be treated very homogeneously to a therapeutic dose. Use of this box technique, however, does not make any special attempt to avoid nearby critical structures. Through use of the beam's eye view display mode, one can tailor the four portals and lower the dose to critical structures while maintaining a homogenous target dose. Results of BEV treatment planning for P-1 is shown in Figures 6-35 and 6-36.

As is illustrated in Figures 6-37 and 6-38, the Peacock system can minimize the dose to critical structures near the prostate, but at the expense of dose homogeneity within the targeted volume where the prescribed isodose line for P-1 is reduced from the 97% line to the 81% line. While this failure of the software to minimize the tumor dose inhomogeneity is of concern, it should be irrelevant assuming that the inhomogeneity is confined within the targeted region. This is especially true for this example, since dose escalation studies which increase the prostate dose to approximately 80 Gy have shown no increase in morbidity when bladder and rectal doses are kept low [Lei92, Sof92].

P-2 is 71-years-old and has stage T_{1C} moderately differentiated adenocarcinoma of the prostate. His treatment was also a four field box which was designed to deliver 6400 cGy in 32 fractions from a 6 MV photon beam. The planned reduction was executed when the patient had received 4600 cGy in order to reduce normal tissue toxicity. Use of the lower energy beam leads to a larger volume of normal tissue irradiation, and this example clearly illustrates the rationale for high energy prostate therapy. Figure 6-39 shows results of the conventional treatment plan, which delivered a homogeneous dose to the prostate but resulted in underdosage of the seminal vesicles. Through BEV planning, displayed in Figure 6-40, this underdosage may be corrected while further sparing normal tissues and maintaining a homogeneous prostate dose. The inverse radiotherapy plan, depicted in Figure 6-41, results in further sparing of critical structures near the prostate, although the resultant dose distribution within the targeted region is rather inhomogeneous and prescribed to the 80% isodose line.

Discussion

Currently, state of the art inverse radiotherapy treatment planning provides no clinical advantage over stereotactic radiosurgery. Figure 6-42 graphically illustrates the difference in objective numerical score for the intracranial targets. For these small intracranial targets, inverse radiotherapy is nearly comparable to stereotactic radiosurgery but inverse plans generally result in a higher normal structure dose than conventional radiosurgery plans. This can be attributed to the fact that the dose gradient obtained using the MIMIC is far worse than can be achieved using small circular collimators. Careful examination of the dose distributions superimposed on axial slices reveals that

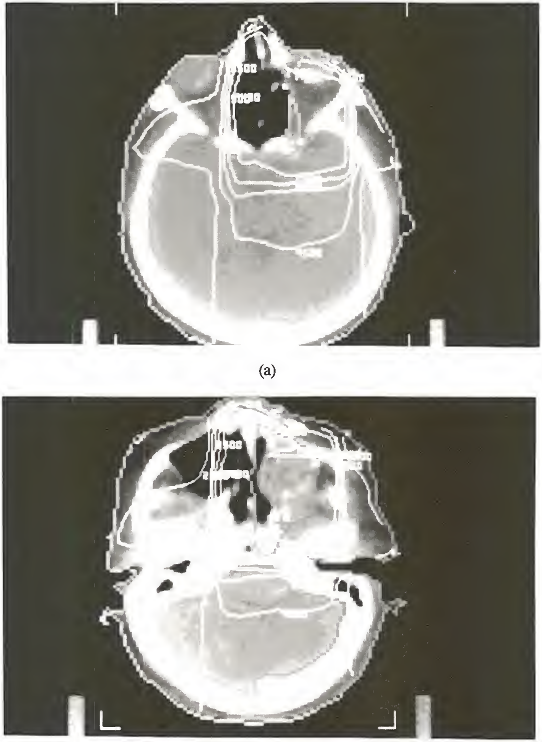

(a)

(b)

Figure 6-15: Conventional plan for HN-1. 74.8, 65, 55, 45 and 20 Gy isodose lines are superimposed on a) a slice 3 cm superior to the central axis and b) the central axis.

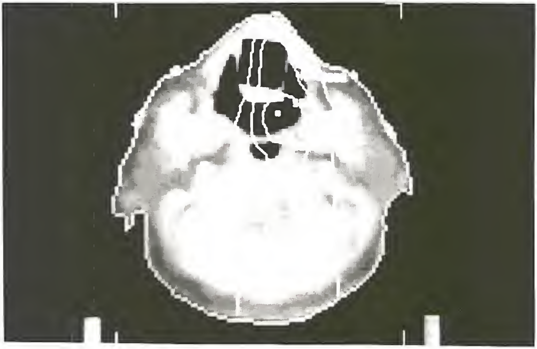

(c)

Figure 6-15--continued: (c) 3 cm inferior to central axis slice.

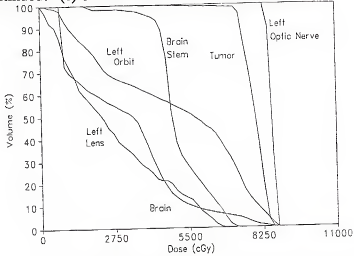

	Min	D_95	Mean	0_5	Max	NTCP/TCP
Tumor	3240.0	7393.3	7830.0	7443.2	8899.0	37.692
Brain	720.0	752.5	2985.1	7200.0	8640.0	0.708
Brain Stem	1620.0	4050.0	5036.2	6829.1	7200.0	0.406
Left Orbit	0.0	824.0	4785.8	8370.0	8640.0	14.185
Left Optic Nerve	8280.0	8365.7	8500.0	8640.0	8640.0	95.947
Left Lens	0.0	248.9	2560.3	6183.0	6660.0	97.726
					Score	0.029

Figure 6-16: Conventional plan dose volume histogram and statistics for HN-1.

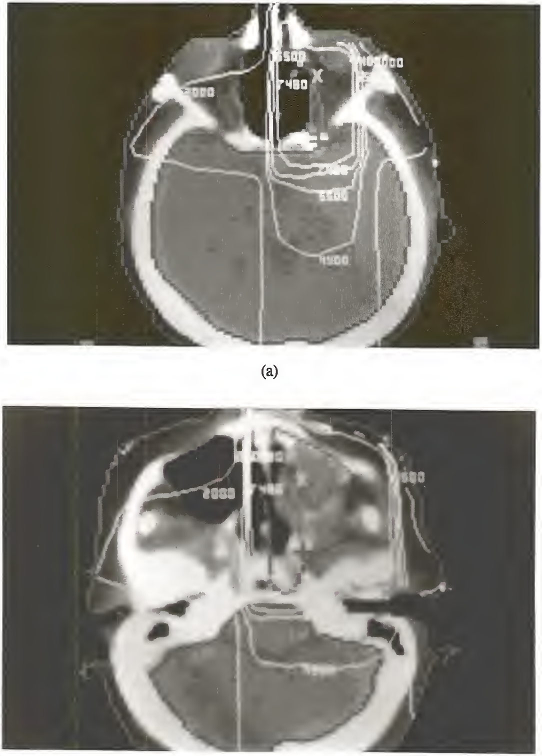

(a)

(b)

Figure 6-17: BEV plan for HN-1. 74.8, 65, 55, 45 and 20 Gy isodose lines are superimposed on a) a slice 3 cm superior to the central axis and b) the central axis.

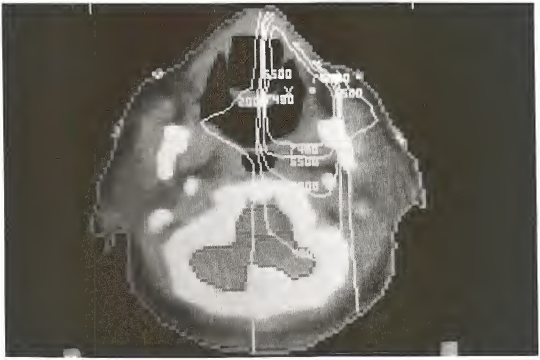

(c)

Figure 6-17--continued: (c) 3 cm inferior to central axis slice.

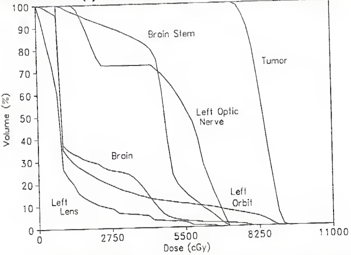

	Min	D_95	Mean	D_5	Max	NTCP/TCP
Tumor	7293.0	7657.4	8302.2	8980.0	9163.0	54.567
Brain	748.0	762.9	1774.3	4837.1	8041.0	0.029
Brain Stem	748.0	1700.0	4505.6	6564.7	7106.0	0.193
Left Orbit	0.0	749.9	1830.4	7974.3	8789.0	2.670
Left Optic Nerve	1309.0	1620.7	4744.0	6912.2	6919.0	4.051
Left Lens	0.0	135.5	1003.8	4145.2	6545.0	40.670
					Score	30.167

Figure 6-18: BEV plan dose volume histogram and statistics for HN-1.

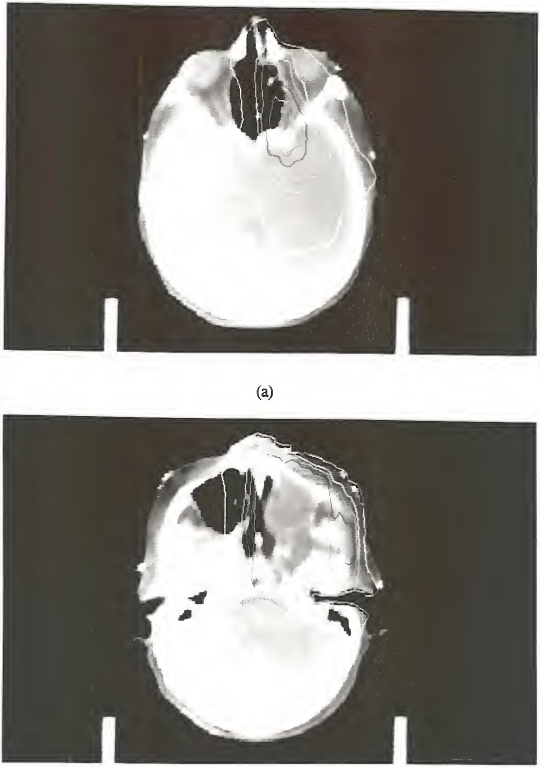

(a)

(b)

Figure 6-19: Conformal plan for HN-1. 74.8, 65, 55, 45 and 20 Gy isodose lines are superimposed on a) a slice 3 cm superior to the central axis and b) the central axis.

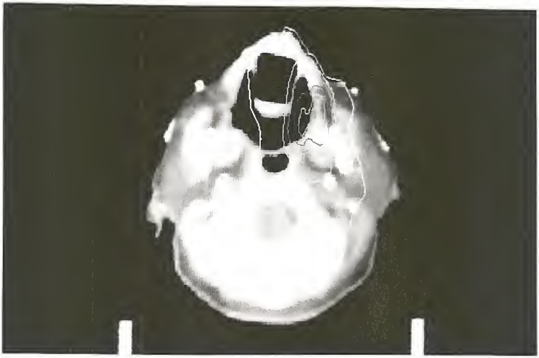

(c)

Figure 6-19--continued: (c) 3 cm inferior to central axis slice.

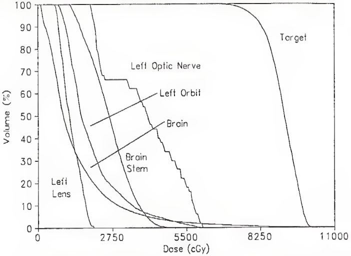

	Min	D_95	Mean	D_5	Max	NTCP/TCP
Tumor	6469.2	7950.7	9050.8	9874.7	10108.1	60.370
Brain	50.5	169.2	1354.1	4045.0	9552.2	0.014
Brain Stem	1112.0	1369.8	2606.2	4006.0	5035.1	0.000
Left Orbit	707.6	905.6	1946.0	4376.8	6014.3	0.050
Left Optic Nerve	1920.5	2009.0	3883.5	5938.5	6064.9	0.182
Left Lens	606.5	707.4	1181.5	1832.7	2021.6	1.544
					Score	59.292

Figure 6-20: Conformal plan dose volume histogram and statistics for HN-1.

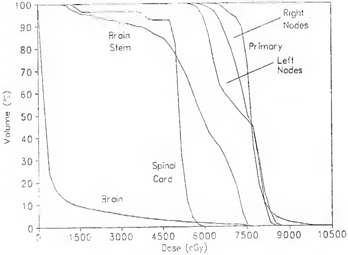

	Min	0_95	Mean	0_5	Max	NTCP/TCP
Primary	6155.1	6949.3	7606.5	8546.5	9729.0	80.430
Right Nodes	3772.5	6428.8	7409.1	8378.9	8537.7	65.056
Left Nodes	5360.9	5909.3	7075.4	8257.0	8339.1	75.375
Brain	0.0	24.0	511.5	3276.1	7544.9	0.000
Brain Stem	794.2	1985.5	5565.8	7346.4	7346.4	5.159
Spinal Cord	1191.3	3828.1	4859.9	5532.3	5758.0	1.041
					Score	37.016

Figure 6-21: BEV treatment plan DVH and statistics for HN-2.

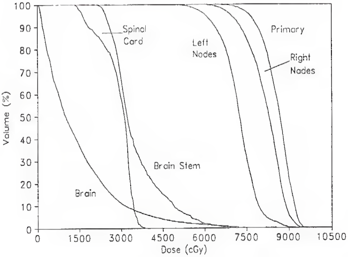

	Min	0_95	Mean	D_5	Max	NTCP/TCP
Primary	5568.0	7632.0	8478.1	9279.9	9600.0	91.831
Right Nodes	5760.0	6960.0	8162.3	9034.1	9456.0	69.448
Left Nodes	4848.0	6061.0	7192.5	8176.8	9216.0	75.572
Brain	0.0	135.3	1408.2	4176.0	8544.0	0.007
Brain Stem	2160.0	2459.9	3480.8	5502.4	7104.0	0.027
Spinal Cord	1344.0	1629.0	2879.4	3526.4	3840.0	0.010
					Score	48.175

Figure 6-22: Conformal treatment plan DVH and statistics for HN-2.

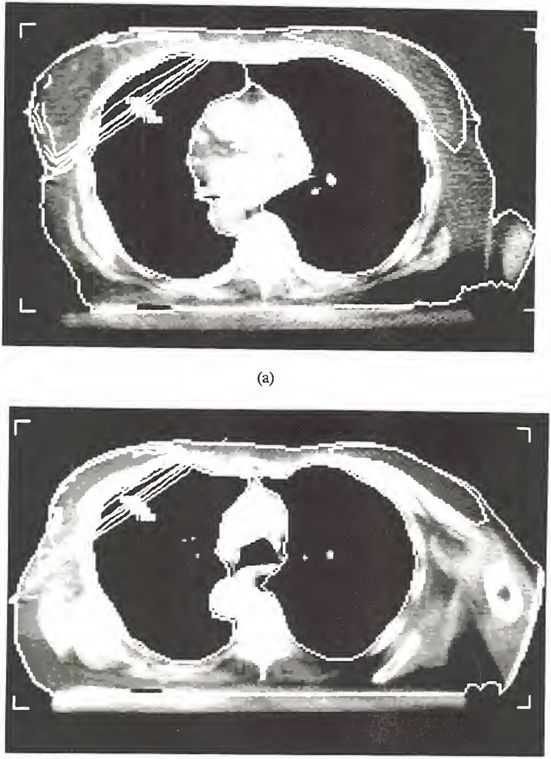

(a)

(b)

Figure 6-23: Conventional plan for B-1. 50, 45, 35, 25 and 10 Gy isodose lines are superimposed on the a) axial slice 3 cm superior to the central axis and (b) central axis.

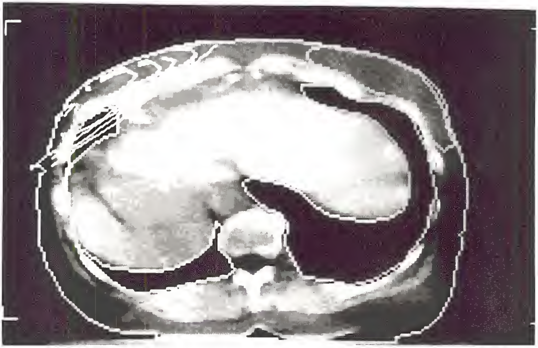

(c)

Figure 6-23--continued: (c) 4 cm inferior to the central axis.

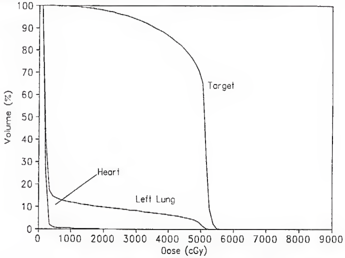

	Min	D_95	Mean	D_5	Max	NTCP/TCP
Target	224.0	2800.0	4701.4	5329.0	5568.0	71.061
Ipsilateral Lung	112.0	121.5	577.5	4575.0	5152.0	0.000
Heart	224.0	119.6	149.7	321.9	2352.0	0.000
Contralateral Lung	112.0	112.0	113.5	224.0	224.0	0.000
Contralateral Breast	0.0	0.0	110.9	224.0	224.0	0.000
Target (Fibrosis)	224.0	2800.0	4701.4	5329.0	5568.0	0.092
					Score	70.405

Figure 6-24: DVH and statistics resulting from conventional treatment plan for B-1.

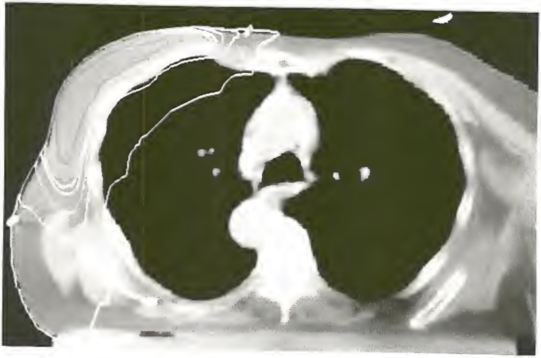

(a)

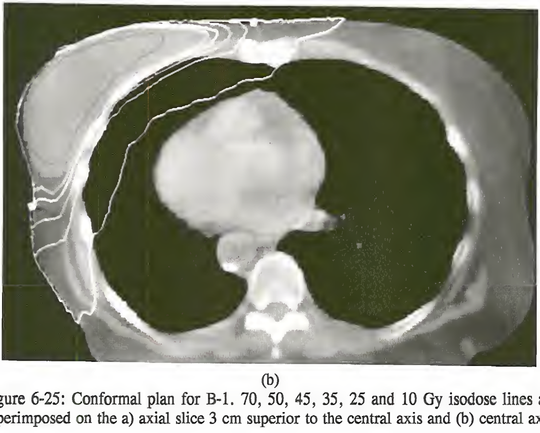

(b)

Figure 6-25: Conformal plan for B-1. 70, 50, 45, 35, 25 and 10 Gy isodose lines are superimposed on the a) axial slice 3 cm superior to the central axis and (b) central axis.

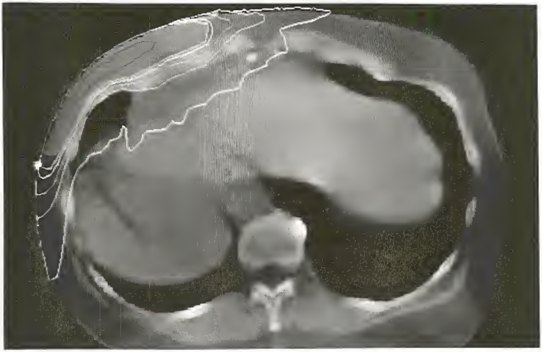

(c)

Figure 6-25--continued: (c) 4 cm inferior to the central axis.

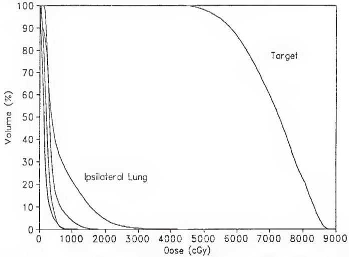

	Min	D_95	Mean	D_5	Max	NTCP/TCP
Target	3815.8	5401.1	7124.9	8482.5	8771.9	93.300
Ipsilateral Lung	0.0	57.1	607.8	1929.8	4166.7	0.000
Heart	87.7	183.0	358.8	921.1	1754.4	0.000
Contralateral Lung	0.0	26.3	142.0	438.6	1140.4	0.000
Contralateral Breast	43.9	66.9	215.3	508.7	877.2	0.000
Target (Fibrosis)	3815.8	5401.1	7124.9	8482.5	8771.9	96.200
					Score	3.546

Figure 6-26: DVH and statistics resulting from conformal treatment planning for B-1.

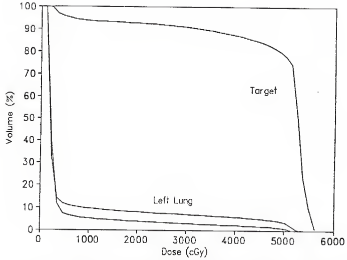

	Min	D_95	Mean	0_5	Max	NTCP/TCP
Target	117.0	604.5	4742.5	5562.0	5616.0	70.003
Ipsilateral Lung	117.0	125.7	517.3	4563.0	5265.0	0.000
Heart	117.0	126.7	337.4	1111.5	5148.0	0.000
Contralateral Lung	117.0	117.0	117.5	228.6	234.0	0.000
Contralateral Breast	0.0	0.0	0.0	0.0	0.0	0.000
Target (Fibrosis)	117.0	604.5	4742.5	5562.0	5616.0	0.116
					Score	69.922

Figure 6-27: DVH and statistics resulting from conventional treatment plan for B-2.

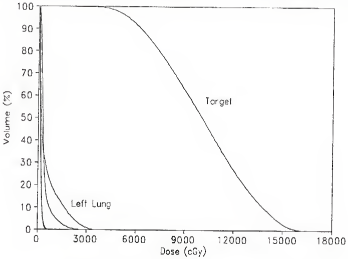

	Min	D_95	Mean	D_5	Max	NTCP/TCP
Target	2069.0	5732.0	10990.7	16226.3	17241.4	94.001
Ipsilateral Lung	0.0	18.1	469.5	2364.5	3793.1	0.000
Heart	0.0	92.9	278.9	1166.3	2586.2	0.000
Contralateral Lung	0.0	11.1	75.1	271.6	517.2	0.000
Contralateral Breast	0.0	15.8	113.2	366.3	689.7	0.000
Target (Fibrosis)	2069.0	5732.0	10990.7	16226.3	17241.4	100.000
					Score	0.000

Figure 6-28: DVH and statistics resulting from conformal plan for B-2.

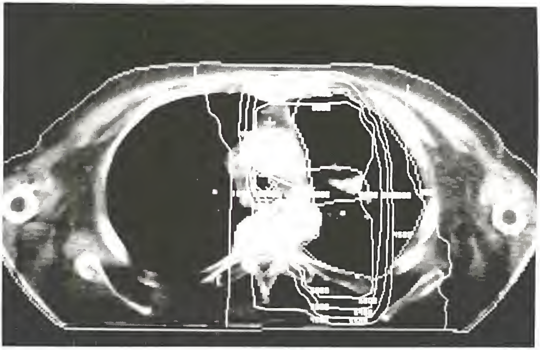

(a)

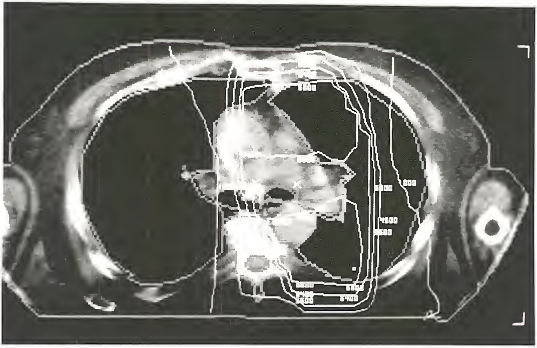

(b)

Figure 6-29: BEV plan for L-1. 68, 64, 55, 45 and 10 Gy isodose lines are superimposed on the a) axial slice 4 cm superior to the central axis and b) central axis.

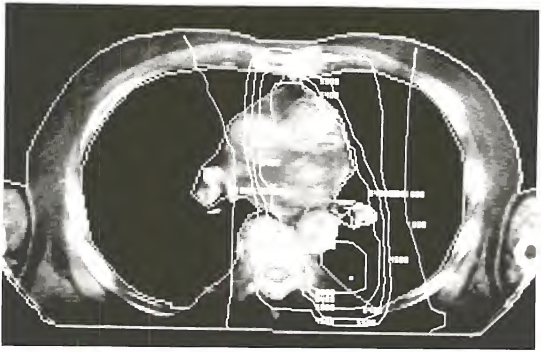

(c)

Figure 6-29--continued: (c) 3 cm inferior to the central axis.

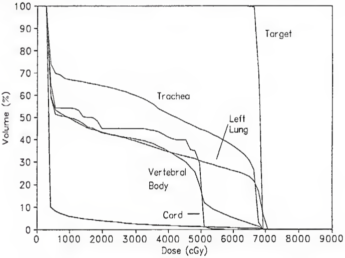

	Min	D_95	Mean	D_5	Max	NTCP/TCP
Target	6222.5	6666.8	6742.2	6788.2	6788.2	30.056
Ipsilateral Lung	282.8	300.3	2677.8	6929.6	7071.0	85.716
Trachea	282.8	309.9	3692.6	6776.0	6788.2	22.089
Contralateral Lung	282.8	290.7	465.6	1367.1	6929.6	0.000
Spinal Cord	282.8	302.9	2421.5	5072.8	5656.8	2.338
					Score	3.267

Figure 6-30: DVH and statistics resulting from BEV treatment plan for L-1.

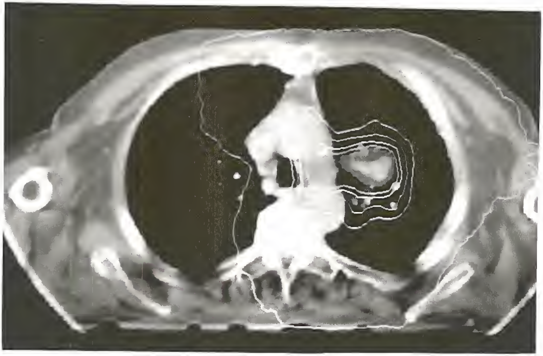

(a)

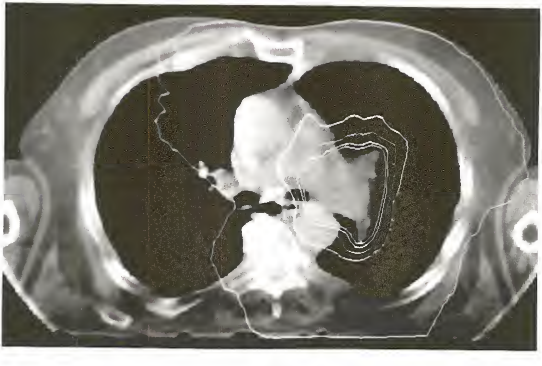

(b)

Figure 6-31: Conformal plan for L-1. 68, 64, 55, 45 and 10 Gy isodose lines are superimposed on the a) axial slice 4 cm superior to the central axis and b) central axis.

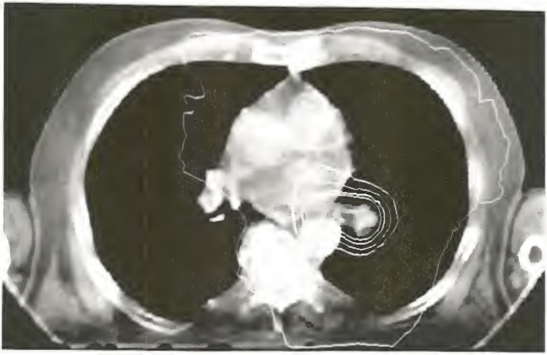

(c)

Figure 6-31--continued: (c) 3 cm inferior to the central axis.

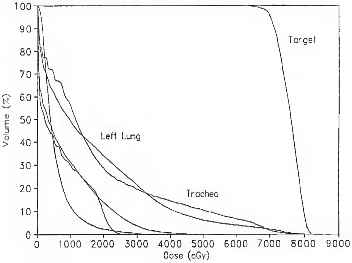

	Min	D_95	Mean	D_5	Max	NTCP/TCP
Target	6103.6	7018.3	7561.2	8048.4	8192.8	32.026
Ipsilateral Lung	0.0	17.4	1586.4	5135.1	7906.0	7.582
Trachea	0.0	27.2	1725.0	6395.7	7783.1	0.085
Contralateral Lung	0.0	112.3	523.4	1506.8	3727.7	0.000
Spinal Cord	0.0	6.5	649.1	2122.8	2457.8	0.000
					Score	29.573

Figure 6-32: DVH and statistics resulting from conformal treatment plan for L-1.

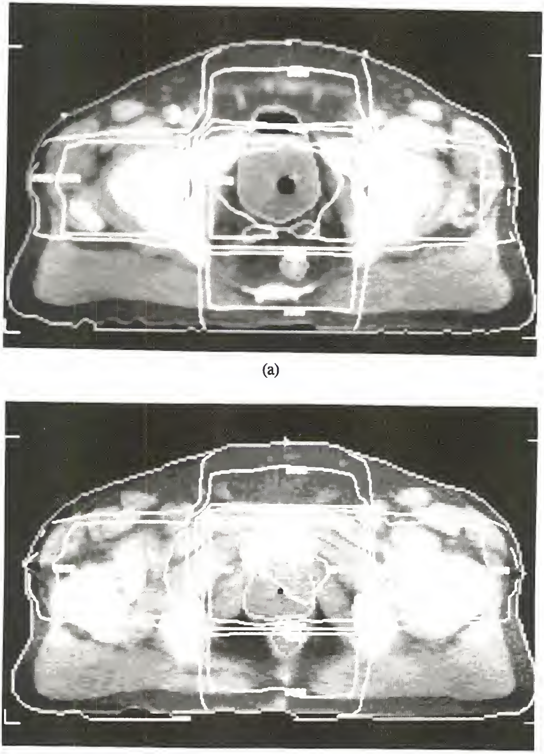

(a)

(b)

Figure 6-33: Conventional plan for P-1. 68.4, 55, 45, 35 and 20 Gy isodose lines are superimposed on the a) axial slice 3 cm superior to the central axis and b) central axis.

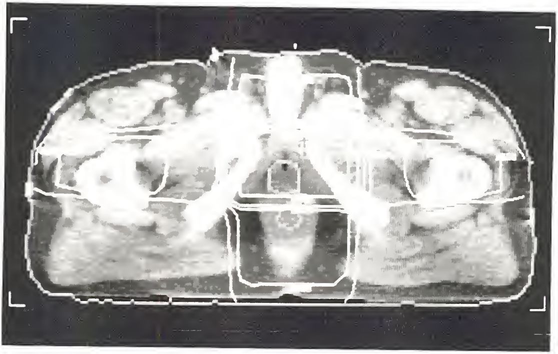

(c)

Figure 6-33--continued: (c) 3 cm inferior to the central axis.

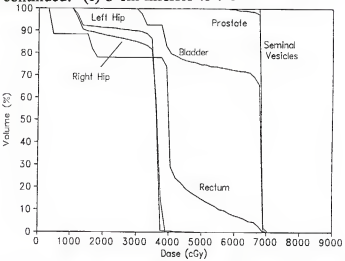

	Min	D_95	Mean	0_5	Max	NTCP/TCP
Prostate	5624.0	6843.6	6828.3	6984.9	7014.0	67.568
Seminal Vesicles	6840.0	6840.0	6843.2	6987.5	6992.0	77.356
Bladder	2888.0	3270.9	6009.2	6840.0	6840.0	0.697
Rectum	304.0	1793.2	3640.9	6612.0	6840.0	0.350
Right Hip	912.0	1216.0	3298.3	3800.0	3800.0	0.000
Left Hip	1064.0	1285.9	3361.9	3787.5	4712.0	0.000
					Score	51.722

Figure 6-34: DVH and statistics resulting from conventional treatment plan for P-1.

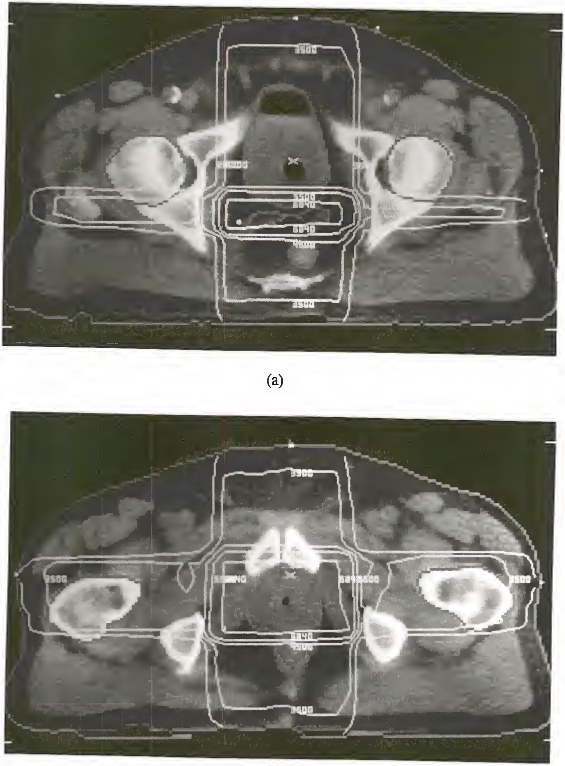

(a)

(b)

Figure 6-35: BEV plan for P-1. 68.4, 55, 45, 35 and 20 Gy isodose lines are superimposed on the a) axial slice 3 cm superior to the central axis and b) central axis.

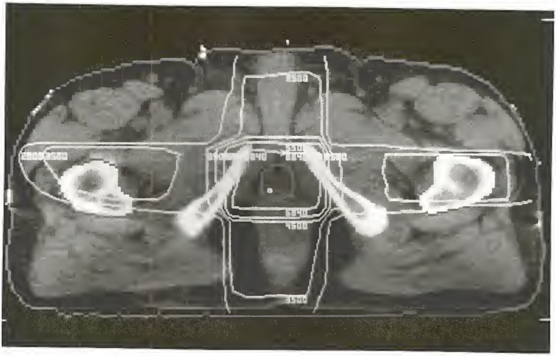

(c)

Figure 6-35--continued: (c) 3 cm inferior to the central axis.

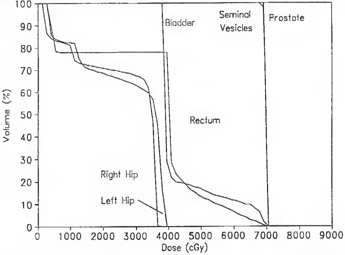

	Min	0_95	Mean	D_5	Max	NTCP/TCP
Prostate	6920.8	6920.8	6920.8	6920.8	7051.5	67.885
Seminal Vesicles	6779.5	6779.5	6917.9	6920.8	6920.8	77.513
Bladder	3813.5	3823.4	4260.1	6828.6	6920.8	0.000
Rectum	282.5	347.9	3485.7	6198.9	6920.8	0.277
Right Hip	282.5	331.1	2660.3	3813.5	3813.5	0.000
Left Hip	282.5	334.3	2726.5	3807.7	3813.5	0.000
					Score	52.474

Figure 6-36: DVH and statistics resulting from BEV treatment plan for P-1.

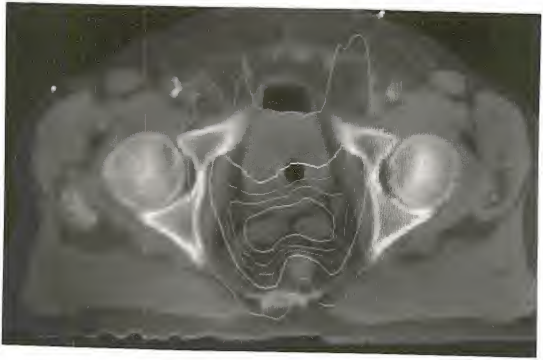

(a)

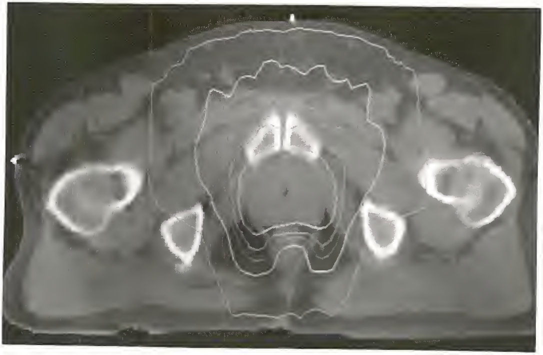

(b)

Figure 6-37: Conformal plan for P-1. 68.4, 55, 45, 35 and 20 Gy isodose lines are superimposed on the a) axial slice 3 cm superior to the central axis and b) central axis.

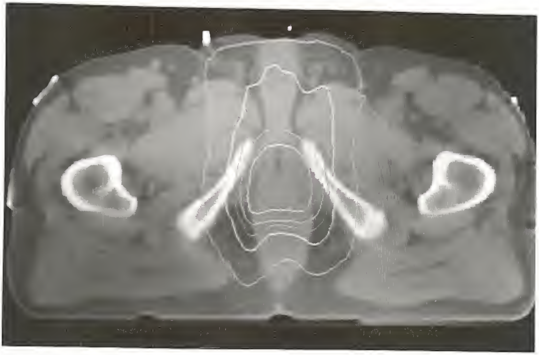

(c)

Figure 6-37--continued: (c) 3 cm inferior to the central axis.

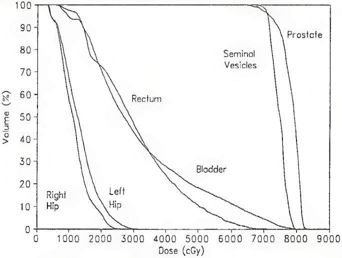

	Min	D_95	Mean	D_5	Max	NTCP/TCP
Prostate	6221.9	7152.1	7807.1	8174.5	8241.0	69.419
Seminal Vesicles	6716.4	7090.3	7427.8	7828.9	7911.3	78.278
Bladder	618.1	947.7	3190.1	6909.7	7952.5	0.000
Rectum	576.9	1259.5	3099.0	5698.5	7046.0	0.144
Right Hip	288.4	418.0	1115.1	2079.1	2554.7	0.000
Left Hip	329.6	419.1	1275.9	2347.3	3049.2	0.000
					Score	54.261

Figure 6-38: DVH and statistics resulting from conformal treatment plan for P-1.

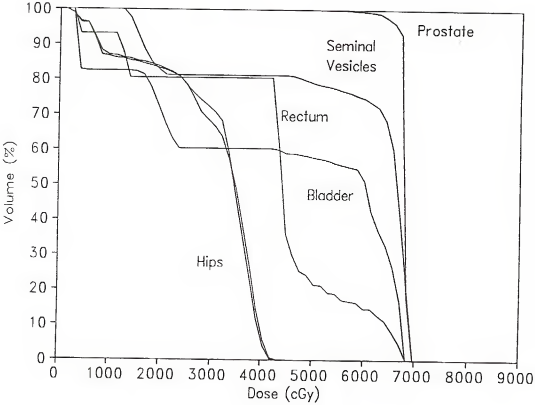

	Min	D_95	Mean	D_5	Max	NTCP/TCP
Prostate	5442.8	6610.1	6721.8	6938.6	6978.0	68.642
Seminal Vesicles	1256.0	1482.0	5597.9	6838.0	6838.4	33.489
Bladder	279.1	319.5	4258.1	6698.9	6698.9	0.040
Rectum	279.1	380.3	4067.7	6685.8	6838.4	1.746
Right Hip	139.6	604.9	2967.2	4027.6	4186.8	0.000
Left Hip	139.6	597.6	2953.6	4061.8	4186.8	0.000
					Score	22.577

Figure 6-39: DVH and statistics resulting from conventional plan for P-2.

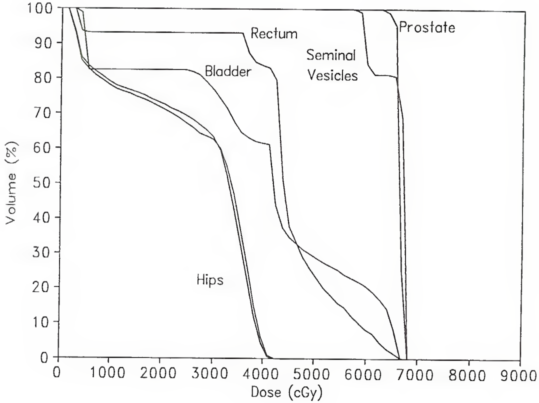

	Min	D_95	Mean	D_5	Max	NTCP/TCP
Prostate	6267.0	6539.9	6566.1	6785.6	6812.0	68.672
Seminal Vesicles	5722.1	5895.6	6507.0	6675.8	6675.8	78.066
Bladder	272.5	488.4	3868.3	6538.5	6539.5	0.000
Rectum	272.5	378.9	4313.9	6213.4	6675.8	0.879
Right Hip	136.2	242.7	2598.6	3941.6	4087.2	0.000
Left Hip	136.2	237.9	2590.2	3980.3	4087.2	0.000
					Score	53.138

Figure 6-40: DVH and statistics resulting from BEV plan for P-2.

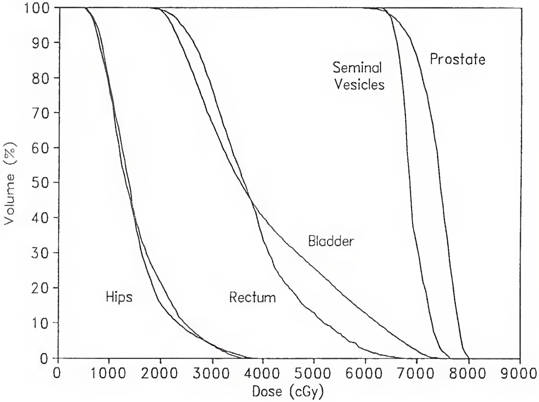

	Min	D_95	Mean	D_5	Max	NTCP/TCP
Prostate	5640.0	6673.7	7352.9	7852.8	8000.0	69.231
Seminal Vesicles	6280.0	6511.7	6878.9	7380.8	7600.0	78.257
Bladder	1840.0	2192.7	3923.0	6701.1	7400.0	0.004
Rectum	1720.0	2372.2	3716.1	5665.4	6720.0	0.294
Right Hip	480.0	731.0	1492.5	2846.8	3640.0	0.000
Left Hip	480.0	694.7	1429.9	2840.9	3840.0	0.000
					Score	54.019

Figure 6-41: DVH and statistics resulting from conformal plan for P-2.

the prescription isodose is fairly consistent between the stereotactic and conformal plans, and the primary difference between the plans is found in the low dose regions. It is interesting to note, however, that even with the higher average brain dose within the Peacock plans, NTCP calculations were fairly consistent between the conventional and conformal plans. This indicates that, while the spread of the low dose lines is not aesthetically pleasing, current models of tissue tolerance consider them relatively insignificant and the probability of complication is driven almost entirely by the hot spots within normal tissue. Still, these low doses throughout the brain do result in a small increase in NTCP and corresponding decrease in overall score. The failure of inverse radiotherapy planning to deliver superior plans coupled with its decreased efficiency, as is displayed in Table 6-10, make intensity modulated treatments using the Peacock system ineffective for small intracranial targets.

Table 6-10: Delivery Efficiency ($MU_{SRS}/MU_{conformal}$) for patients SRS-1 through SRS-6. Note that on average approximately 2/3 of the beam is wasted in the modulation process (Average efficiency = 0.33).

Patient	MU_{SRS}	$MU_{conformal}$	Efficiency
SRS-1	2684	6921	.39
SRS-2	2586	7466	.35
SRS-3	3284	10357	.32
SRS-4	4295	12192	.35
SRS-5	2948	11289	.26
SRS-6	2765	8659	.32

This is not necessarily the case when one investigates conventional external beam radiotherapy as is illustrated in Figure 6-43. Head and neck plans devised using conformal planning are significantly better than those planned using conventional techniques, although part of this advantage is due to the fact that Peacock utilizes all of the CT data. When the head and neck cases were replanned using the BEV display, target dose is seen to increase while normal tissue dose decreases. Conformal head and neck plans still offer a significant advantage over BEV head and neck plans since they conformally avoid critical structures and lower the normal tissue toxicity while still delivering a therapeutic tumor dose.

Prostate cases planned conformally are slightly better than conventional treatment plans, since they can be made to better spare the bladder and rectum. When BEV planning is used to conformally shape the fields, however, the advantage gained by using intensity modulated fields is clinically insignificant. Since the critical structures are conformally avoided using intensity modulated fields, dose escalation to the prostate can be considered in order to increase the probability of cure without increasing the probability of normal tissue complications. To test this, P-1's prescription dose was escalated to the point where normal tissue toxicity for the conformal plan was comparable to that in the conventional plan (7600 cGy). This dose escalation slightly increased the overall probability of uncomplicated control to 54.4%. It is clear that critical structures, particularly the rectum, must be better avoided in order to consider clinically significant dose escalation.

Lung cases may benefit from conformal treatments since intensity modulated beams can better conform to the shape of the target and thus spare the lung, spinal cord and other critical structures. In order to successfully shrink the margins around lung tumors and maintain tumor coverage, however, a dose algorithm which more correctly models the dose distribution would be required. Again, dose escalation to lung tumors would be possible with a hopeful increase in TCP without the corresponding increase in NTCP.

Although inverse radiotherapy planning is suitable for all of the aforementioned sites, it is currently unacceptable for breast planning due to the dose inhomogeneity within the breast. Target dose inhomogeneity is a concern when using this treatment planning system, and is apparently a function of target size. To test this hypothesis, plans were generated using P-1's external contour with a spherical target in the center. As the diameter of the sphere was varied from 1 to 6 cm the resultant minimum dose to the target dropped as a percentage of maximum. Figure 6-44 shows this decrease as a function of spherical target volume. This increased target inhomogeneity as a function of volume is especially undesirable since breast lesions, which are susceptible to damage from hot spots, are the largest lesions examined in this study. This inhomogeneity could be decreased through use of a two dimensional modulator or, alternatively through software modifications which constrain the allowable target dose inhomogeneity. After such modification, it is theoretically possible to increase the dose homogeneity while sparing normal tissue.

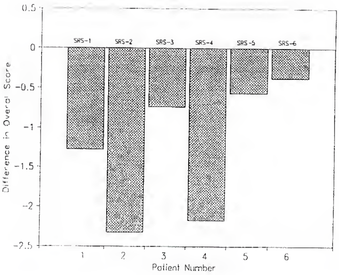

Figure 6-42: Difference in probability of uncomplicated control (Peacock conformal five table angle plan - conventional stereotactic plan) for patients SRS-1 through SRS-6.

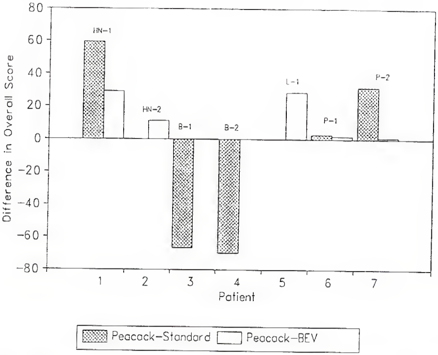

Figure 6-43: Difference in probability of uncomplicated control for conventional radiotherapy patients.

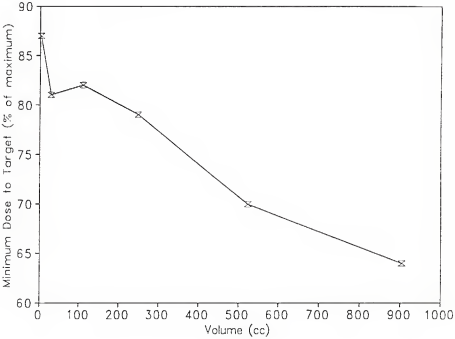

Figure 6-44: Illustration of Peacock's decrease in prescription isodose line as a function of lesion volume.

CHAPTER 7
PHYSICAL REQUIREMENTS FOR INTENSITY MODULATION DEVICE

Computer Simulation of Intensity Modulator

A clinically useful approach to inverse radiotherapy planning requires a mathematical solution to the problem in conjunction with a method for physically implementing the intensity modulation as prescribed by this mathematical solution. Unfortunately, mathematical solutions found in the literature either ignore the physical limitations of a modulation device and simply assume a continuously variable intensity modulator, or they model a specific device with all of its inherent limitations. In order to study the effects of these limitations, dynamic compensation above a slit collimator was investigated. This dynamic compensation may be achieved through the use of a temporally modulated multileaf collimator system.

Alternatively, intensity modulation of the beam may be achieved via a multivane step wedge device. Each of the vanes is capable of independent translation, which allows variation of the amount of attenuating material in the path of the radiation beam. By independently varying the amount of attenuation in the beam at each vane position, the beam can be spatially modulated in order to produce a beam profile which closely approximates a generic mathematically determined intensity modulation function. Although this approach differs conceptually from temporal modulation, it suffers from exactly the same physical limitations and this discussion is ultimately applicable.

The primary advantage of "all or nothing" temporal modulation over spatial modulation is that dosimetry calculations need not consider hardening of the radiation beam. With the step wedge case, however, the differential attenuation in the primary beam can increase the effective energy of the radiation beam by preferentially filtering lower energy components of the beam spectrum. Discounting beam hardening effects, however, dosimetry for the two situations should be similar.

Derivation of Semiempirical Dose Model

For the purpose of modeling the effect of the multivane system on the radiation beam, a simplified dose model was devised. The area underneath the compensator was broken into dose bins, and a mathematical separation of the primary and scattered components of the beam was performed in much the same manner as is done in the Cunningham scatter integration method of dose computation [Cun72]. Since the primary and scattered components of the radiation beam obey different boundary conditions, it is useful to compute their dose computations separately and then sum them at the end of the computation. Thus, the dose to the central axis bin at the depth d_{max} is given by

$$D = TMR \cdot [P + \sum_{i=1}^{n} k_i \cdot S_i \cdot w_i + \sum_{j=1}^{m} k_j \cdot S_j \cdot w_j]$$

where

D = total dose
TMR = tissue-maximum ratio
P = primary dose
k_i = transmission factor for bin i (dependent on the amount of attenuation above bin i)
S_i = scatter function for bin i (dependent on distance of bin i from calculational point)
w_i = off axis factor (dependent on distance of bin i from central axis).

The use of the two subscripts i and j is necessary to account for differences in the two-dimensional intensity modulation function on either side of the central axis. Clearly, for an arbitrary i equal to j the scatter function and off axis functions should be equal if we assume that the radiation beam is symmetric. The transmission factors, however, may vary significantly since the independent translation of the vanes can allow for large differences in attenuation or modulation time above two dose bins on opposite sides of the central axis although their indices are equivalent.

The primary component of the dose was determined by considering the dose dependence on the cross sectional area of the beam. In the limit as the cross sectional area of the radiation beam approaches zero, the scattering volume also approaches zero. If the volume available for beam scattering is reduced to zero, only the primary component of the dose remains. Several obstacles make it practically impossible to measure the dose from a beam of zero cross sectional area: the finite size of measuring instruments, penumbral effects and scatter from beam limiting devices. In order to determine this dose value, one must collect measured data for numerous small field sizes and then extrapolate the function back to zero area field size.

Beam data measurements were performed using a 6 MV x-ray beam produced by a Philips SL75-5 linear accelerator at the Shands Cancer Center. To measure the small field data an ISORAD diode (designed and manufactured by Theta Systems, Inc.) was utilized which has 7.1 mm physical diameter and therefore causes minimal perturbation of the radiation beam. The diode used has inherent buildup equivalent to approximately 1.6 cm of solid water, so the data were measured at approximately d_{max} for the 6 MV beam. Basic beam data measurements obtained with the diode were checked against an ion chamber and the diode was seen to track the ion chamber to within 1%. Since penumbral effects were seen when the beam was limited to within 0.5 cm of the diode, the minimum field size measured was limited to 0.8 cm^2. These small field sizes were obtained using a divergent lead collimator which defined a 1x20 cm slit at isocenter. The field sizes were limited further by placing lead attenuators atop the slit collimator to trim the field edges.

Table 7-1: Summary of Measurement Equipment

Instrument	Manufacturer	Model Number	Serial Number	Active Volume
Ion Chamber (Markus)	PTW	N23343-295	A131	0.6 cm^3
Electrometer	Keithley	35614	38186	NA
Diode	Nuclear Associates	202200	X233	0.25 mm^3

After obtaining data points for numerous small field sizes, the zero area primary component of the beam was determined via extrapolation using higher order polynomial curve fitting (see Fig. 7-1). Although the value for the primary and scatter components of the dose obtained in such a manner will not be exact, the requirement for accuracy in these values is "relaxed somewhat by the expectation that they will be used for computing purposes only and that the computations involve a reassembly of the components" [Cun72, pg. 43].

Extrapolation of the dose back to zero area can, however, be guided by a variable, $z=rd/(r+d)$, which has been shown to be proportional to the scatter dose component [Niz93]. Linear extrapolation may thus be used to determine the zero-field or primary dose as follows:

$$D(d) = Pri(d) + N(d) \cdot z$$

where N = constant determined from the linear fit, r = beam radius and d = depth in phantom.

Figure 7-2 demonstrates the linear extrapolation of dose to zero-area as a function of the geometric parameter, z, for the measurement conditions described above. Comparison of the linear extrapolation with higher order curve fitting agrees to within 1% (84.6 vs. 83.8 normalized dose units).

Profile computation at points other than the central axis may be performed simply by incorporating the off-axis ratios into the bracketed portion of the computation above. This calculation of the profile for every bin along the linear accelerator axis creates the one-dimensional intensity modulation function (IMF) at a depth of d max.

Once the IMF at the depth of maximum dose has been attained, this profile may be multiplied by the tissue-maximum ratio to obtain the dose at any depth in phantom. Since this simple model cannot handle the effect of beam hardening, it will provide more accurate results for temporally modulated beams. Further, its intended use is for simulation of the dose profile at d_{max} only and not for dose calculation for actual patient treatment, so this simple dose model is sufficient.

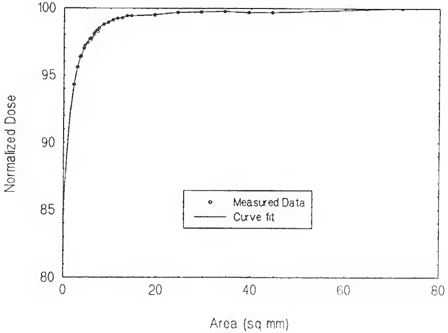

Figure 7-1: Extrapolation of dose to zero area field size using polynomial curve fitting.

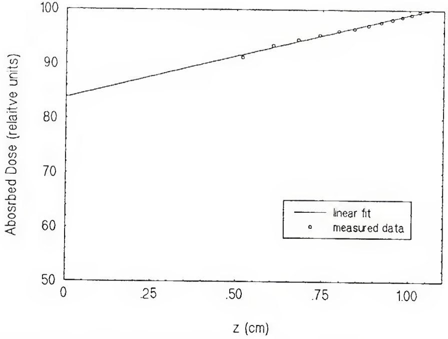

Figure 7-2: Linear extrapolation of dose to zero area field size.

Description of Computer Algorithm

Two design parameters effect the ability of the MIM to sufficiently match the profile designated by a prescribed IMF: vane width and attenuation resolution. In order to investigate these factors, a computer model was generated that utilizes the dose model previously described in conjunction with two common multidimensional optimization algorithms: simulated annealing and Nelder and Mead's downhill simplex method. Upon input of a desired intensity modulation function, the model determines the optimized transmission values required above each dose bin for various intensity modulator configurations. The transmission values were optimized to the center of each vane utilizing a least squares objective function which minimized the difference between the prescribed IMF and the calculated IMF, and IMF calculation was then performed on a 1 mm spaced grid in order to equate the sampling frequencies for the various MIM configurations. In order to ensure physically realistic results, the optimization was constrained to allow beam transmission values between 0.6 and 100%. Transmission values less than 0.6% require inordinate thicknesses of attenuating material which cannot physically be placed between the treatment head of the machine and the patient. Values greater than 100% would require negative thicknesses of attenuating material, which is unphysical. Therefore, whenever the optimization steps outside of the physically realistic range of transmission values, the value is forced to match the nearest reasonable value. As seen in the previous literature review, this is a common obstacle when determining the optimum IMF utilizing inverse radiotherapy planning. The code listing and explanation are contained in Appendix A.

Vane Width

As a mathematically abstract example of this optimization process, Figure 7-3 graphically displays the results obtained for the optimized fit to a periodic function $IMF_{pre} = 100 \mid \sin(0.5x) \mid$ using various vane widths. In all of the figures, the prescribed IMF is represented by a dashed line, with the superimposed solid line representing the computed physical IMF. In order to concentrate only on the effect of vane width, all other design parameters were considered invariant. A periodic function was chosen because the large dose gradient required across the entire radiation field causes difficulty in matching the function with a physical IMF. A second abstract example is an arbitrary profile of one hypothetical treatment slice as demonstrated in Figure 7-4. Such a profile may be required if the targeted region were in close proximity to a critical structure.

The third IMF chosen for optimization purposes is a bit more realistic. Wedges are commonly utilized to achieve dose gradients across the face of the beam in radiation therapy. Figure 7-5 shows the dose gradient produced in the central axis slice by a 60 degree wedge along with the optimized match to this gradient produced by an MIM utilizing different vane widths. The prescribed IMF was obtained from a scan performed at a depth of d_{max} during the annual calibration on a 6 MV Linac at Shands Cancer Center.

Figure 7-6 demonstrates the MIM's ability to fit these various two-dimensional IMFs as a function of vane width by graphing the average objective function (normalized to unity) for these three examples. Clearly, the solution to this problem is analogous to the execution of numerical integration via the trapezoidal rule; the best fit to the desired curve will be obtained through use of the maximum possible number of vanes. In general, however, one discovers a tradeoff exists between computational accuracy and computation time required when utilizing trapezoidal rule integration. The analogous scenario exists for optimization of intensity modulation functions using a multivane device. The number of function evaluations required for convergence of the optimization routine is approximately [Nel65]

$$N_{eval} = 3.2 \cdot (N_{vanes} + 1)^{2.1} \quad .$$

In addition to the increased computational time required for multidimensional optimization, it is important to recall that this is a conceptual model of a device which will ultimately be required to adhere to physical constraints. The most obvious constraint is the machinability of the material used to construct the step wedge vanes. High density materials that would be utilized for dynamic compensation of a high energy x-ray beam can not easily be machined into extremely thin strips. The machinability of such materials constrains us to physical vane widths greater than 3 mm. Discounting the ability to construct very thin vanes, independently controlling and driving each vane are essential elements to useful operation of an MIM. Clearly, thinner vanes require more driving devices and lead to a more complex MIM. Keeping these physical constraints in mind after viewing Figures 7-3 through 7-6, using a vane width of 5 mm is possibly a physically realistic solution and is in the approximate center of the diminishing return floor of the objective function for the chosen examples.

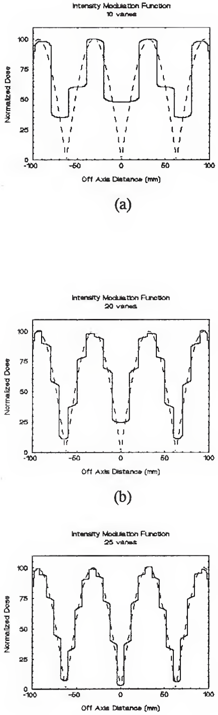

(a)

(b)

(c)

Figure 7-3: Optimal fit to periodic IMF using (a) 10 vanes; (b) 20 vanes; (c) 25 vanes;

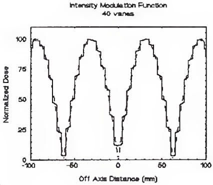

(d)

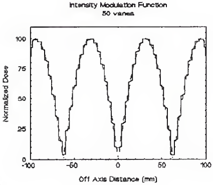

(e)

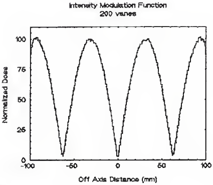

(f)

Figure 7-3--continued: (d) 40 vanes; (e) 50 vanes; (f) 200 vanes.

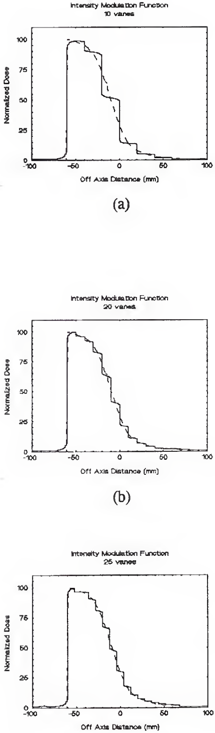

(a)

(b)

(c)

Figure 7-4: Optimal fit to arbitrary IMF using (a) 10 vanes; (b) 20 vanes; (c) 25 vanes;

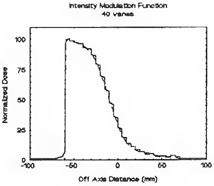

(d)

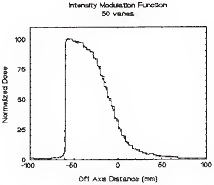

(e)

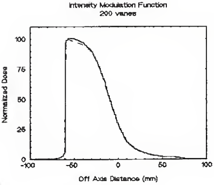

(f)

Figure 7-4--continued: (d) 40 vanes; (e) 50 vanes; (f) 200 vanes.

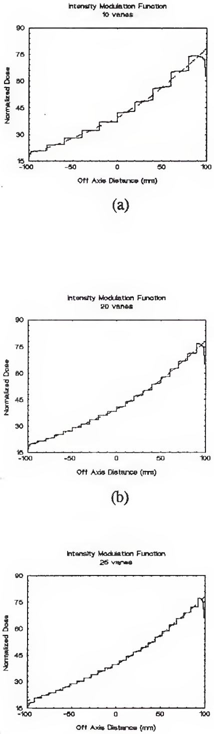

(a)

(b)

(c)

Figure 7-5: Optimal fit to wedge profile using (a) 10 vanes; (b) 20 vanes; (c) 25 vanes;

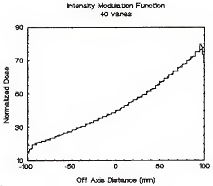

(d)

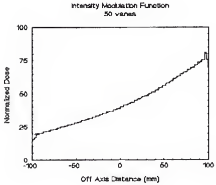

(e)

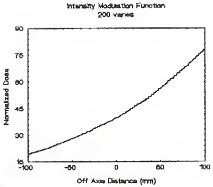

(f)

Figure 7-5--continued: (d) 40 vanes; (e) 50 vanes; (f) 200 vanes.

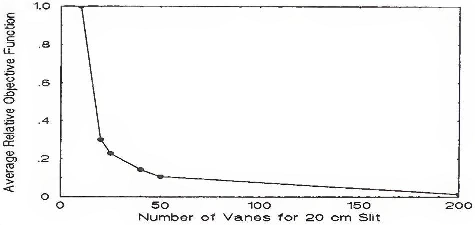

Figure 7-6: Ability of slit MIM to match prescribed IMF as a function of vane width.

Step Resolution

The previous examples which dealt with vane width allowed each vane to assume any thickness of attenuating material which allowed transmission values between 0.6 and 100%. Clearly, a physical MIM which modulates either spatially or temporally must be constrained to allow a finite number of discrete intensity values. With a narrow beam, or so-called good geometry, attenuation of the primary beam, I/I_0 varies with thickness of material as a simple exponential function, $I/I_0 = e^{-ut}$. Although scattered radiation prevents the slit collimator from presenting a narrow beam geometry, Figure 7-7 shows that the attenuation in lead placed above the collimator may be closely approximated by an exponential function.

Since attenuation is an exponential function, it is not prudent to force the compensating steps to be equal thicknesses. Instead, a better approach is to construct the vanes such that the steps allow transmission of the beam in equal percentage increments.

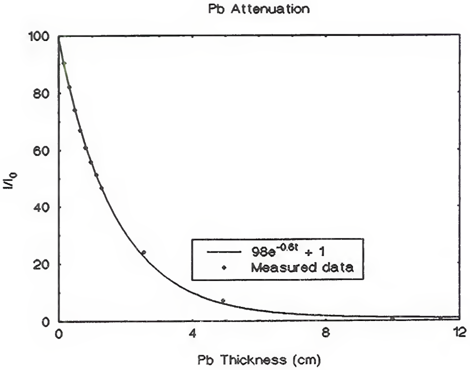

Figure 7-7: Attenuation of 6 MV beam through lead using geometry determined by a slit collimator.

As a simple example, consider a lead vane which consists of five steps. If the vane is not in the path of the beam, it obviously allows 100% transmission. The minimum allowed transmission, which corresponds to placing the maximum allowed vane thickness in the x-ray beam, is 0.6%. There are four more allowable transmission values which correspond to the remaining four steps, and they are chosen to be 20%, 40%, 60% and 80%. Likewise, temporal modulation devices should modulate in equal percentages of beam transmission.

Figures 7-8 through 7-10 depict the best possible match to the previous three examples using representative numbers of steps on each vane of the MIM. In order to eliminate the effect of vane width, all optimization were performed assuming 40 vanes (0.5 cm/vane). Figure 7-11 depicts the effect of step size on the ability to properly match a prescribed IMF. As expected, a large number of steps on each vane allows for a better match to the prescribed IMF. Once again, however, the accuracy with which one matches a prescribed IMF must be balanced with the physical constraints placed on the MIM. This is not quite as critical with step resolution as it is with vane width, and the figure clearly demonstrates that any more than 20 steps per vane is superfluous, and 12 to 15 steps per vane should be sufficient to match the examples shown.

The physical size of the MIM is the only important factor which effects the number of steps placed on each vane for spatial modulation of the beam using step wedge compensators. Since the MIM will eventually be attached to the gantry of the treatment machine, it is important that the size of the MIM is no larger than the maximum allowed for attachment to the treatment machine. The maximum allowed distributed load for the gantry of the Philips SL75-5 is 15 kg for gantry angles other than 0° or 180°. Since the mass of the MIM increases directly with the number of compensating steps and these vanes are composed of a high density attenuating material, the number of allowable intensities must be restricted.

With the use of temporal modulation size requirements do not increase with increases in the number of steps, but one must be concerned with switching speed requirements. The minimum switching time, which is defined as the time required to

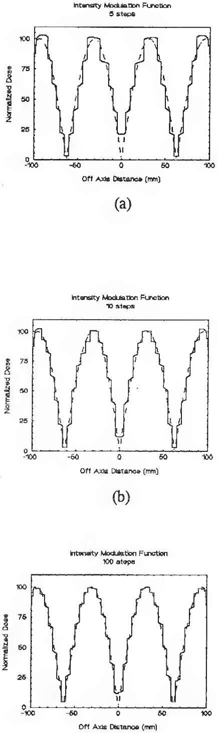

(a)

(b)

(c)

Figure 7-8: Optimal fit to periodic IMF using 40 vanes and (a) 5, (b) 10 and (c) 100 attenuation steps.

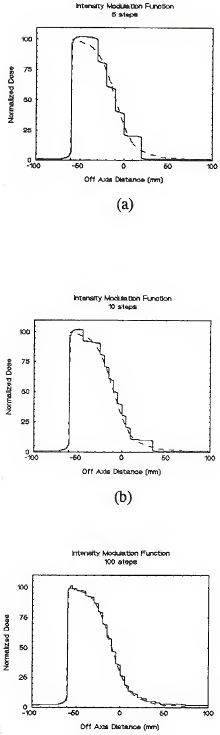

(a)

(b)

(c)

Figure 7-9: Optimal fit to arbitrary profile using 40 vanes and (a) 5, (b) 10 and (c) 100 attenuation steps.

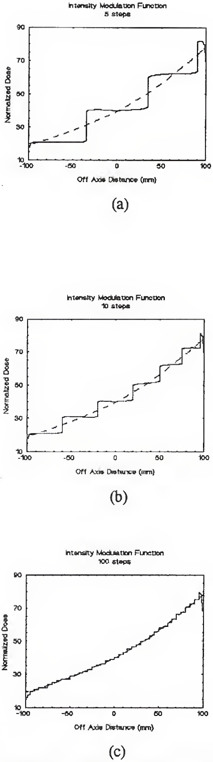

Figure 7-10: Optimal fit to wedge profile using 40 vanes and (a) 5, (b) 10 and (c) 100 attenuation steps.

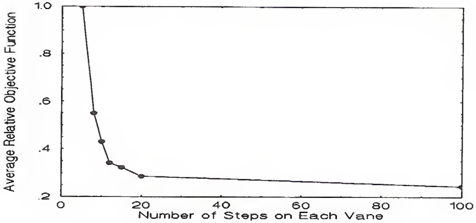

Figure 7-11: Ability of MIM (0.5cm/vane) to match a prescribed IMF as a function of step resolution.

open a vane and immediately close it, determines the number of allowable beam intensities [Mac93]. If we assume rotational delivery may be approximated by a number of discrete beams, Mackie's paper provides the time per discrete beam, t_{beam}

$$t_{beam} = \frac{T \cdot z \cdot SAD}{L \cdot B \cdot SCD}$$

and the optimal switching time,

$$t_{opt} = 3 \cdot \sqrt{\frac{2z}{a}}$$

where T = total beam on time
z = physical vane width (at collimator)
SAD = source to isocenter distance
SCD = source to collimator distance
L = longitudinal vane dimension
B = number of discrete beams in the arc and
a = acceleration of the vane.

From these equations it follows that we may determine the maximum number of allowable intensities, $n_{\max}$ as

$$n_{\max} = \frac{t_{beam}}{t_{opt}} = \frac{T\cdot\sqrt{za}}{3\cdot L\cdot B}\cdot\frac{SAD}{SCD} \qquad .$$

Obviously, whether the intensity is modulated temporally or spatially there exists a physical limit on the allowable number of intensities. The preceding analysis demonstrated little benefit in using more than 10 steps per vane, which is physically realizable.

Clinical Resolution Requirements

As seen previously, the ultimate test of conformal algorithms comes when they are used to create clinical conformal radiotherapy plans. The results of the optimal fit to an ideal IMF give us a feel for the physical requirements of the intensity modulator, but they tell nothing about how well an ideal IMF must be matched in order to provide a clinically viable treatment. In order to determine the spatial resolution required for an intensity modulator that is used clinically, the cases presented in chapter 6 were replanned modelling a modulator with vanes that project a width of 5 mm at isocenter rather than the 10 mm wide MIMIC vanes. Results of these plans are presented in Figures 7-12 through 7-26. Comparison of these figures and tables with the data presented in chapter 6 shows that although 5 mm vanes may allow for a more conformal fit of the dose distribution with the target volume, the primary advantage is due to their ability to achieve a steeper dose gradient than do their 10 mm counterparts. Comparison of these conformal plans with the stereotactic plans, however, shows that the dose gradient achieved using stereotactic planning is still superior to the conformal techniques.

Since the conformation of the high isodose lines to the target is similar with the two techniques, there is very little variation in the overall scores between techniques. Figure 7-27 demonstrates that although the use of 5 mm vanes for conformal planning provides better results than the use of 10 mm vanes, conventional stereotactic treatment planning results were still better for 2/3 of the patients. Since construction of vanes smaller than 5 mm (projected at isocenter) is physically unrealistic, intensity modulation is ill advised for small intracranial targets.

Extension to large fields shows that although there is an improved dose gradient over those planned using 10 mm vane widths, there is no significantly better target conformation or normal tissue sparing. This was expected for large field therapy, since these treatments generally do not require the dramatic dose gradient needed for stereotactic radiosurgery. Figure 7-28 compiles the overall results for these plans compared to the plans seen in chapter 6.

This comparison may be flawed, however, due to inherent weaknesses in the treatment planning system. As was explained earlier, the success of simulated annealing is directly dependent upon the choice of annealing schedule and the appropriate schedule is problem dependent. Halving the vane width without halving the collimator length, as was done for this analysis, doubles the number of variables within the optimization routine. In order to alleviate the expected difficulty, the maximum number of iterations allowed for optimization was squared. This remedy seems sufficient for many plans, but for others the problem may be changed sufficiently that the routine will not converge on the global optimum without a change in annealing schedule. HN-2 and P-2 are examples of plans which never converged to an optimal result. Others, including small intracranial targets such as SRS-4, are also in question since there exists no logical way in which planning that models 10 mm vanes can better a plan using 5 mm vanes, assuming both reach a global optimum. Since the 5 mm vanes are simply 10 mm vanes sliced in half, the worst case scenario would result in equivalent plans using the separate configurations. In all other scenarios the increased modulation provided by increased resolution would provide better results. Regardless, it is not expected that vane resolution should be a limiting factor for larger lesions, but the obvious failure of the optimization algorithm is of concern.

Also of concern is the failure of the system to provide a homogeneous target dose, as was discussed in Chapter 6. Using higher resolution vanes, the target dose inhomogeneity is worse. It is not clear if this is due to the optimization routine's failure to reach a global optimum, or if the inhomogeneity is increased since the lesions are now larger relative to the vane width and slice thickness (refer to Figure 6-44).

Due to these current weaknesses, it is not recommended that one vary the resolution requirements within the Peacock system. Based on the results of the previous computer simulation and the results of other studies [Mos92, Har94], it is suspected that intensity modulated treatments utilizing 5 mm wide vanes would benefit stereotactic treatments. Thus, it would be interesting to revisit this resolution study for small intracranial targets using a different algorithm, such as the approach proposed by Harmon [Har94].

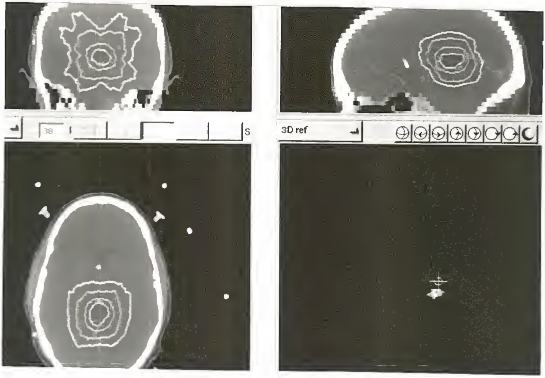

(a)

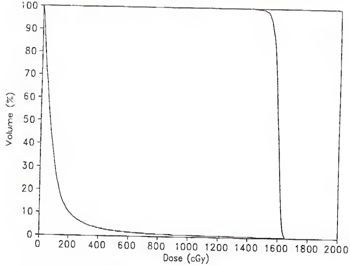

	Min	D_95	Mean	D_5	Max	NTCP/TCP
AVM	1359.9	1539.4	1585.5	1629.5	1648.4	80.9
Brain	0.0	9.6	96.1	305.4	1631.9	1.5
					Score	79.7

(b)

Figure 7-12: Results of conformal plan using 5 mm vanes for SRS-1. (a) 15, 7.5, 3 and 1.5 Gy isodose lines are displayed on orthogonal planes and (b) DVH and statistics.

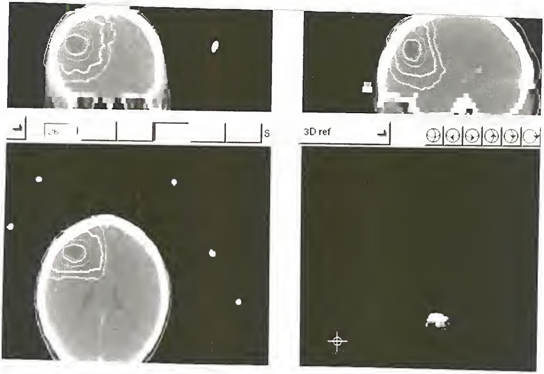

(a)

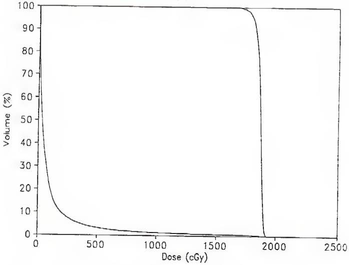

	Min	D_95	Mean	D_5	Max	NTCP/TCP
Target	1625.0	1799.2	1856.7	1900.5	1923.1	77.2
Brain	0.0	2.6	83.6	341.3	1894.2	2.5
					Score	75.3

(b)

Figure 7-13: Results of conformal plan using 5 mm vanes for SRS-2. (a) 17.5, 8.75, 3.5 and 1.75 Gy dose lines are displayed on orthogonal planes and (b) DVH and statistics.

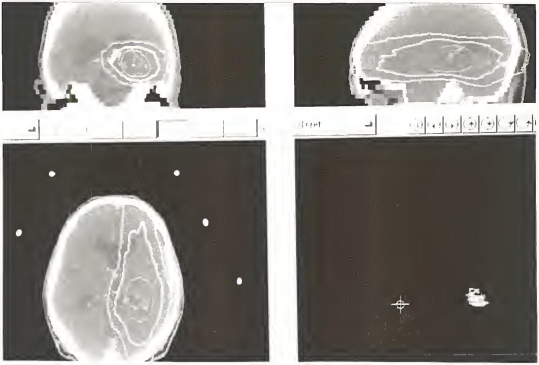

(a)

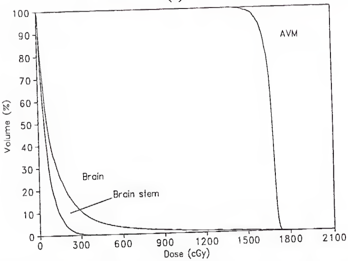

	Min	D_95	Mean	D_5	Max	NTCP/TCP
AVM	1360.5	1360.5	1664.9	1717.6	1744.2	81.2
Brain	0.0	6.3	125.1	452.0	1718.0	2.6
Brain Stem	0.0	9.8	58.3	184.8	409.9	0.0
					Score	79.1

(b)

Figure 7-14: Results of conformal plan using 5 mm vanes for SRS-3. (a) 15, 7.5, 3 and 1.5 Gy dose lines are displayed on orthogonal planes and (b) DVH and statistics.

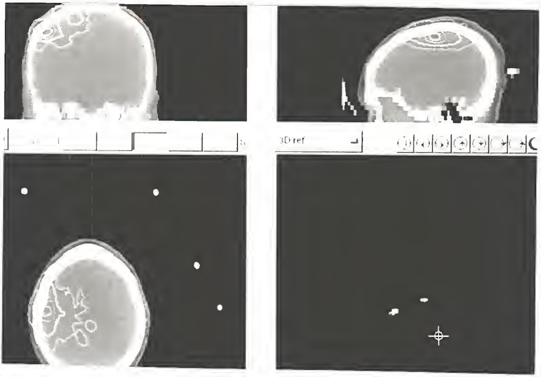

(a)

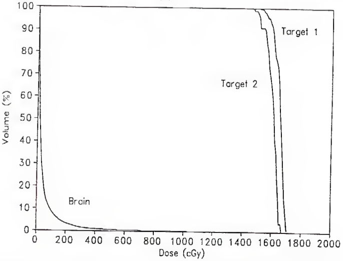

	Min	D_95	Mean	D_5	Max	NTCP/TCP
Target 1	1508.5	1577.0	1646.0	1698.2	1704.5	81.0
Target 2	1465.9	1510.5	1598.0	1652.5	1661.9	80.4
Brain	0.0	1.6	38.0	153.4	1704.5	0.9
					Score	64.5

(b)

Figure 7-15: Results of conformal plan using 5 mm vanes for SRS-4. (a) 15, 7.5, 3 and 1.5 Gy dose lines are displayed on orthogonal planes (through isocenter 1) and (b) DVH and statistics.

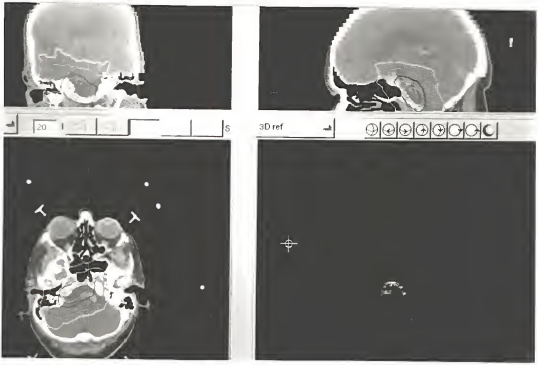

(a)

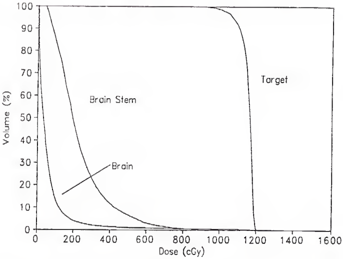

	Min	D_95	Mean	D_5	Max	NTCP/TCP
Tumor	873.5	1060.2	1147.7	1190.0	1204.8	94.0
Brain	0.0	3.0	53.1	174.7	1198.8	0.7
Brain Stem	36.1	63.1	226.8	542.2	994.0	0.8
					Score	92.6

(b)

Figure 7-16: Results of conformal plan using 5 mm vanes for SRS-5. (a) 10, 5, 2 and 1 Gy isodose lines are displayed on orthogonal planes and (b) DVH and statistics.

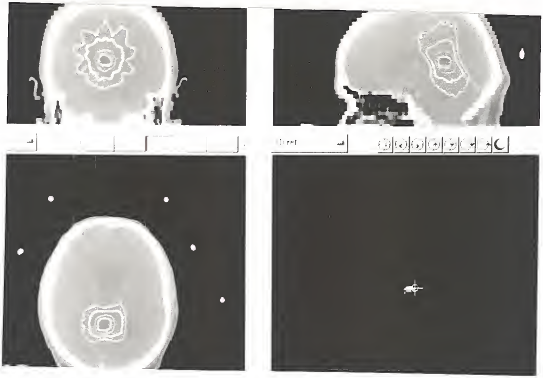

(a)

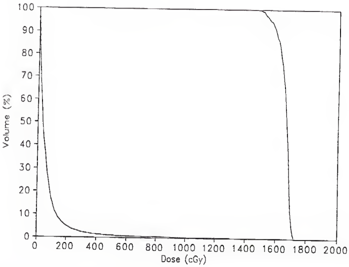

	Min	D_95	Mean	D_5	Max	NTCP/TCP
AVM	1431.0	1557.4	1653.3	1706.7	1724.1	81.2
Brain	0.0	2.4	57.6	196.9	1706.9	1.1
					Score	80.3

(b)

Figure 7-17: Results of conformal plan using 5 mm vanes for SRS-6. (a) 15, 7.5, 3 and 1.5 Gy isodose lines are displayed on orthogonal planes and (b) DVH and statistics.

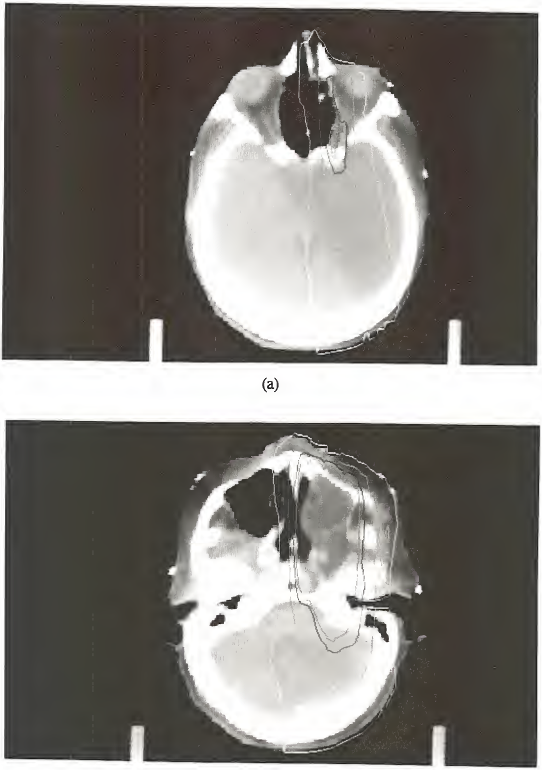

(a)

(b)

Figure 7-18: 5 mm vane conformal plan for HN-1. 74.8, 65, 55, 45 and 20 Gy isodose lines are displayed on a) a slice 3 cm superior to the central axis and b) the central axis.

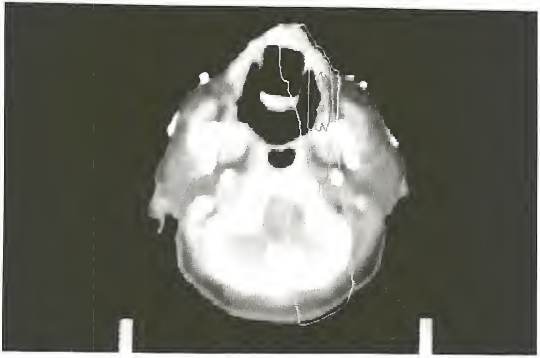

(c)

Figure 7-18--continued: (c) 3 cm inferior to central axis slice.

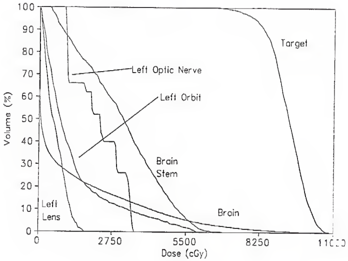

	Min	0_95	Mean	0_5	Max	NTCP/TCP
Tumor	6016.5	8040.9	9263.9	10338.7	10840.6	61.211
Brain	0.0	5.8	1080.2	5624.4	10461.2	0.198
Brain Stem	379.4	636.1	3061.5	5627.6	6775.4	0.015
Left Orbit	0.0	94.5	1243.3	4612.7	508.1	0.027
Left Optic Nerve	975.7	998.2	2172.5	3496.1	3523.2	0.000
Left Lens	0.0	79.6	589.0	1374.0	1680.3	0.329
					Score	60.863

Figure 7-19: 5 mm vane conformal plan dose volume histogram and statistics for HN-1.

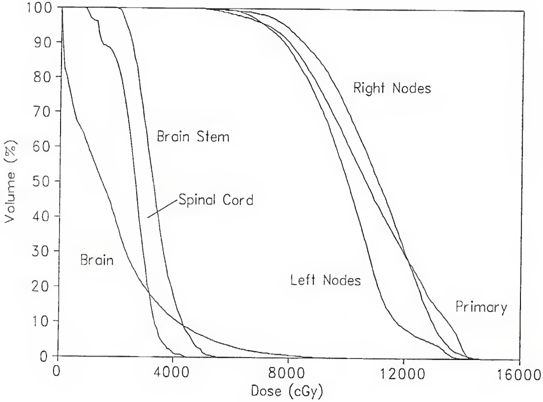

	Min	D_95	Mean	D_5	Max	NTCP/TCP
Primary	4375.0	7212.9	10612.0	13893.7	14364.6	55.587
Right Nodes	4739.6	7799.3	10857.2	13367.1	14583.3	69.223
Left Nodes	4229.2	7124.5	9869.9	12778.4	14145.8	75.840
Brain	0.0	35.2	1759.0	5318.4	9989.6	0.139
Brain Stem	1895.8	2261.6	3275.1	4648.8	5468.8	0.000
Spinal Cord	802.1	1265.4	2516.4	3543.8	4375.0	0.020
					Score	29.136

Figure 7-20: 5 mm vane conformal treatment plan DVH and statistics for HN-2.

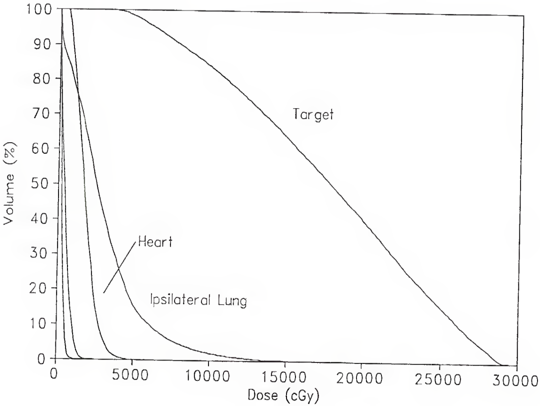

	Min	D_95	Mean	D_5	Max	NTCP/TCP
Target	3382.4	6234.5	17439.9	27523.4	29411.8	95.528
Ipsilateral Lung	0.0	92.1	2914.3	7785.4	19117.7	100.000
Heart	441.8	754.0	1705.6	3102.7	5147.1	0.000
Contralateral Lung	0.0	32.6	412.1	1191.8	2352.9	0.000
Contralateral Breast	0.0	29.5	200.7	624.0	1029.4	0.000
Target (Fibrosis)	3382.4	6234.5	17439.9	27523.4	29411.8	100.000
					Score	0.000

Figure 7-21: DVH and statistics resulting from conformal treatment planning for B-1.

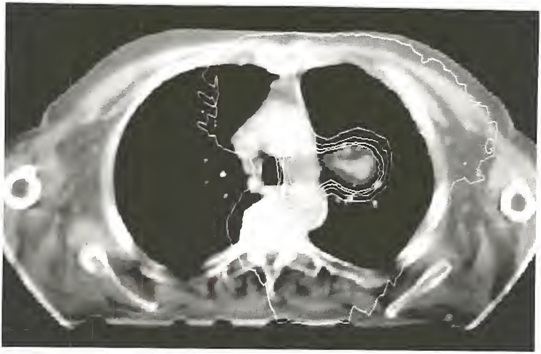

(a)

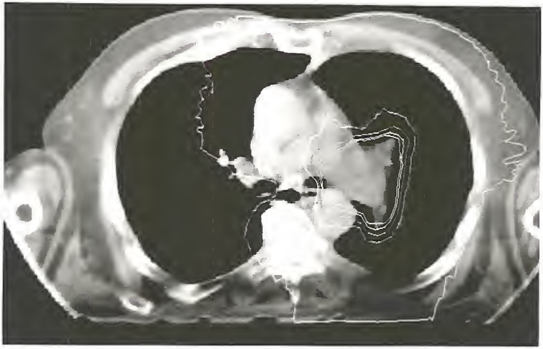

(b)

Figure 7-22: 5 mm vane conformal plan for L-1. 68, 64, 55, 45 and 10 Gy isodose lines are superimposed on the a) axial slice 4 cm superior to the central axis and b) central axis.

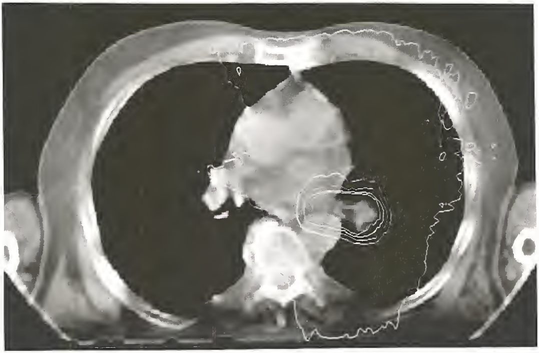

(c)

Figure 7-22--continued: (c) 3 cm inferior to the central axis.

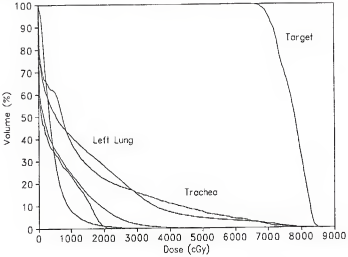

	Min	D_95	Mean	D_5	Max	NTCP/TCP
Target	6290.0	6998.7	7712.9	8312.6	8500.0	31.338
Ipsilateral Lung	0.0	8.6	1264.7	4446.6	8202.5	1.571
Trachea	0.0	10.1	1357.3	577.2	8117.5	0.015
Cantralateral Lung	0.0	77.5	426.7	1234.2	3655.0	0.000
Spinal Cord	0.0	4.8	460.5	1756.4	2125.0	0.000
					Score	30.841

Figure 7-23: DVH and statistics resulting from 5 mm vane conformal plan for L-1.

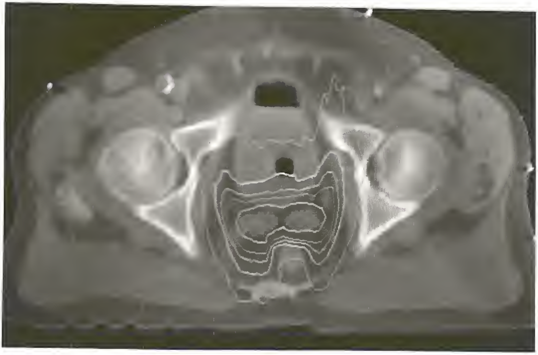

(a)

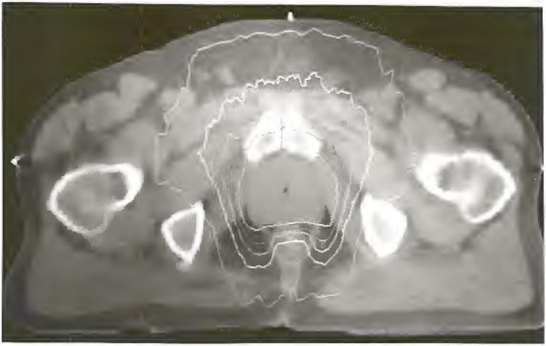

(b)

Figure 7-24: 5 mm vane conformal plan for P-1. 68.4, 55, 45, 35 and 20 Gy dose lines are displayed on the a) axial slice 3 cm superior to the central axis and b) central axis.

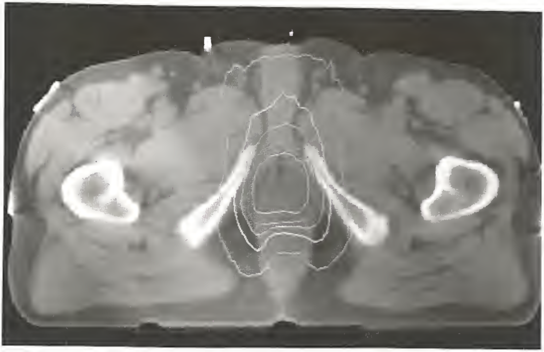

(c)

Figure 7-24--continued: (c) 3 cm inferior to the central axis.

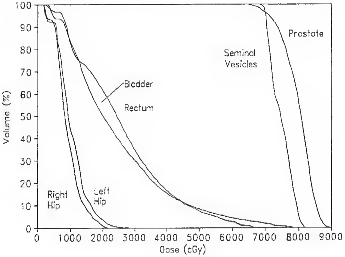

	Min	D_95	Mean	D_5	Max	NTCP/TCP
Prostate	6440.3	7114.0	7966.7	8633.0	8883.1	69.292
Seminal Vesicles	6795.6	7014.8	7440.8	8007.7	8172.5	78.165
Bladder	310.9	466.8	2408.1	5809.6	7906.0	0.000
Rectum	220.8	756.0	2553.6	5490.3	6973.2	0.083
Right Hip	177.7	222.1	880.1	1667.1	2176.4	0.000
Left Hip	177.7	246.9	990.5	1875.0	2798.2	0.000
					Score	54.117

Figure 7-25: DVH and statistics resulting from 5 mm vane conformal plan for P-1.

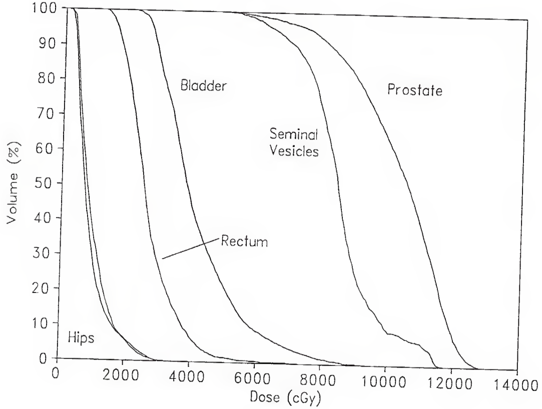

	Min	D_95	Mean	D_5	Max	NTCP/TCP
Prostate	4800.0	7511.2	10253.0	12177.7	12800.0	69.733
Seminal Vesicles	4928.0	6410.1	8456.7	11173.1	11648.0	75.549
Bladder	2176.0	2664.3	4104.8	6818.0	9216.0	0.087
Rectum	1216.0	1602.3	2617.0	4170.0	7232.0	0.046
Right Hip	128.0	320.1	827.9	2103.4	3072.0	0.000
Left Hip	192.0	356.3	910.9	2156.9	3200.0	0.000
					Score	52.659

Figure 7-26: DVH and statistics resulting from 5 mm vane conformal plan for P-2.

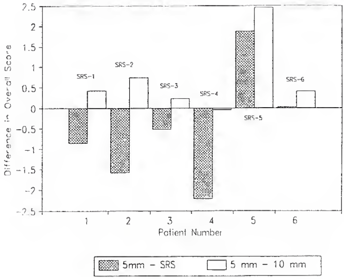

Figure 7-27: Comparison of probability of uncomplicated control for stereotactic planning (SRS), Peacock plans using 10 mm vanes (10 mm) and Peacock plans using 5 mm vanes (5 mm).

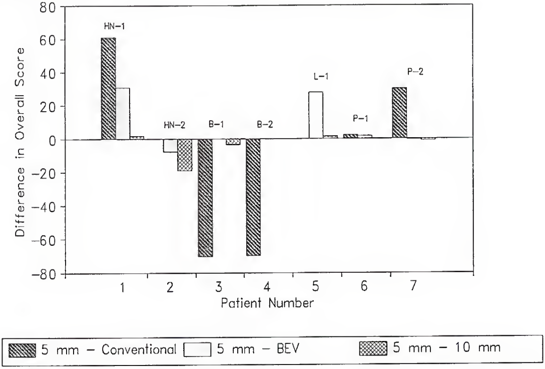

Figure 7-28: Comparison of overall score for conventional, BEV, Peacock 10 mm vane width (10 mm) and Peacock 5 mm vane width (5 mm) plans.

CHAPTER 8
CLINICAL EFFICACY OF TOMOTHERAPY

The term tomotherapy is literally defined as slice therapy, which makes it applicable to the treatment plans presented previously. Strictly speaking, however, tomotherapy is a proposed treatment delivery concept in which a small linear accelerator is mounted on a ring gantry similar to a CT scanner [Mac93]. Like the Peacock system, the beam would be collimated to a slit, and the one-dimensional intensity profile temporally modulated using multiple vanes. Unlike the Peacock system, however, the ring gantry of a tomotherapy unit would most likely not allow treatment delivery using noncoplanar beams. Treatments would instead be delivered in a full 360^0 arc at a zero degree table angle (full axial slice treatment).

Noncoplanar beams are regularly utilized in treatments such as SRS since the intersection of multiple noncoplanar beams at the isocenter enhances the dose gradient outside of the targeted region. It has been hypothesized that noncoplanar beams may provide little dosimetric advantage when intensity modulated beams are utilized, since the fields are shaped to deliver optimal dose levels both inside and outside the target [Mac93, Har94]. The merit of this hypothesis will be tested using the clinical cases and evaluation criteria presented previously.

Tomotherapy plans for the clinical examples presented previously are depicted in Figures 8-1 through 8-14. Comparison of these plans with those presented previously shows clearly that the dose gradient in the axial plane is much worse when one abandons the use of noncoplanar beams. Conformity of the high isodose lines with the target remains similar, however, and TCP remains consistent regardless of the differences in treatment plans. Due to the decreased dose gradient, however, a larger volume of normal tissue is irradiated which generally leads to a small increase in NTCP and corresponding decrease in overall score for the plan. Figure 8-15 demonstrates that noncoplanar beams are essential for the treatment of small intracranial lesions. The probability of uncomplicated control is decreased (relative to 5 table angle plans) for all patients except 2: SRS-3 and SRS-5. SRS-3 does not provide a representative comparison, however, since its 5 table angle plan utilized long arcs which resulted in a poor dose gradient. SRS-5 is also questionable since there is a substantial increase in dose to eyes and optic nerves. These increased doses did not result in a decrease in overall score, but are still of concern.

Considering figure 8-16, it is reasonable to conclude that noncoplanar beams offer little advantage over tomotherapy for large field external beam radiotherapy treatments since the decreased dose gradient is of little consequence for these situations. The lone exception is HN-1, which inexplicably never adequately conformed to the target. Overall, however, it appears that tomotherapy offers a significant advantage, however, over conventional treatments for both head and neck therapy and lung treatments. They offer little advantage over conventional radiotherapy for prostate carcinoma, and are again not recommended for treatment of the intact breast or intracranial lesions which are currently treated using stereotaxis.

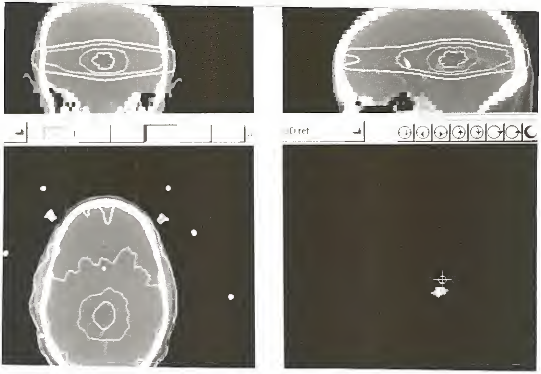

(a)

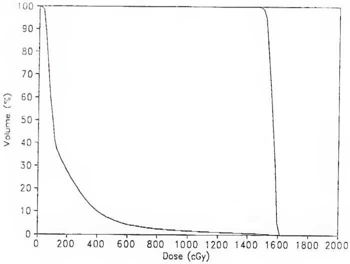

	Min	D_95	Mean	D_5	Max	NTCP/TCP
AVM	1475.8	1524.2	1563.8	1605.0	1612.9	80.8
Brain	0.0	30.9	167.7	551.7	1604.8	2.5
					Score	78.8

(b)

Figure 8-1: Results of tomotherapy plan for SRS-1. (a) 15, 7.5, 3 and 1.5 Gy isodose lines are displayed on orthogonal planes and (b) DVH and statistics.

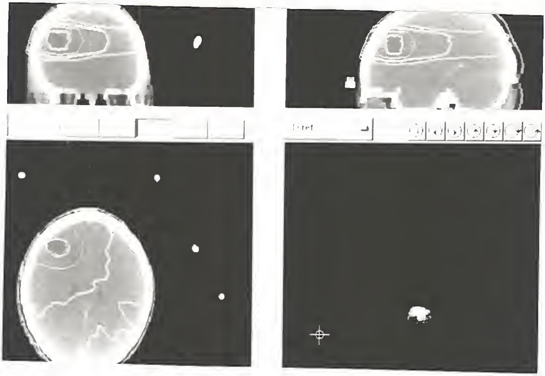

(a)

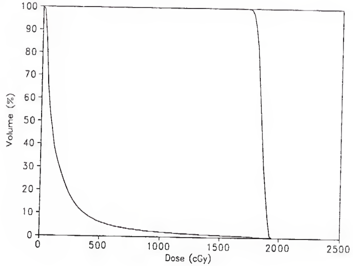

	Min	D_95	Mean	D_5	Max	NTCP/TCP
Target	1682.7	1768.7	1830.5	1900.7	1923.1	77.0
Brain	0.0	20.6	151.4	548.0	1884.6	3.6
					Score	74.2

(b)

Figure 8-2: Results of tomotherapy plan for SRS-2. (a) 17.5, 8.75, 3.5 and 1.75 Gy dose lines are displayed on orthogonal planes and (b) DVH and statistics.

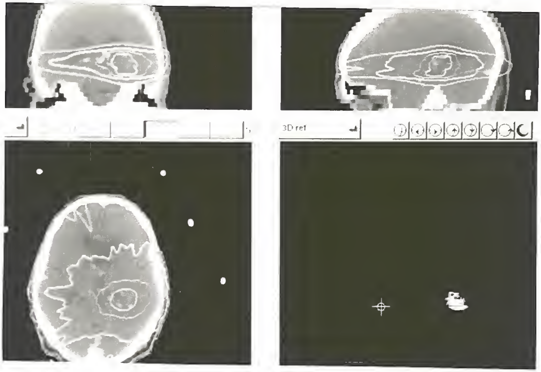

(a)

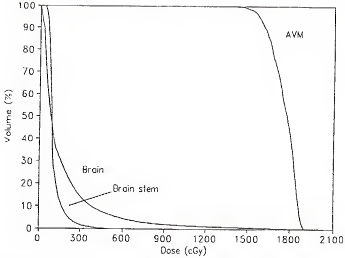

	Min	D_95	Mean	D_5	Max	NTCP/TCP
AVM	1348.1	1576.5	1750.9	1870.5	1898.7	81.6
Brain	0.0	13.6	152.9	550.6	1889.2	3.2
Brain Stem	38.0	56.0	98.9	211.2	607.6	0.0
					Score	79.0

(b)

Figure 8-3: Results of tomotherapy plan for SRS-3. (a) 15, 7.5, 3 and 1.5 Gy dose lines are displayed on orthogonal planes and (b) DVH and statistics.

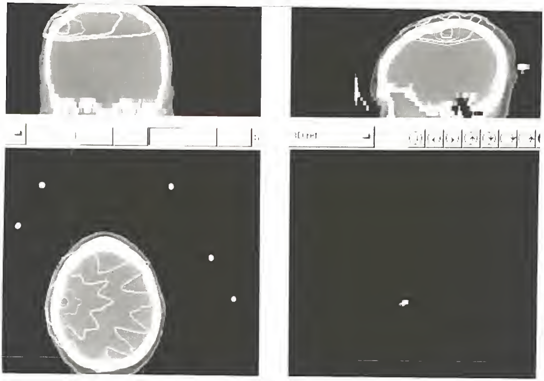

(a)

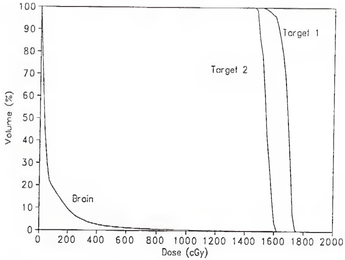

	Min	D_95	Mean	D_5	Max	NTCP/TCP
Target 1	1554.2	1639.2	1712.0	1767.1	1780.1	81.7
Target 2	1491.0	1515.7	1570.5	1633.8	1644.6	80.0
Brain	0.0	1.7	63.3	288.6	1807.2	1.5
					Score	64.4

(b)

Figure 8-4: Results of tomotherapy plan for SRS-4. (a) 15, 7.5, 3 and 1.5 Gy dose lines are displayed on orthogonal planes (through isocenter 1) and (b) DVH and statistics.

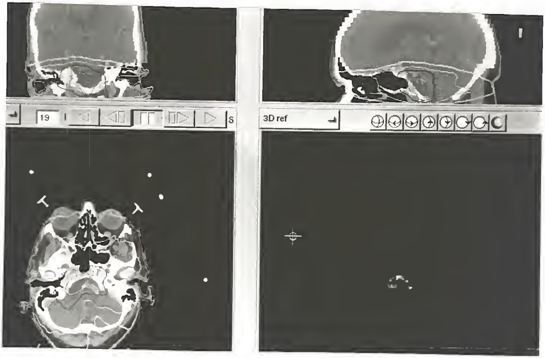

(a)

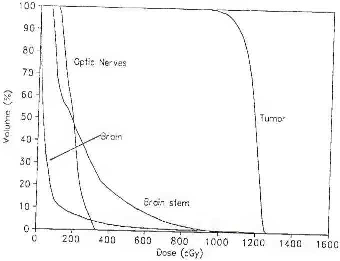

	Min	D_95	Mean	D_5	Max	NTCP/TCP
Tumor	856.3	1051.9	1166.8	1235.0	1250.0	94.3
Brain	0.0	1.1	53.8	256.0	1231.3	0.8
Brain Stem	56.3	63.2	239.6	683.6	1093.8	3.2
					Score	90.6

(b)

Figure 8-5: Results of tomotherapy plan for SRS-5. (a) 10, 5, 2 and 1 Gy isodose lines are displayed on orthogonal planes and (b) DVH and statistics.

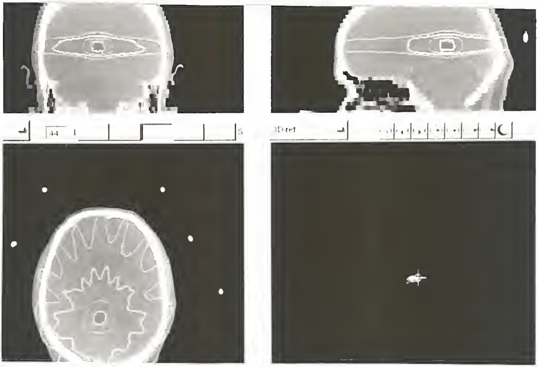

(a)

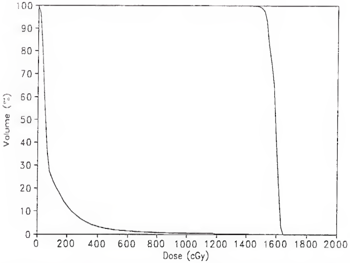

	Min	D_95	Mean	D_5	Max	NTCP/TCP
AVM	1425.8	1533.1	1590.5	1637.1	1648.4	80.9
Brain	0.0	13.4	87.5	327.3	1648.4	1.4
					Score	79.8

(b)

Figure 8-6: Results of tomotherapy plan for SRS-6. (a) 15, 7.5, 3 and 1.5 Gy isodose lines are displayed on orthogonal planes and (b) DVH and statistics.

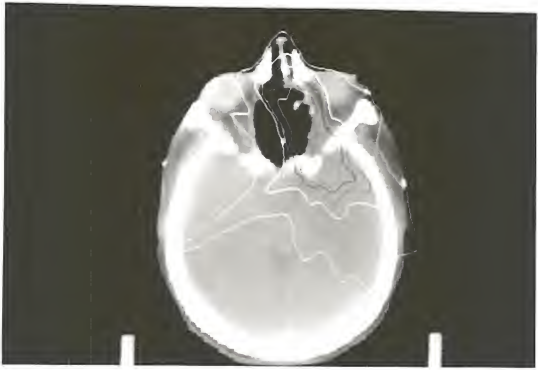

(a)

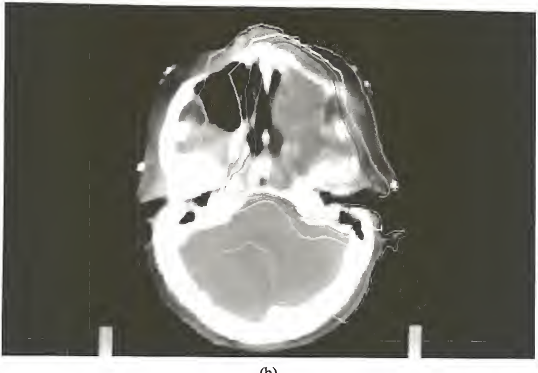

(b)

Figure 8-7: Tomotherapy plan for HN-1. 74.8, 65, 55, 45 and 20 Gy isodose lines are displayed on a) a slice 3 cm superior to the central axis and b) the central axis.

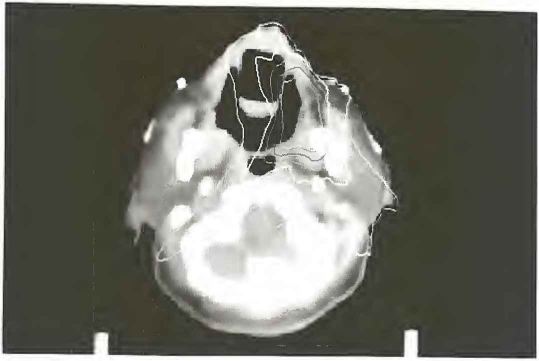

(c)

Figure 8-7--continued: (c) 3 cm inferior to central axis slice.

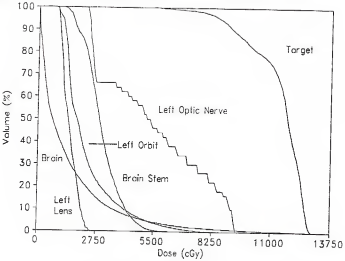

	Min	D_95	Mean	D_5	Max	NTCP/TCP
Tumor	5287.6	8574.2	11331.0	12682.1	12896.6	64.698
Brain	0.0	29.9	1342.7	4962.1	12574.1	0.519
Brain Stem	1225.2	1626.4	2943.7	4584.4	6125.9	0.000
Left Orbit	838.3	1136.7	2227.6	5081.2	8060.3	0.188
Left Optic Nerve	2256.9	2369.7	5385.6	9301.6	9350.0	62.092
Left Lens	838.3	974.6	1459.9	2193.5	2450.3	3.728
					Score	23.445

Figure 8-8: Tomotherapy plan dose volume histogram and statistics for HN-1.

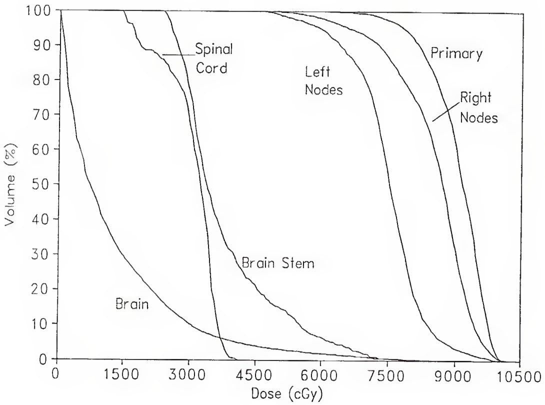

	Min	D_95	Mean	D_5	Max	NTCP/TCP
Primary	5502.9	7817.1	9024.9	9853.8	10131.4	92.142
Right Nodes	4782.9	6528.9	8470.2	9650.9	10182.9	67.991
Left Nodes	4474.3	5932.7	7450.8	8794.3	10080.0	75.474
Brain	0.0	59.6	1221.9	4062.9	9360.0	0.016
Brain Stem	1440.0	1679.5	3025.0	3740.6	4062.9	0.268
Spinal Card	514.3	641.3	1147.8	2076.1	2520.0	0.018
					Scare	47.141

Figure 8-9: Tomotherapy treatment plan DVH and statistics for HN-2.

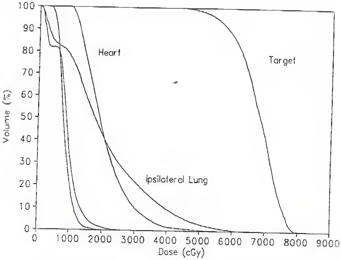

	Min	D_95	Mean	D_5	Max	NTCP/TCP
Target	4079.0	5293.0	6950.0	8307.0	8772.0	94.632
Ipsilateral Lung	0.0	54.0	565.0	1860.0	3904.0	48.242
Heart	88.0	159.3	331.0	879.7	1842.0	0.000
Contralateral Lung	0.0	39.0	152.0	395.0	1140.0	0.000
Contralateral Breast	44.0	104.7	226.0	515.3	921.0	0.000
Target (Fibrosis)	4079.0	5293.0	6950.0	8307.0	8772.0	96.993
					Score	1.473

Figure 8-10: DVH and statistics resulting from conformal treatment planning for B-1.

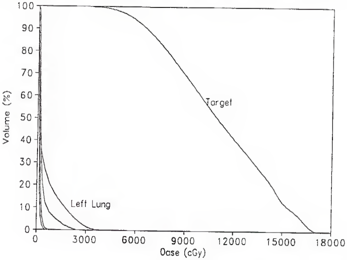

	Min	D_95	Mean	D_5	Max	NTCP/TCP
Target	2069.0	5732.0	10990.7	16226.3	17241.4	94.008
Ipsilateral Lung	0.0	18.1	469.5	2364.5	3793.1	0.000
Heart	0.0	92.9	278.9	1166.3	2586.2	0.000
Contralateral Lung	0.0	11.1	75.1	271.6	517.2	0.000
Contralateral Breast	0.0	15.8	113.2	366.3	689.7	0.000
Target (Fibrosis)	2069.0	5732.0	10990.7	16226.3	17241.4	100.000
					Score	0.000

Figure 8-11: Tomotherapy plan DVH and statistics for B-2.

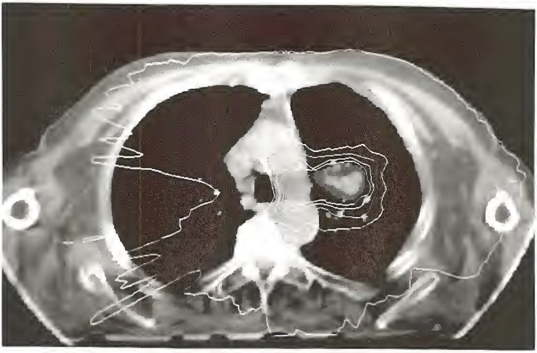

(a)

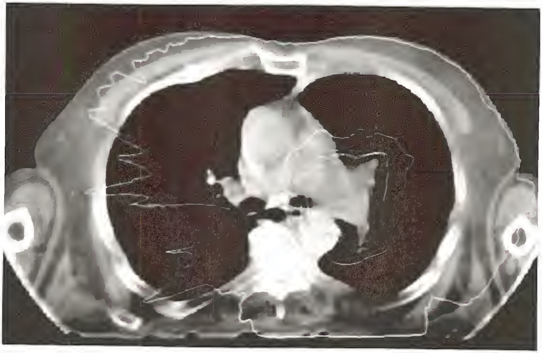

(b)

Figure 8-12: Tomotherapy plan for L-1. 68, 64, 55, 45 and 10 Gy isodose lines are superimposed on the a) axial slice 4 cm superior to the central axis and b) central axis.

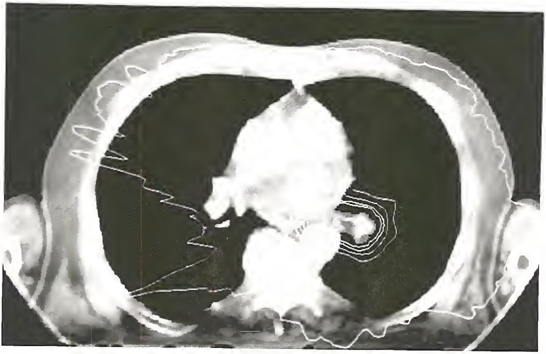

(c)

Figure 8-12--continued: (c) 3 cm inferior to the central axis.

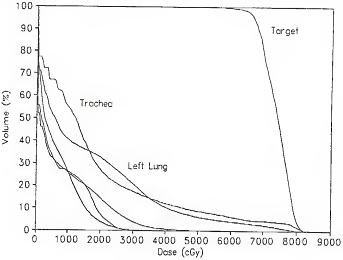

	Min	D_95	Mean	0_5	Max	NTCP/TCP
Target	5797.1	7087.9	7779.8	8410.3	8607.6	32.319
Ipsilateral Lung	0.0	7.8	1427.8	5110.1	8220.3	4.365
Trachea	0.0	9.4	1653.6	6420.2	8263.3	0.077
Contralateral Lung	0.0	8.6	559.9	1872.7	3486.1	0.000
Spinal Cord	0.0	4.5	544.1	2133.9	2754.4	0.000
					Score	30.885

Figure 8-13: DVH and statistics resulting from tomotherapy plan for L-1.

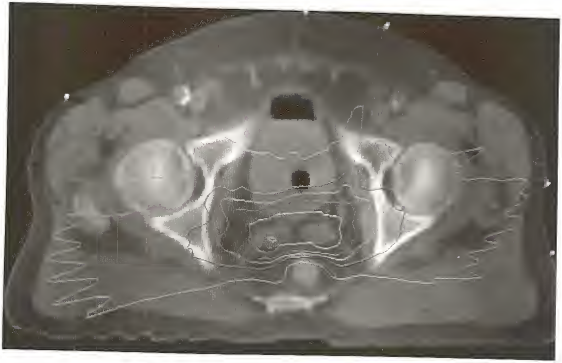

(a)

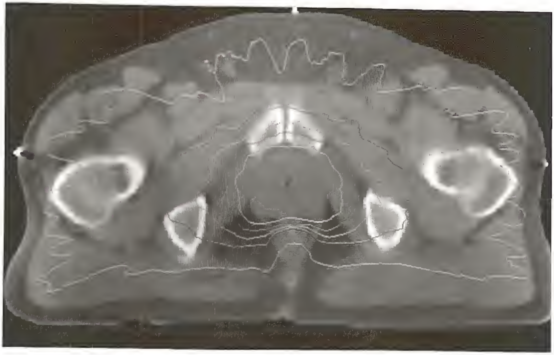

(b)

Figure 8-14: Tomotherapy plan for P-1. 68.4, 55, 45, 35 and 20 Gy dose lines are displayed on the a) axial slice 3 cm superior to the central axis and b) central axis.

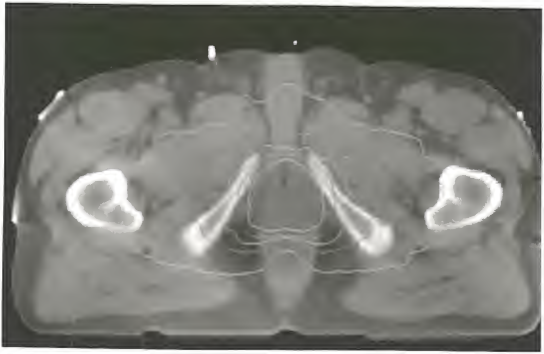

Figure 8-14--continued: (c) 3 cm inferior to the central axis.

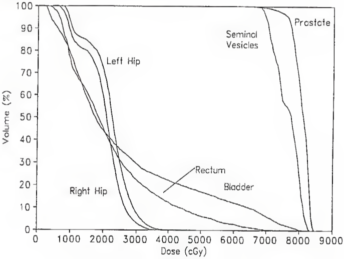

	Min	D_95	Mean	0_5	Max	NTCP/TCP
Prostate	6164.4	7631.5	8034.6	8368.4	8444.4	69.419
Seminal Vesicles	6797.8	6960.3	7603.9	8177.9	8275.6	78.274
Bladder	211.1	378.8	2562.6	7146.1	8022.2	0.000
Rectum	295.6	644.5	2151.8	5338.8	7600.0	2.958
Right Hip	591.1	843.5	1956.4	2872.2	3631.1	0.000
Left Hip	717.8	927.2	2157.2	3129.4	3926.7	0.000
					Score	52.730

Figure 8-15: DVH and statistics resulting from tomotherapy plan for P-1.

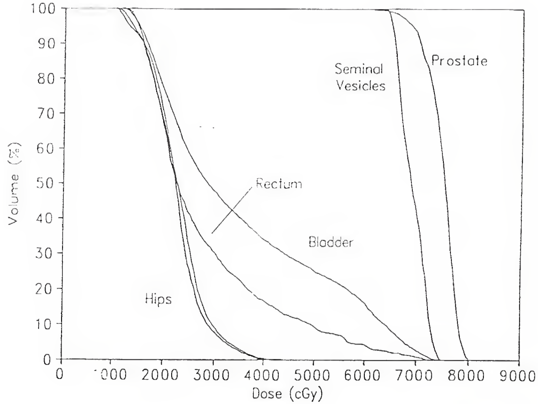

	Min	0_95	Mean	0_5	Max	NTCP/TCP
Prostate	6000.0	6881.2	7438.5	7862.5	8000.0	69.489
Seminal Vesicles	6280.0	6487.9	6873.8	7326.4	7440.0	78.242
Bladder	1120.0	1509.8	3499.3	6767.3	7440.0	0.000
Rectum	1160.0	1486.6	2748.3	5687.7	7240.0	0.608
Right Hip	1000.0	1300.8	2217.5	3216.8	4080.0	0.000
Left Hip	1040.0	1376.0	2251.0	3286.0	4360.0	0.000
					Score	54.039

Figure 8-16: DVH and statistics resulting from tomotherapy plan for P-2.

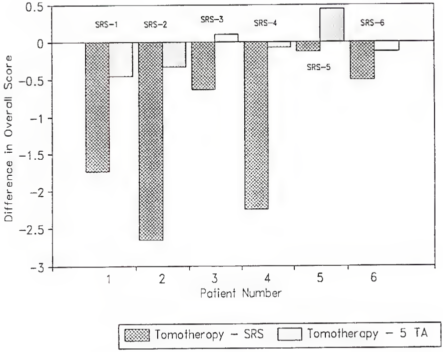

Figure 8-17: Comparison of probability of uncomplicated control for conventional stereotactic, tomotherapy and noncoplanar (five table angles) conformal planning.

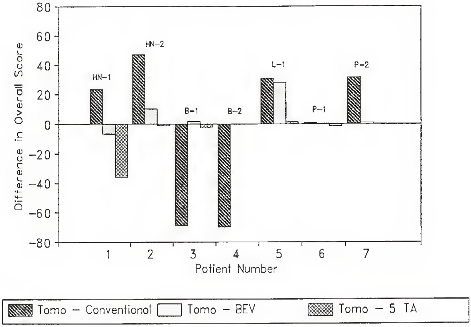

Figure 8-18: Comparison of probability of uncomplicated control for conventional, BEV, tomotherapy and noncoplanar (five table angles) conformal planning.

CHAPTER 9
THE EFFECT OF RANDOM POSITIONAL ERRORS ON INVERSE RADIOTHERAPY PLANS

Typically, radiotherapy treatments are designed with a large margin around the target volume to account for errors in patient positioning, motion and possibility of microscopic disease around the tumor. Although the size of this margin depends on characteristics of the lesion and experience of the physician designing the treatment, 1 cm margins are typically included around the target volume. Through retrospective analyses of portal films, the overall inaccuracy in radiotherapy delivery can be better determined and methods for determining the appropriate margin are developing. Using such analysis, it has been suggested that a margin of approximately $1.5\sigma_{tot}$ (where σ_{tot} is the standard deviation of the total uncertainty in treatment delivery) is required to ensure adequate tumor coverage [Goi86].

While including this margin helps avoid underdosage of the tumor periphery, it also increases the absorbed dose received by surrounding normal tissues. The primary goal of conformal therapy is to reduce this margin in order to reduce toxicity to normal structures while maintaining a curative tumor dose. As these margins are constricted to more closely match the target volume, it is imperative to ensure accurate dose delivery with as little uncertainty as possible. In recent years, radiotherapy has experienced a dramatic increase in accuracy of dose delivery; CT allows improved delineation of target and critical structures, linear accelerators are more precisely aligned, improved patient immobilization devices are used which allow better set up reproducibility [Uri91] and dosimetric calculational methods are much improved.

None of these errors can be completely controlled, however, and they result in an overall uncertainty in dose delivery. For example, the target and normal tissues as delineated on CT slices represent their relative positions averaged over an instant in time and does not account for motion within the body caused by breathing, heart beat, bowel gas, stomach, bladder and intestines [Lin93]. Uncertainty in linear accelerator parameters leads to systematic errors that with adequate quality assurance can routinely be kept within ± 0.8 mm [Leo87], and with great care can be reduced to ± 0.2 mm [Fri89]. Immobilization devices help reproduce patient set up, but even the most rigid devices contain inherent uncertainty; even the rigid frame attached to the skull for stereotactic radiosurgery may experience a small shift throughout the course of a day. Finally, although dose algorithms have improved they still have weaknesses which can cause significant systematic dose perturbations in certain situations. In general, these algorithms are worse in penumbral regions, in high (bone) or low (lung) density tissues and at interfaces between regions of different density [Uri91].

The purpose of this study is to examine the effects of set up uncertainties on treatment plans designed using the Peacock treatment planning system. For this study, it will be assumed that the tumor and internal organs are rigidly fixed, and their positions can be obtained directly from the CT images. To account for the movement of the target and make certain it is not underdosed, a small margin is left around the lesion. The movement of normal tissues is ignored completely, however, and it is reasonable to assume that the CT scans provide a realistic average position for all treatments [Uri91]. It is further assumed that all errors are uncorrelated, which is based on published results of measured uncertainties for pelvic [Hun93a] and head and neck treatments [Hun93b]. One last assumption is that all set up errors are completely random since there should be no systematic errors in aligning the patient with the linear accelerator.

Since stereotactic treatments are delivered in a single fraction with a tight margin around the target, a small uncertainty in the delivered dose can lead to catastrophic results. The results with conventional and conformal treatments are comparable, however, since no margin is added to the target in either case. Further, there is little uncertainty in such treatments due to the excellent immobilization provided by the head ring and the accuracy of the linear accelerator system. Thus, the small uncertainty in radiosurgery treatments is of little consequence.

The analysis is more interesting for large field cases since the patients are not immobilized or positioned as precisely and the positioning must be reproduced for multiple fractions. Fractionated radiotherapy treatments rely on the fact that the patient will be repositioned the same for each of multiple treatments. Unfortunately, a lack of reproducibility in these set ups is a major source of uncertainty in the resultant dose distribution received by the patient. For this analysis, only patient set up errors will be considered, since they are the primary cause of uncertainty for large field fractionated cases. Although systematic errors from mechanical and calculational inaccuracies are present, these will be ignored; assuming good quality assurance techniques mechanical errors are negligible [Leo87], and it is assumed that if inverse radiotherapy planning is used in the clinic more sophisticated dose algorithms can be employed to reduce calculational uncertainty. Thus, the expected dose, D_{exp} delivered to point (AP,LAT,AX) after n fractions is simply

$$D_{exp}(AP,LAT,AX) = \frac{1}{n}\sum_{i}^{n} D_{plan}(AP-ap_i,\ LAT-lat_i,\ AX-ax_i)$$

where D_{plan}(AP,LAT,AX) is the planned dose at point (AP,LAT,AX) and ap_i represents the positional error in the AP direction for the i^{th} fraction [Lin93]. Further assuming that errors are uncorrelated allows consideration of the errors in each dimension separately as the convolution of the dose distribution with the appropriate response functions,

$$D_{exp}(AP,LAT,AX) = \frac{1}{n}\sum_{i}^{n} D_{plan}(AP,LAT,AX)\cdot g_1(AP-ap_i)\cdot g_2(LAT-lat_i)\cdot g_3(AX-ax_i)$$

where g_1(AP-ap) describes the distribution of the translation of D in the anteroposterior direction and equals 1 for AP = ap but zero otherwise. It was assumed that the distributions were gaussian distributed, and the convolution was performed numerically with the distribution extended to $\pm 3\sigma$ (covers 99.75% of all cases). The normal distribution was approximated by a probability grid in which the distribution was divided equally in $\pm 0.1\sigma$ bins and each bin was randomly sampled (using ANSI C pseudorandom generator rand()) to determine the shifts in the AP, lateral and axial directions. Dose distributions and DVHs were calculated for each fraction separately and then averaged to determine an overall DVH. Although this provides an accurate representation of the average daily DVH, it is important to note that this is not a very good representation of the cumulative treatment DVH [Hun93a].

Studies of repositioning errors are found in the literature for both head and neck and pelvic treatments. For head and neck the deviation in patient set up along the patient's coordinate system have been measured using portal imaging to be $\sigma_{AP} = 1.5$ mm, $\sigma_{Lat} = 2.8$ mm and $\sigma_{Ax} = 2.1$ mm [Hun93a]. The margins on the head and neck cases planned previously using Peacock are approximately 4 mm, so are sufficient ($> 1.5\sigma$) assuming that only set up uncertainties are considered. For pelvic treatments, the uncertainties have been determined similarly to be $\sigma_{AP} = 5.3$ mm, $\sigma_{Lat} = 5.5$ mm and $\sigma_{Ax} = 5.3$ mm [Hun93b]. A 1 cm margin is included in conventional prostate plans, which means the target periphery should be within the margin for approximately 95% of the random shifts (1 cm $\approx 2\sigma$). Since the margins in the conformal prostate plans are not sufficient to account for the uncertainty, the effect of positional errors on P-1's tomotherapy distribution was examined. The standard deviations from Hunt's paper were convolved with the planned dose distribution as previously described.

Figures 9-1 through 9-6 show the tomotherapy DVHs for P-1's targets and critical structures with planned and average distributions displayed. Also shown are the minimum and maximum DVHs, which represent extremes in daily DVHs. On average, the minimum dose to the prostate is over 3000 cGy less than was planned, but the mean dose for the average daily treatment remains fairly consistent with the mean dose for the planned distribution (7889.7 vs 8034.6 cGy). The average distribution for the seminal vesicles also closely resembles the planned, with the exception of a lower minimum dose. Since TCP models show a stronger correlation with mean target dose than with minimum target dose, the deviation from the planned distribution should not cause a significant reduction in the probability of tumor control. If, however, systematic errors exist which cause the overall treatment to more closely resemble the minimum histograms, then tumor coverage is significantly compromised. Examining Figure 9-2, for example, it is clear that an axial shift in patient position can lead to a geographic miss of a large portion of the seminal vesicles.

Figures 9-3 through 9-5 demonstrate the effect of random uncertainty on the normal tissue dose distributions. Once again, the average histograms after 38 treatments show clinically insignificant deviation from the planned histograms. Analogous to the target histograms, systematic errors which shift the histograms toward their respective maxima would significantly increase the doses for both rectum (planned distribution average dose = 2151.8 cGy and maximum distribution mean dose = 3683.9 cGy) and bladder (planned distribution mean dose = 2562.6 cGy and maximum distribution mean dose = 3754.7 cGy) and also the probability of complications. The hips are far enough away from the target volume that the envelope created between maximum and minimum is small making the histograms for planned and average distributions nearly identical.

This analysis demonstrates that since a small margin is left around the target volume, random positional errors cause a negligible change in the average distribution over the course of treatment. If, however, systematic errors are introduced into the analysis catastrophic failures can occur. Although systematic errors are generally negligible in comparison to random positional errors, it is important to identify such errors and take the necessary steps to eliminate them. Mechanical accuracy of the linear accelerator is one of the primary causes of systematic errors in patient treatment. Since most conceptual designs of inverse radiotherapy treatments rely on gantry rotation, it is advisable to minimize the errors caused by gantry sag through a design similar to the SRS200 floor stand. Since the SRS200 has a proven mechanical accuracy of 0.2 mm [Fri89], coupling this gimbal bearing system with a modulation device should force mechanical errors to be entirely insignificant.

Improvement in the dosimetry algorithm would remove the other source of significant systematic error within the system. As seen in chapter 4, the algorithm currently chosen for dose computation has inherent errors which can hardly be considered insignificant. More sophisticated dosimetry algorithms, most notably convolution algorithms, are currently available which can reduce the dosimetric uncertainty to within 3-5% [Hol93, Har94].

Assuming that these inaccuracies are eradicated, the margins provided by the Peacock system are sufficient to account for set up uncertainties. With further improvement in patient positioning, if possible, the margins could theoretically be shrunk even further which would allow dose escalation without increase in normal tissue toxicity. If these systematic errors are not removed from the system, larger margins should be included to account for such inaccuracies. Inclusion of these margins would defeat the purpose of conformal treatment planning, however, and reduce its potential benefit.

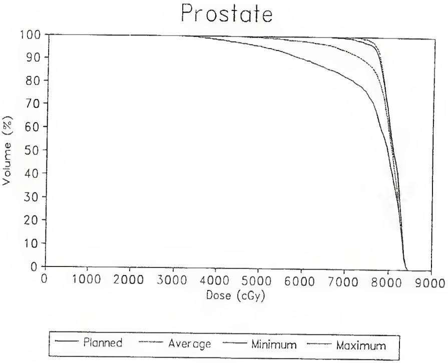

Figure 9-1: Prostate DVH for P-1 tomotherapy plan with random setup uncertainties.

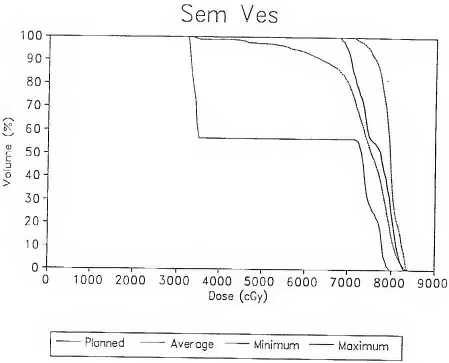

Figure 9-2: Seminal vesicles DVH for P-1 tomotherapy plan with random uncertainties.

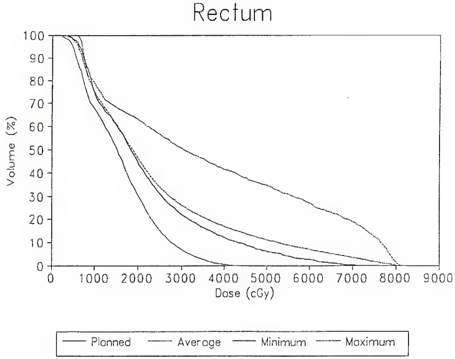

Figure 9-3: Rectum DVH for P-1 tomotherapy plan with random setup uncertainties.

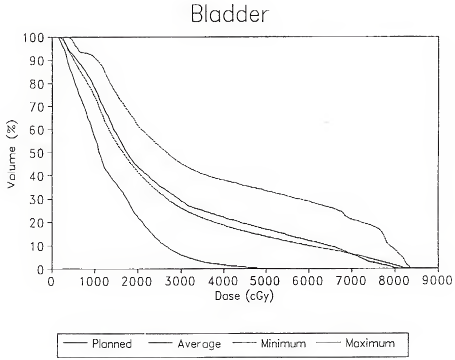

Figure 9-4: Bladder DVH for P-1 tomotherapy plan with random setup uncertainties.

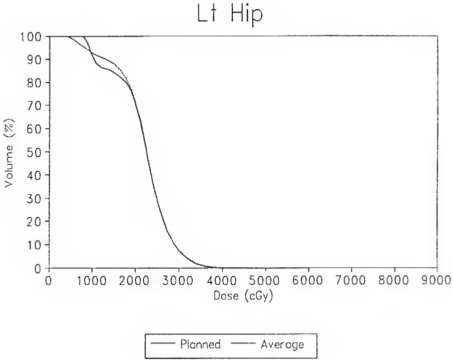

Figure 9-5: Left hip DVH for P-1 tomotherapy plan with random setup uncertainties.

CHAPTER 10
DISCUSSION

The work presented here addressed the clinical efficacy of intensity modulation for 3D conformal radiotherapy. This study was undertaken in order to ascertain the advantages of conformal therapy over conventional techniques, and determine if the benefit reaped justifies the investment required to make intensity modulated treatment a clinically viable option. Pre-release version 1.9R7 of the Peacock Plan^{TM}, which is the most advanced conformal planning system commercially available, was used to perform this research.

Although 3D conformal systems such as Peacock are becoming commercially available, their clinical utility has yet to be established. The current limitations of 3D conformal systems are primarily engineering difficulties which can theoretically be overcome. The solution of these implementation challenges is not the subject of this research effort. Before expending resources necessary to attack such obstacles, it was felt that clinical efficacy needed to be established and a retrospective analysis was in order. Therefore, this work focuses on computer simulation of clinical inverse radiotherapy planning. It is assumed throughout this work that dose distributions provided by all systems are valid. This assumption was considered conservative and does not effect the outcome of the analysis.

In order to determine the possibility of benefit of this mode of therapy, the retrospective analysis was performed for patients with several different disease sites: intracranial, head and neck, breast, lung and prostate. For each patient three types of treatment plans were developed: conventional, three-dimensional and inverse radiotherapy plans. The primary obstacle in determining the efficacy of the treatment modality was developing a method of objectively evaluating each of these treatment plans. Historically, this evaluation has been performed by simply viewing 2D slices through the target volume with isodose lines superimposed. While this was part of the methodology used within this work, more sophisticated evaluation methods were also used to condense the vast amount of information. Dose volume histograms and statistics which quantify the dose volume distribution were calculated for each plan. Biological dose response models were also utilized in order to develop a method of objectively quantifying the effect of a given treatment plan. An algorithm which calculates normal tissue complication probability (NTCP) was developed based on calculational methods found in the literature [Lym85, Kut91]. Since methods found in the literature are based on conventional fractionation schemes and treatment volumes, parameters within the model were optimized in order to better fit published stereotactic radiosurgery data. A separate algorithm was generated to calculate tumor control probability (TCP) using techniques developed by Goitien and Niemierko [Goi83, Nie93]. Since both NTCP and TCP models were developed assuming conventional fractionation (2 Gy/fraction), these models are valid only with such fractionation schemes. Fractionation schedules within this work vary from 1.7 Gy/fraction to 17.5 Gy/fraction, however. To account for this wide variation, input data for both models were modified using the linear quadratic model. Calculated values for NTCP and TCP were then used to determine a single objective score for each plan, which was the probability of uncomplicated control.

Although these tools condense the information contained within the 3D dose distributions, they are still under development and present a weak link in the analysis. There is a paucity of accurate dose volume information in the literature, and as these dose response models are based on this data they reflect this weakness. Further, these models may underestimate the effects of dose inhomogeneity, since virtually no data exist which detail these effects. Newer models under development model the organization of tissues based on their relative seriality and should provide an improved method of accounting for the dose volume response of normal tissues. Currently, these models have been developed for a limited number of normal tissues and do not provide an adequate database for a wide scale study such as this one. Further, the model can only be as good as the biological response data that it models, and one can not expect to more accurately predict NTCP until more accurate data are available. Use of the currently available models in conjunction with the dosimetric statistics and graphical displays, however, has allowed adequate objective comparison within this work.

Using these treatment planning techniques and tools, this work demonstrated that there is no advantage in using intensity modulated fields for treatment of small intracranial lesions treated stereotactically. The small circular collimators used for stereotactic radiosurgery are a powerful tool which can provide a highly conformal fit to all but the most irregular targets. Further, stereotactic radiosurgery provides a steeper dose gradient outside of the targeted region than was attained using intensity modulated beams. Under certain situations, such as a concave target volume near the brain stem, this conformal technique may prove superior. Considering the additional time and complexity required to modulate the beam intensity, however, it does not seem prudent to pursue inverse radiotherapy planning for radiosurgical cases.

For clinical situations which require larger field sizes, head and neck and lung cases show the most benefit from the use of conformal techniques. Head and neck lesions are generally quite irregular and are adjacent to radiosensitive structures such as the brain, brain stem, optic nerves and spinal cord. Similarly, lung lesions are quite irregular and in close proximity to critical structures. Through the use of intensity modulated beams, the entire target can be treated to the prescription dose while sparing nearby critical structures.

While inverse radiotherapy plans for prostate carcinomas are better than those determined using conventional planning techniques, there is little apparent clinical benefit. This is because prostate cases, like stereotactic cases, have small, regularly shaped targets with beam's eye view projections that can be easily matched with simple field shaping. Thus, simple beam's eye view conformal planning techniques already have the ability to homogenously irradiate the target while maintaining a reasonably low dose to the nearby rectum and bladder. Although the conformal plans better avoided these structures, it was not sufficient to allow significant dose escalation while maintaining low tissue toxicity.

Other than radiosurgery cases, the only treatment site which did not show an advantage from intensity modulated treatments was the intact breast. For this site, the Peacock plans resulted in an undesirable target dose inhomogeneity and should not be used for such treatment plans. If one considers the geometry of this situation, it is clear that large gantry rotations are not necessary for treatment of the breast. Attempting to optimize these large arcs may force variation of too many variables and never result in an acceptable solution. A better approach may be to start with more traditional field arrangements, and determine the optimal profiles for a limited number of portals. This approach would essentially use the 3D conformal tool to produce fixed field compensators rather than to design dynamic treatments. Regardless, further work is required before the Peacock system should be used to develop treatment plans for the intact breast.

Regardless of the treatment site, this study further demonstrated that the probability of uncomplicated local control for conventional radiotherapy treatments is enhanced through the use of virtual simulation. Since this technique allows the physician to design the radiation portals while examining the three dimensional geometry of the patient, these portals were designed to better spare normal tissue in all cases examined. Further, this treatment planning technique virtually eliminates the possibility of geographic target miss caused by design of an inadequate radiation portal. After review of this and other studies, it can unequivocally be stated that virtual simulation should be used whenever practical.

Factors which effect the clinical outcome of conformal treatments were studied, including resolution of the intensity modulation device and use of noncoplanar beams. Although both of these techniques improve the dose gradient outside of the target volume, it was shown that neither results in a significant gain in probability of uncomplicated control for the cases studied. Thus for treatment of head and neck, lung and prostate cancers, single arc therapy using an intensity modulation device with 1 cm vanes generates an acceptable plan which is not needlessly complex.

The effect of patient positional uncertainties on the inverse radiotherapy plans was examined, assuming that all such errors are random and may be predicted by a gaussian distribution. It was demonstrated that these inaccuracies introduce negligible perturbation of the dose distribution for the conformal plans, since plans developed using the Peacock retain a small margin around the target volume. Once systematic errors are introduced into the treatment delivery, margins must be increased in order to ensure adequate target coverage. This is significant since toxicity is directly related to treatment volume, and the overall treatment volume increases dramatically with inclusion of a margin. For example, a 1 cm margin around an 8 cm diameter spherical target results in nearly a two fold increase in overall treatment volume. Although it is wise to maintain a small margin which ensures adequate coverage of the entire target and irradiation of microscopic disease, a primary goal of conformal therapy is to reduce this margin and thereby reduce toxicity. In order to allow such margin constriction and maximize the potential benefit from conformal radiotherapy, sources of both random and systematic error must be minimized.

Although this study examined the efficacy of inverse radiotherapy planning, it is difficult to separate limitations of inverse radiotherapy planning from limitations of the specific algorithm used to generate the plans. One of the primary obstacles in treatment planning optimization is selection of an appropriate objective function. The best score function would be one that maximized the probability of uncomplicated control with weights assigned denoting relative importance of critical structures, but this is currently impractical due to the previously discussed limitations of biological response models. The next obvious choice is a score function which requires the prescription dose within the target and zero dose elsewhere. Since this is physically impossible, however, optimization of such an objective function generally results in an unacceptable plan. The cost function within the Peacock is essentially such a function with weights assigned to each target and critical structure based on the user's opinion of their relative importance. Such simplistic score functions may not be sufficient, since it is difficult to formulate the desired result and the function may not be intuitively obvious. For example, the current score function contains no constraint on dose homogeneity within the target volume. Since high target dose homogeneity is required for many treatment sites, such a constraint must be included within the optimization. It is clear that further study is required in order to formulate a more appropriate objective function.

Another concern arises because it is known that simulated annealing may be trapped in local minima if the annealing schedule is not chosen properly. Choice of annealing schedule is unfortunately problem dependent, and thus choice of an appropriate schedule may be required prior to each treatment planning session. For example, the clinical plans generated using 5 mm vane widths showed no substantial improvement over those planned using the 10 mm vane widths and were actually worse in some cases. Since this outcome is illogical and unexpected due to computer simulations presented in this and other studies [Mos92], one questions the validity of the optimization algorithm. This increase in vane resolution does increase the complexity of the optimization and it may be argued that this places unreasonable demands on the algorithm. There were, however, plans within this study which never converged to an acceptable result even when using a conventional MIMIC configuration with 1 cm vane widths. Thus, the optimization technique currently used by the Peacock should be reevaluated.

The increased complexity and decreased efficiency of delivering intensity modulated treatments may impede its acceptance by the general radiotherapy community. Although difficulties such as these still exist they can be overcome, however, since it is felt that the benefits described within this study and others underway justify the efforts required to solve the technical problems. Considering the results of this study, problems which must be addressed in order to design the ideal inverse radiotherapy planning and delivery system are as follows. First, the time investment for delineation of critical structures must be reduced. Although Peacock has tools which aid the user, more sophisticated tools need to be developed which simplify or possibly automate the process. Incidentally, these tools are essential for all 3D treatment planning systems. The conformal planning system would also benefit from more sophisticated optimization and dose calculation algorithms. Simulated annealing, although one of the best optimization algorithms available, can fail to reach an optimal solution. This tendency is especially evident when trying to optimize a large number of dimensions as the Peacock system does. Further, this large number of dimensions causes the algorithm to be very slow. A superior approach is to analytically determined the required beam fluences through backprojection or deconvolution. If one wishes to further refine the dose distribution obtained in this manner, the relative weighting for each beam portal may be optimized as was done in a companion project to this work [Har94]. Forward dose calculation should then be performed utilizing a more sophisticated algorithm, such as convolution of monte carlo generated pencil beam kernels, which determines a more accurate dose and can take into account the effects of tissue inhomogeneities. Further, the software should be modified to constrain the allowable dose inhomogeneity within the targeted region.

Accurate transfer of the planning information to the treatment couch can be accomplished via techniques currently under development at University of Florida for high precision stereotactic radiotherapy [Yan94], and better methods of patient immobilization should be investigated for areas other than head and neck. Although treatments could be performed using the tomotherapy device proposed by Mackie, this dedicated unit is far too costly for the average clinic. Instead, a multileaf collimation system (1 cm vane width) which attaches to the linear accelerator head provides a more economical and flexible solution. A two dimensional "box" modulator would be the optimal solution, but at this point has not been proven practical. Since this device will attach directly to the linear accelerator head, mechanical accuracy must be ensured through tighter quality assurance specifications for these devices. After solving these problems, one is confronted with regulatory issues; part 10D-91 of the Florida Administrative Code requires that all compensators used for patient treatment must be verified. Since intensity modulated treatments are essentially dynamic compensation of the radiation beam, it seems that verification of each intensity modulated field delivered will inevitably be required. Thus, a method of verifying these fields must be developed, possibly through use of a megavoltage imaging system.

In conclusion, this work has demonstrated that 3D treatment planning is always advantageous, but intensity modulation of the radiation beam is beneficial only under specific conditions. In general, this conformal technique shows an advantage only for relatively large, irregular targets with critical structures in close proximity. Using the steps outlined in this conceptual work, intensity modulated conformal radiotherapy can be transformed into a clinically viable treatment modality for these irregular targets.

APPENDIX A
CALCULATION OF NORMAL TISSUE COMPLICATION PROBABILITY

The program NTCP.C utilizes the effective volume dose histogram reduction method to calculate the relative probability of complication associated with a treatment plan as described in chapter 5 of the text. NTCP.C requires command line input of basic prescription dosimetric parameters for the treatment plan in addition to the differential dose volume histogram generated for a critical structure of interest. The effective volume method is then utilized to reduce this DVH into a single bin with effective volume v_{eff} occurring at the point of maximum dose. This effective volume can in turn be utilized to determine an effective tolerance dose for partial volume irradiation of the organ. These parameters are then input into the standard normal probability distribution, which is numerically integrated using the trapezoidal rule to complete the NTCP calculation.

Although the calculation of complication probabilities associated with inhomogeneous irradiation cannot be tested in an absolute sense due to the limited available data, Kutcher and Burman have suggested that NTCP calculations should meet a set of boundary conditions if the calculational methodology is consistent [Kut91a]. These boundary conditions, and the program NTCP.C's ability to match them for idealized situations are as follows.

i) The calculation should be independent of the energy bin size used for the differential

DVH. Figure A-1 demonstrates the dependence of NTCP on the DVH bin size. Obviously, the utilization of a coarsely calculated DVH leads to an erroneous result and one should avoid the use of fewer than fifty bins when using NTCP.C. Kutcher and Burman found that a dose bin size of 2 Gy is adequate for their NTCP calculations in most clinical situations. Their calculation considers only treatments of 2 Gy/fraction, however. NTCP.C, which utilizes a variation of the linear quadratic formula in order to account for the effect of variable fraction sizes to each point within the critical volume, appears more sensitive to bin fluctuation and requires a bin size not larger than 1.5 Gy.

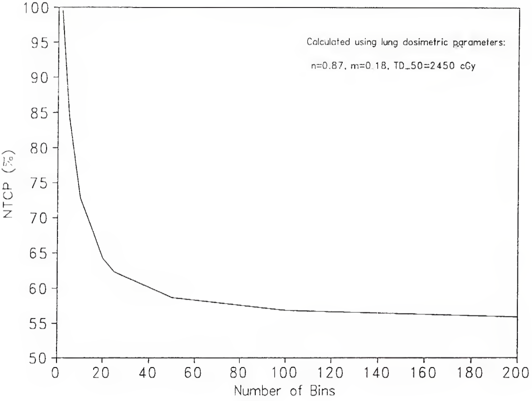

Figure A-1: NTCP as a function of bin size using NTCP.C with input DVH that decreases linearly from unity to zero volume over an 18 Gy dose range (18-36 Gy).

ii) Complication probabilities calculated for a homogenous differential dvh should yield the expected result for homogeneous irradiation. Figure A-2 depicts the cumulative dose volume histogram for homogenous irradiation of the liver to its TD_{50}. As required by the boundary condition, NTCP.C calculates a fifty percent complication probability.

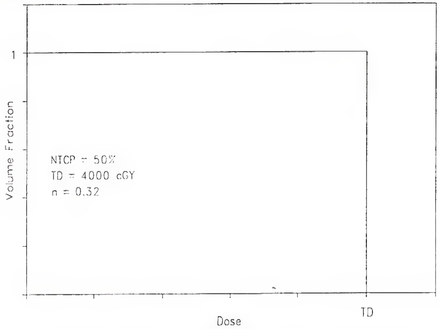

Figure A-2: DVH for homogeneous irradiation of the liver to its TD_{50} (4000 cGy). Note that calculated result (50%) matches the expected.

iii) Cold spots within the histogram should cause a reduction in the NTCP in relation to the size of the cold spot. Conversely, hot spots should produce an increase proportional to their size. Figure A-3 illustrates the consequences of cold or hot spots in the uniform histogram of figure A-2 upon input to NTCP.C.

iv) If two plans are produced for a particular organ, and the cumulative DVH_A is entirely within DVH_B, then $NTCP_A < NTCP_B$. This condition holds true for calculations using the idealized cases depicted in figures A-2 and A-3, and has also held true for clinical cases, as is demonstrated in figure A-4.

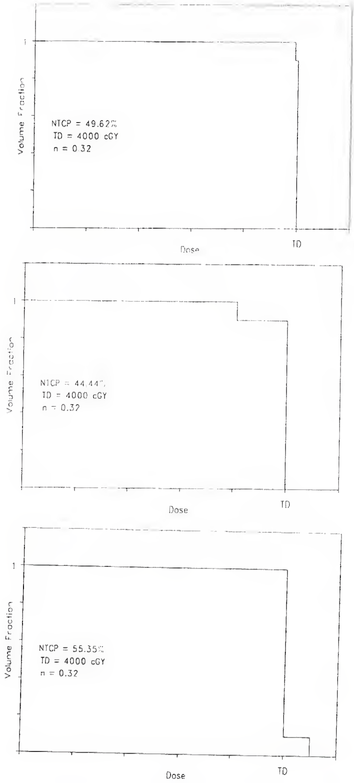

Figure A-3: NTCP calculations for hisotgrams containing a) small cold spot, b) large cold spot and c) small hot spot

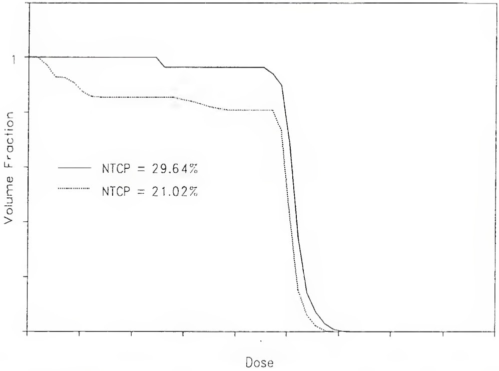

Figure A-4: NTCP calculations for dose volume histogram A enclosed within dvh B.

Tables A-1 through A-3 further demonstrate condition iv, and the effect of dose on NTCP calculations. The prescription doses for patients HN-1, L-1 and P-1 (see Chapter 6 for description) were varied by ±10%, and NTCP.C was utilized to calculate the complication probabilities. For most of the normal tissues, complication probability is negligibly effected by these small dose perturbations. This is reasonable since dose response is characterized by a sigmoid curve, and normal tissue doses are generally kept below the "knee" of the curve. The left lung dose for L-1 is high enough, however, that dose response is closer to the linear portion of the curve. Thus, the 10% increase in dose causes a larger increase in NTCP than is seen with the other tissues.

Table A-1: NTCP calculations for HN-1's 5 TA conformal plan with prescription dose escalated 10%, actual prescription dose and prescription dose de-escalated 10%.

Rx Dose (cGy)	Left Orbit	Left Optic Nerve	Brain Stem	Brain	Left Lens	Overall NTCP (%)
8228	0.0628	0.9627	0	0.0627	2.3732	3.4344
7480	0.0264	0.182	0	0.0142	1.5439	1.7630
6732	0.0110	0.0282	0	0	0.9874	1.0262

Table A-2: NTCP calculations for L-1's 5 TA conformal plan with prescription dose escalated 10%, actual prescription dose and prescription dose de-escalated 10%.

Rx Dose (cGy)	Left Lung	Right Lung	Trachea	Overall NTCP (%)
7480	19.7792	0	0.257	19.9854
6800	7.582	0	0.0846	7.6602
6120	2.3469	0	0.0267	2.3730

Table A-3: NTCP calculations for L-1's 5 TA conformal plan with prescription dose escalated 10%, actual prescription dose and prescription dose de-escalated 10%.

Prescription Dose (cGy)	Rectum	Bladder	Overall NTCP (%)
7524	0.8020	0	0.8020
6840	0.1444	0	0.1444
6156	0.0221	0	0.0221

```
/*  Program   NTCP.C   */
/*  This program utilizes the histogram reduction method of Kutcher and Burman   */
/*  [Kut91, Kut92] to calculate normal tissue complication probabilty.            */
/*  Written in ANSI C by Sanford Meeks at Shands Cancer Center 1993.              */
/* Last edited:  8/15/94  */

#include<stdlib.h>
#include<stdio.h>
#include<math.h>

#define SQ(x)       x*x
#define CONST        0.39894228    /*  1/(sqrt(2*pi))  */
#define EPS         1.0e-3        /*  Tolerance value for integration */
#define JMAX         20           /* Maximum number of integration steps */
#define FUNC(x)      ((*func)(x))

float qtrap(float (*func)(float), float a, float b);
float trapzd(float (*func)(float), float a, float b, int n);
void nrerror(char error_text[]);
float func(float x);

FILE  *dvh_ptr;

/*************************************************************************/
/*                     Main                                              */
/*************************************************************************/

void main (void)
{
 char dvh_file[15];
 float a, b, rxdose, isoline, d_max, v[250], v_i[250], d[250], v_eff, bin_frac, n, m, t,
   td_50, td_50_eff, v_frac, vol, z, bnd[250], bnd_max, alpha_beta, v_ref, v_std;
 int i, j, nbin, num_frac, crit_struct, type;

    printf("Pick critical structure of interest:\n");
    printf(" 1=>Bladder  2=>Brachial plexus  3=>Brain  4=>Brain stem\n\n
        5=>Cauda equina  6=>colon  7=>Ear (mid & exter) 8=>Esophagus\n\n
        9=>Femoral head & neck  10=>Heart  11=>Kidney  12=>Larynx\n\n
        13=>Lens 14=>Liver  15=>Lung  16=>Optic Nerve\n\n 17=>Optic
        chiasma  18=>Parotid  19=>Rectum  20=>Retina\n\n 21=>Rib cage
        22=>Skin  23=>small intestine  24=>spinal cord\n\n 25=>stomach
        26=>Thyroid  27=>TM joint and mandible 28=> Breast:\n");
     scanf("%d", &crit_struct);
```

```
if(crit_struct == 22){
  printf("Enter area of skin (sq cm) in CT data used for Tx planning:\n");
   scanf("%f",&vol);
  printf("Enter reference surface area (0 for default value):\n");
   scanf("%f", &v_ref);
}
else{
  if(crit_struct == 24){
    printf("Enter length (cm) of cord in CT data used for Tx planning:\n");
     scanf("%f",&vol);
    printf("Enter reference length (0 for default value):\n");
     scanf("%f", &v_ref);
  }
  else{
    printf("Enter volume (cc) of structure in CT data used for plan:\n");
     scanf("%f",&vol);
    printf("Enter reference (total) volume\n");
    printf("(0 for default value, -1 if same as volume in CT scan):\n");
     scanf("%f", &v_ref);
  }
}
printf("Enter prescribed dose (cGy):\n");
 scanf("%f", &rxdose);
printf("Enter prescribed isodose line (percent):\n");
 scanf("%f", &isoline);
printf("Enter number of fractions:\n");
 scanf("%d", &num_frac);
printf("Enter number of dvh bins:\n");
 scanf("%d", &nbin);

d_max = rxdose/isoline;  /* Maximum dose  (Gy)  */
bin_frac = 1.0/(float)nbin;

for(i = 1; i<= nbin; i++){
    d[i] = (float)i*bin_frac*d_max;
}
switch(crit_struct)
{
    case(1):  /*  Bladder  */
    {      n = 0.5; m = 0.11; td_50 = 80; alpha_beta = 2.0; v_std = 45.0;break;
    }
    case(2):  /*  Brachial plexus  */
    {      n = 0.03; m = 0.12; td_50 = 75; alpha_beta = 5.3;break;
    }
```

```
case(3):  /*  Brain  */
{     n = 0.25; m = 0.15; td_50=60; alpha_beta = 3.3; v_std = 1136.;break;
}
case(4):  /* Brain stem */
{      n=0.16; m=0.14; td_50=65; alpha_beta=2.0; v_std=30.0;break;
}
case(5):  /*  Cauda equina  */
{      n = 0.03; m = 0.12; td_50 = 75;  alpha_beta = 2.0;break;
}
case(6):  /*  Colon  */
{      n=0.17; m=0.11; td_50=55; alpha_beta=4.0; v_std=138.0;break;
}
case(7):  /*  Ear  */
{      n = 0.01; m = 0.15; td_50 = 40;  alpha_beta = 2.0;break;
}
case(8):  /*  Esophagus  */
{      n=0.06; m=0.11; td_50=68; alpha_beta=2.0; v_std=40.0;break;
}
case(9):  /*  Femoral head & neck  */
{      n = 0.25; m = 0.12; td_50 = 65;  alpha_beta = 2.0;break;
}
case(10):  /*  Heart  */
{      n=0.35; m=0.10; td_50=48; alpha_beta=2.0; v_std=450.0;break;
}
case(11):  /*  Kidney  */
{      n=0.70; m=0.10; td_50=28; alpha_beta=2.0; v_std=310.0; break;
}
case(12):  /* Larynx  */
{      n = 0.08; m = 0.17; td_50 = 70; alpha_beta = 4.0; v_std=28.0;break;
}
case(13):  /*  Lens  */
{      n = 0.30; m = 0.27; td_50 = 18;  alpha_beta=2.0;v_std=0.4;break;
}
case(14):  /*  Liver  */
{      n=0.32; m=0.15; td_50=40; alpha_beta=2.0;v_std=1800.0;break;
}
case(15):  /*  Lung  */
{     n = 0.87; m = 0.18; td_50 =24.5;  alpha_beta=3.8; v_std=1000.;break;
}
case(16):  /*  Optic nerve  */
{      n = 0.25; m = 0.14; td_50 = 55;  alpha_beta = 2.0;break;
}
case(17):  /*  Optic chiasm  */
{      n = 0.25; m = 0.14; td_50 = 65;  alpha_beta = 2.0;break;
```

```
    }
    case(18):  /*  Parotid  */
    {        n = 0.70; m = 0.18; td_50 = 46;  alpha_beta = 2.0;break;
    }
    case(19):  /*  Rectum  */
    {        n=0.12; m=0.15; td_50=80; alpha_beta=2.0; v_std=15.0;break;
    }
    case(20):  /*  Retina  */
    {       n = 0.20; m = 0.19; td_50 = 65;  alpha_beta = 2.0; v_std=15.0;break;
    }
    case(21):  /*  Rib cage  */
    {        n=0.10; m=0.21; td_50=68; alpha_beta=2.0; v_std=765.0;break;
    }
    case(22):  /*  Skin  */
    {       n = 0.10; m = 0.12; td_50 = 70; alpha_beta = 2.0; v_std=100.0;break;
    }
    case(23):  /*  Small intestine  */
    {        n=0.15; m=0.16; td_50=55; alpha_beta=2.0; v_std=640.0;break;
    }
    case(24):  /* Spinal cord  */
    {        n=0.05; m=0.175; td_50=65.5; alpha_beta=3.3; v_std = 20.0;break;
    }
    case(25):  /* Stomach  */
    {        n=0.15; m=0.14; td_50=65; alpha_beta=2.0; v_std=150.0;break;
    }
    case(26):  /*  Thyroid  */
    {        n=0.22; m=0.26; td_50=80; alpha_beta=2.0; v_std=20.0;break;
    }
    case(27):  /*  TM joint and mandible  */
    {        n = 0.07; m = 0.10; td_50 = 72;  alpha_beta = 2.0; break;
    }
   case(28):  /* Breast */
    {       n = 0.10; m = 0.12; td_50 = 80; alpha_beta = 2.0; v_std=1000; break;
    }
    default:{
            printf("Not an available organ, so using default parameters\n");
            n = 0.1; m = 0.1; td_50 = 60;  alpha_beta = 2.0;
            break;
    }
}
if(v_ref == 0.0){v_ref = v_std;}
else{
   if(v_ref == -1.0){v_ref = vol;}
}
```

```
   printf("Enter 1 -> cumulative dvh or 2 -> differential dvh\n");
     scanf("%d", &type);

printf("Enter input dvh file name:\n");
 scanf("%s", dvh_file);
if((dvh_ptr = fopen(dvh_file,"r")) == NULL)
{
   printf("***  Unable to open dvh file  ***");
   exit(0);
}
for(i = 1; i <= nbin; i++){
    fscanf(dvh_ptr, "%f", &v_i[i]);
   if(v_i[i] > 0.0) {d_max = d[i];}
}
fclose(dvh_ptr);

if(type == 1){
   for(i = 1; i<= nbin; i++){
          v[i] = v_i[i] - v_i[i+1];
   }
}
else{
   for(i = 1; i <= nbin; i++){
                 v[i] = v_i[i];
   }
}

   /* Calculate effective volume using dvh reduction */
for(i = 1; i <= nbin; i++){v_eff += v[i]*vol*pow(d[i]/d_max,1/n);}
v_frac = v_eff/v_ref;

td_50_eff = (td_50*pow(v_frac,-n))*(alpha_beta+2.0)/(alpha_beta+
     d_max/num_frac);

/* Determine integration limits */
t = (d_max - td_50_eff)/(td_50_eff*m);
a = -10;
b = t;
/* Perform numerical integration */
if(b < -4){printf("NTCP = 0%%\n");}
else{
   if( b > 4){printf("NTCP = 100%%\n");}
   else{
       z=qtrap(func,a,b);
```

```
            printf("NTCP = %.4f%%\n", 100*z);
        }
    }
  return;
}

/*************************************************************************/
/*  Numerical integration using trapezoidal rule. From Numerical Recipes     */
/*************************************************************************/
float qtrap(float (*func)(float), float a, float b)
{
        float trapzd(float (*func)(float), float a, float b, int n);
        void nrerror(char error_text[]);
        int j;
        float s,olds;

        olds = -1.0e30;
        for (j=1;j<=JMAX;j++) {
                s=trapzd(func,a,b,j);
                if (fabs(s-olds) < EPS*fabs(olds)) return s;
                olds=s;
}
        nrerror("Too many steps in routine qtrap");
        return 0.0;
}

/*************************************************************************/
/* From Numerical Recipes in C                                               */
/*************************************************************************/
float trapzd(float (*func)(float), float a, float b, int n)
{
        float x,tnm,sum,del;
        static float s;
        int it,j;

        if (n == 1) {
                return (s=0.5*(b-a)*(FUNC(a)+FUNC(b)));
        } else {
                for (it=1,j=1;j<n-1;j++) it <<= 1;
                tnm=it;
                del=(b-a)/tnm;
                x=a+0.5*del;
                for (sum=0.0,j=1;j<=it;j++,x+=del) sum += FUNC(x);
                s=0.5*(s+(b-a)*sum/tnm);
                return s;
        }
}
/*************************************************************************/
/*  Function to be integrated                                            */
/*************************************************************************/
float func(float x)
  {
        float f;
                f = CONST*exp(-0.5*SQ(x));   /* Std. Normal Distribution */
        return f;
   }

/*************************************************************************/
/*               Numerical Recipes standard error handler                */
/*************************************************************************/
void nrerror(char error_text[])
{
        fprintf(stderr,"Numerical Recipes run-time error...\n");
        fprintf(stderr,"%s\n",error_text);
        fprintf(stderr,"...now exiting to system...\n");
        exit(1);
}
```

APPENDIX B
CALCULATION OF TUMOR CONTROL PROBABILITY

The program TCP.C utilizes the biophysical model described in Chapter 5 to estimate the tumor control probability for an inhomogeneously irradiated tumor. As with NTCP.C, this program requires command line input of the treatment plan's prescription parameters in addition to the dose volume histogram associated with the target volume. This DVH is converted into a biologically normalized dose volume histogram using radiobiological parameters stored within the program, and these data are input into a variant of the linear quadratic formulation which calculates the probability of killing a clonogen. The program then utilizes gaussian distributions to represent the variability in intratumoral and interpatient clonogen sensitivities and determine a representative TCP for the irradiation conditions.

Analogous to NTCP calculation, the calculation of control probabilities associated with inhomogeneous tumor irradiation cannot be tested absolutely. Thus, the TCP.C will be required to meet the four boundary conditions discussed in Appendix A [Kut91, Kut89]. TCP.C's abilty to match these conditions is demonstrated as follows.

i) The calculation should be independent of the energy bin size used for the differential dvh. Figure B-1 demonstrates the dependence of TCP on the DVH bin size. Obviously, the utilization of a coarsely calculated DVH leads to an erroneous result and one should avoid the use of fewer than fifty bins when using TCP.C. Kutcher and Burman found that a dose bin size of 2 Gy is adequate for their NTCP calculations in most clinical situations. Their calculations were valid only for treatments of 2 Gy/fraction, however. TCP.C, which utilizes the BNDVH in order to account for the effect of variable fraction sizes to each point within the critical volume, appears more sensitive to bin fluctuation and requires a maximum bin size of 1.5 Gy.

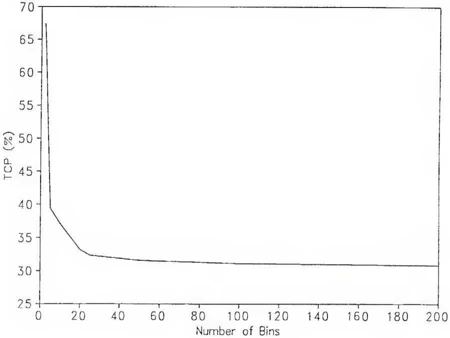

Figure B-1: TCP as a function of bin size using TCP.C with input DVH that decreases linearly from unity to zero volume over an 18 Gy dose range (18-36 Gy).

ii) Tumor control probabilities calculated for a homogenous differential dvh should yield the expected result for homogeneous irradiation. Figure B-2 depicts the cumulative dose volume histogram for homogenous irradiation of malignant tissue to its TCD_{50}. As can be seen in the figure, TCP.C does not return a value of exactly fifty percent for the complication probability. This due to the fact that the subroutine get_parameters iteratively alters the radiobiological parameters in order to force a match between the clinical data and the model's internal parameters [Nie94]. This iteration continues until the model prediction and the input data differ by less than the required accuracy of the model's estimated TCD_{50}. Since the required accuracy of this parameter defaults to 0.2 Gy, the calculated TCP will contain an inherent inaccuraccy. Greater accuracy in the TCP calculation can be obtained at the expense of increased calculation time. Since the model is valid only to give a relative score and it is understood this probability is not exact, the default accuracy is sufficient.

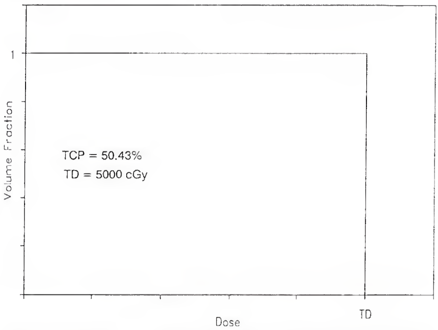

Figure B-2: DVH for homogenous irradiation of a tumor to its TCD_{50}.

iii) Cold spots within the histogram should cause a reduction in the TCP in relation to the size of the cold spot. Conversely, hot spots should produce an increase proportional to their size. Figure B-3 demonstrates the consequences of cold spots or hot spots in the uniform histogram of figure B-2 when input to TCP.C.

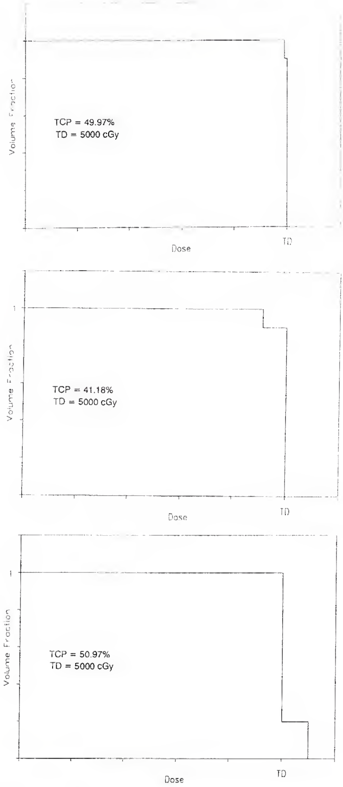

Figure B-3: TCP calulations for histograms with a) small cold spot, b) large cold spot and c) small hot spot.

iv) If two plans are produced for a particular organ, and the cumulative DVH_A is entirely enclosed within DVH_B, then $TCP_A < TCP_B$. This condition holds true for calculations using the idealized histograms depicted in figures B-2 and B-3, and has also held true for clinical cases, as is demonstrated in figure B-4.

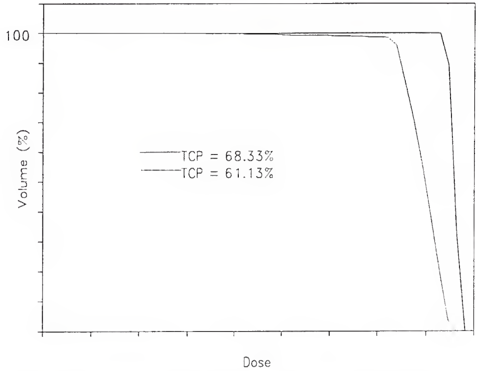

Figure B-4: TCP calculations for DVH_A enclosed entirely within DVH_B.

Tables B-1 through B-3 further demonstrate condition iv, and the effect of dose on TCP calculations. The prescription doses for patients HN-1, L-1 and P-1 (see Chapter 6 for description) were varied by ±10%, and TCP.C was utilized to calculate the tumor contol probabilities. In general, tumors are irradiated to a dose that is high enough to place their response on the linear portion of the dose response curve (i.e. probability of control is between 20 and 80 percent). Thus, the 10% variation in the dose is reflected in the calculation of TCP. For the prostate and seminal vesicles, however, probability of control is near the shoulder of the curve and a small dose variation does not tremendously effect the TCP calculation. The probability of uncomplicated control is also shown in the tables in order to demonstrate the overall effect of dose variation.

Table B-1: TCP calculation for HN-1's 5 TA conformal plan with prescription dose escalated 10%, actual prescription dose and prescription dose de-escalated 10%.

Prescription Dose (cGy)	TCP (%)	Score (%)
8228	66.4258	64.14
7480	60.3699	59.31
6732	49.0831	48.58

Table B-2: TCP calculation for L-1's 5 TA conformal plan with prescription dose escalated 10%, actual prescription dose and prescription dose de-escalated 10%.

Prescription Dose (cGy)	TCP (%)	Score (%)
7480	43.2785	34.63
6800	32.0263	29.57
6120	30.0492	29.34

Table B-3: TCP calculation for P-1's 5 TA conformal plan with prescription dose escalated 10%, actual prescription dose and prescription dose de-escalated 10%.

Prescription Dose (cGy)	$TCP_{prostate}$ (%)	$TCP_{sem\ ves}$ (%)	Score (%)
7524	69.6575	78.6158	54.33
6840	69.4186	78.2784	54.26
6156	68.3117	76.8999	52.52

Interestingly, the tumor dose response is not as steep as expected from general radiobiologic principles. From in vitro irradiation of cells, radiobiologists have determined a very steep sigmoidal relationship exists between cell kill and absorbed dose. Clinically, this steep relationship has not been exhibited, however [Oku93]. This flattening of the dose response curve has been attributed to heterogeneity in intratumoral and interpatient cell sensitivities [Sui92, Tha91] as schematically demonstrated in Figure B-5. Cell lines 1, 2 and 3 all have a steep dose response, but differ in thier relative radiation sensitivity. When one averages this dose response over the population, a more shallow relationship exists. Internally, the TCP model iteratively determines the variability in both intratumoral and interpatient cell sensitivities (i.e. spread between curves 1, 2 and 3 in Figure B-5) required to force agreement between laboratory radiobiology and clinical observations. The resultant TCP thus determined is in general more shallow than the corresponding NTCP. Therefore, while escalations in dose slightly improve tumor control probability, they reap little in terms of uncomplicated control. This effect is demonstrated in Figure B-6.

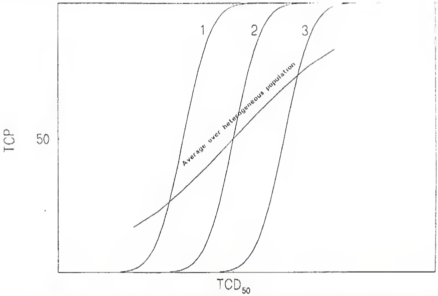

Figure B-5: Cell lines 1, 2 and 3 exhibit steep dose responses, although they differ in their relative sensitivities. For a heterogeneous population comprised of these cells, the dose response is much shallower, and dose escalation will not be easily detected.

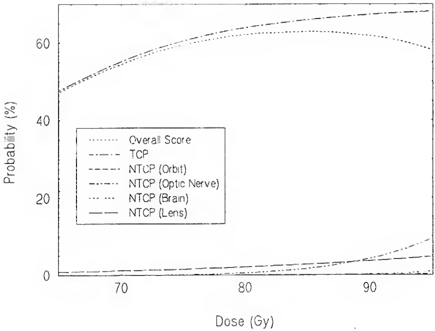

Figure B-6: Dose escalation for HN-1's five table angle conformal plan. While escalations in dose demonstrate a small benefit, the probability of uncomplicated control decreases once dose response for normal tissue is on the linear portion of the curve.

```
/* TCP.C */
/* Program which predicts the tumor control probability under conditions of          */
/* non-uniform tumor irradiation. This program is based on a biophysical model        */
/* developed by Niemierko and Goitein at Massachusetts General Hospital [Nie94].  */
/* Written in ANSI C by Sanford Meeks at Shands Cancer Center, 1993.                  */


#include<stdlib.h>
#include<stdio.h>
#include<math.h>

#define SQ(x)          x*x
#define lambda         8.0  /* Volume response parameter */
#define gamma_50_pop  2.0  /* Observed gamma_50 for a population */
#define CONST            0.39894228    /*  1/(sqrt(2*pi))  */
#define step_sigma    0.01  /* Resolution in sigma_pop space */
#define step_dose     0.1  /* Resolution in TCD_50 space */
#define R                4.0  /* Number of standard deviations for integration */
#define S               40.0  /* Number of steps for integration  */

void get_parameters(float tcd_50, float d[], float v[], float d_max, float d_bin, int nbins,
int nfrac, float alpha_beta);
float normal(float x, float m, float sigma);
float tcp_calc(int nbins,float d[],float v[],float nc,float sf_2, float sigma_pop, float
sigma_ind);

FILE  *dvh_ptr;

/************************************************************************/
/*                                    MAIN                                               */
/************************************************************************/

void main(void)
{
 char dvh_file[15];
 int tumor, i, nfrac, nbins;
 float alpha_beta, sum, tcp_est, tcd_50, isoline, rx_dose, d[150], sf, v[150], d_max,
     d_bin;

  printf("Choose target tissue:\n");
  printf("1=>Liposarcoma 2=>Melanoma 3=>Other Malignant 4=>AVM
         5=>Enter own parameters\n");
   scanf("%d", &tumor);
```

```
switch(tumor)
{
  case(1):
  {
    alpha_beta = 0.4;
    break;
  }
  case(2):
  {
    alpha_beta = 0.6;
    break;
  }
  case(3):
  {
    alpha_beta = 10;
    break;
  }
  case(4):
  {
    alpha_beta = 0.6;
    break;
  }

  case(5):
  {
    printf("Enter alpha/beta:\n");
      scanf("%f", &alpha_beta);
   break;
  }

  default:
  {
  printf("Only have radiobiological data for four different");
  printf("types of target tissue.\n");
  printf("Please try again.\n");
  exit(0);
  }
}
printf("Enter prescribed dose (cGy):\n");
 scanf("%f",&rx_dose);
printf("Enter prescribed isodose line (percent):\n");
 scanf("%f", &isoline);
printf("Enter the number of fractions:\n");
 scanf("%d", &nfrac);
 printf("Estimated TCP (percentage) if tumor were homogeneously\n");
 printf("irradiated to prescription dose\n");
  scanf("%f", &tcp_est);

 printf("Enter the number of dvh bins:\n");
  scanf("%d", &nbins);  printf("Enter 1 -> cumulative dvh or 2 -> differential
dvh\n");
  scanf("%d", &type);
 printf("Enter input dvh file name:\n");
  scanf("%s", dvh_file);
 if((dvh_ptr = fopen(dvh_file,"r")) == NULL)
 {
   printf("***  Unable to open dvh file  ***\n");
   exit(0);
 }
 for(i = 1; i <= nbins; i++){
   fscanf(dvh_ptr, "%f", &v_i[i]);  /* Fractional volume in the ith bin */
 }
 fclose(dvh_ptr);

 if(type == 1){
      for(i = 1; i<= nbins; i++){
           v[i] = v_i[i] - v_i[i+1];
      }
   }
   else{
      for(i = 1; i <= nbins; i++){
                 v[i] = v_i[i];
      }
   }


 d_max = rx_dose/isoline;  /* Maximum dose  (Gy)  */
 d_bin = 1.0/(float)nbins;  /* Fractional dose within each dvh bin */

 /* Calculate TCD_50 from estimated TCP */
 if(tcp_est == 50.0){tcd_50 = 0.01*rx_dose;}
 else{
    tcd_50 = 0.01*rx_dose*(gamma_50_pop)/(gamma_50_pop+0.01*(tcp_est-50.0));
 }
 printf("TCD_50 = %.2f Gy\n", tcd_50);

 get_parameters(tcd_50, d, v, d_max, d_bin, nbins, nfrac, alpha_beta);
}
```

```
/*****************************************************************************/
/*                          GET_PARAMETERS                                    */
/* Iterative procedure to estimate the inital number of nc, sigma_pop and    */
/* sigma_ind assuming that sigma_ind = sigma_pop/3. Based on Niemierko's      */
/* FORTRAN subroutine ESTIMATE_NC_SF2_AND_SIGMAS  [Nie94].                   */
/*****************************************************************************/

void get_parameters(float tcd_50, float d[150], float v[150], float d_max, float d_bin, int
nbins, int nfrac, float alpha_beta)
{
 float dose_50, sigma_pop, sigma_ind, nc, dose_40[5], dose_60[5], tcp_40;
 float tcp_60, gamma_50, sf_2, vol[5], d_frac[150], bnd[150], tcp;
 int i;
 printf("getting parameters\n");
 sf_2 = pow(10, -2/lambda);   /* Surviving fraction after 2 Gy */
 nc = log(2)*pow(10, tcd_50/lambda);  /* Number of tumor clonogens */
 vol[1] = 1.0;  /* Fractional volume for homogeneously irradiated tumor */
 while(fabs((double)tcd_50-(double)dose_50) > 0.2){  /* stop iteration when model */
                              /* prediction and input data differ less than 0.2 */
  sigma_pop = 0.0;
  gamma_50 = 2.5;
   while(gamma_50 >gamma_50_pop){
     sigma_pop += step_sigma;
     sigma_ind = sigma_pop/3;
     dose_40[1] = 0.0;
       tcp_40 = tcp_calc(1, dose_40, vol, nc, sf_2, sigma_pop, sigma_ind);
     while(tcp_40 < 0.40){
       dose_40[1] += step_dose;
       tcp_40 = tcp_calc(1, dose_40, vol, nc, sf_2, sigma_pop, sigma_ind);
     }
     dose_60[1] = dose_40[1];
       tcp_60 = tcp_40;
     while(tcp_60 < 0.60){
       dose_60[1] += step_dose;
       tcp_60 = tcp_calc(1, dose_60, vol, nc, sf_2, sigma_pop, sigma_ind);
     }
     dose_50 = (dose_40[1] + dose_60[1])/2;
     gamma_50 = tcd_50*(tcp_60 - tcp_40)/(dose_60[1] - dose_40[1]);
  }

   nc *= pow(sf_2, (dose_50 - tcd_50)*0.5);  /* Heterogeneity correction */
printf("dose_50=%.2ftcd_50=%.2fgamma_50=%.2f\n",dose_50,tcd_50,gamma_50);

 }                                      /* to make NC fit TCD_50    */
```

```
  /* Calculate biologically normalized dose volume histogram */
  for(i = 1; i <= nbins; i++){
     d[i] = (float)i*d_bin*d_max;  /* Average total dose in the ith bin */
     d_frac[i] = d[i]/(float)nfrac; /* Average fractional dose in the ith bin */
     /* Average total biologically normalized dose in the ith bin */
     bnd[i] = d[i]*(alpha_beta + d_frac[i])/(alpha_beta + 2.0);
  }
  tcp = tcp_calc(nbins, bnd, v, nc, sf_2, sigma_pop, sigma_ind);
  printf("TCP = %.4f\n", 100*tcp);

}


/*****************************************************************************/
/*                              TCP_CALC                                     */
/*  Calculates TCP for inhomogeneous dose distribution under conditions of   */
/*  heterogeneity of patient population and intratumoral heteregeneity.      */
/*  Based on Niemierko's FORTRAN subroutine TCP  [Nie94].                    */
/*****************************************************************************/

float tcp_calc(int nbins,float d[150],float v[150],float nc, float sf_2, float sigma_pop,
float sigma_ind)
{
  float step_pop, step_ind, norm_pop, tcp, sf_pop, fac_pop, ncs, sf_min;
  float sf_max, sf_eff, sf, norm_ind, tcp_ind, fac_ind, sf_ind;
  int i;

  sf_min = sf_2 - R*sigma_pop*sf_2;  /* Lower integration limit  */
  sf_max = sf_2 + R*sigma_pop*sf_2;  /* Upper limit */
  step_pop = sf_2*sigma_pop*2*R/S;  /* Integration step size (population) */
  step_ind = sf_2*sigma_ind*2*R/S;  /* Integration step size (individual) */
  norm_pop = 0.0;
  tcp = 0.0;
  if(step_pop == 0.0) {step_pop = 1.0;}  /* Only one level of integration */
  if(step_ind == 0.0) {step_ind = 1.0;}  /* if no variability exists      */

  sf_pop = sf_min - step_pop;
  while(sf_pop < sf_max){   /* Loop over patient population */
     sf_pop += step_pop;
     fac_pop = normal(sf_pop, sf_2, sf_2*sigma_pop);
     norm_pop += fac_pop;
     ncs = 0.0;
     for(i = 1; i <= nbins; i++){
        sf_ind = sf_pop - R*sigma_ind*sf_2 - step_ind;
        norm_ind = 0.0;
        sf_eff = 0.0;
        while(sf_ind < (sf_pop + R*sigma_ind*sf_2)){
          sf_ind += step_ind;
          fac_ind = normal(sf_ind, sf_pop, sf_2*sigma_ind);
          norm_ind += fac_ind;
          if(sf_ind < 0.0) { sf = 0.0;}
          else{
            if(sf_ind > 1.0) { sf = 1.0;}
              else{ sf = sf_ind;}
          }
          sf_eff += fac_ind*pow(sf, 0.5*d[i]);
        }
        sf_eff /= norm_ind;
        ncs += nc*v[i]*sf_eff;
      }
      tcp_ind = exp(-ncs);     /*  TCP for individual's tumor */
      tcp += fac_pop*tcp_ind;
    }

    tcp /= norm_pop;            /* Normalized TCP for population */
    return tcp;
  }

  /*****************************************************************************/
  /*                              NORMAL                                       */
  /*      Calculates normal probability density function.                      */
  /*****************************************************************************/

  float normal(float x, float m, float sigma)
  {
    float t, norm;
    t = (x-m)/sigma;
    norm = (CONST/sigma)*exp(-0.5*SQ(t));
    return norm;
  }
```

APPENDIX C
OPTIMIZATION OF INTENSITY MODULATION FUNCTIONS

Assuming a one-dimensional intensity modulation function (IMF) is prescribed in mm increments, the program ANN.C determines the optimal fit to this ideal IMF that can be obtained using a physical modulator with various configurations; the device may be modeled with 1, 2, 4, 5, 8, 10, 12, 15 and 20 mm wide vanes at isocenter, and may assume any number of equally spaced percentage transmission steps input by the user. For this simulation, an IMF was defined as the absorbed dose profile at the depth of D_{max} for a 6 MV x-ray beam and ANN.C attempts to minimize the difference between the physical and prescribed profiles through use of a simple least squares objective function:

$$\begin{matrix}\mathit{Objective}\\ \mathit{Function}\end{matrix} = (IMF_{prescribed} - IMF_{physical})^2$$

where $IMF_{physical}$ is calculated using the dose model discussed in Chapter 7.

Optimization within ANN.C is accomplished using the algorithm AMEBSA [Pre92], which is a variant of simulated annealing. AMEBSA is driven by an algorithm, AMOEBA, [Pre92] which is an optimization routine known as the downhill simplex method. This method replaces the single point x that describes the system, by a simplex of N+1 points. The simplex explores solution space by reflecting, expanding and contracting. Simulated annealing is incorporated into this algorithm through the addition of random values, proportional to the temperature, to the function value associated with each vertex of the simplex and subtract a similar value from every point associated with the new simplex [Pre92]. AMEBSA will always accept a true downhill step, but will sometimes accept an uphill one. Obviously, this makes AMEBSA more computationally intensive than simple downhill methods such as AMOEBA, but it also enables the algorithm to escape local traps.

Unfortunately, no perfect optimization algorithm exists, and there is no way to be certain that a chosen routine will obtain the global optimum for all possible situations. It is possible, however, to demonstrate an algorithm's ability to find the global solution for known functions. Two functions were chosen for this illustration. Figure C-1 illustrates the first function,

$$F_1 = x_1^2+2x_2^2-0.3\cos(3\pi x_1)-0.4\cos(4\pi x_2)+0.3+0.4 \quad ,$$

which contains numerous local extrema and a global minimum at (0,0). After 148 iterations, AMEBSA finds the global optimum. A second example is Colville's merit surface, which is a four dimensional function containing many local minima:

$$\begin{aligned} F_2 = {} & 100(x_2-x_1^2)^2 + (1-x_1)^2 + 90(x_4-x_3^2)^2 + (1-x_3)^2 + \\ & 10.1[(x_2-1)^2 + (x_4-1)^2] + 19.8(x_2-1)(x_4-1) \quad . \end{aligned}$$

AMEBSA easily finds the global optimum solution after only 10 iterations.

Although these two examples hardly provide definitive proof of the accuracy of the optimization algorithm, they do provide confidence in the code's ability to find the global minimum of known functions. As a double check of this optimization routine, all optimizations were performed twice: once using simulated annealing and once using the downhill simplex alone. Figure C-2 demonstrates the behavior of these two algorithms as a function of the number of dimensions varied for the optimization. As seen in the

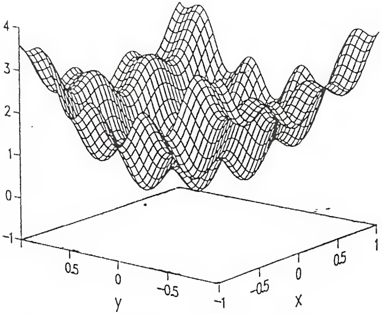

Figure C-1: Two-dimensional test function with many local minima and one global minimum at (0,0).

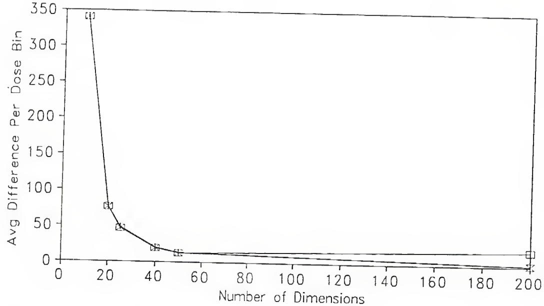

Figure C-2: Comparison of simulated annealing (hourglass) and downhill simplex (square) as a function of dimension.

figure, the objective function determined by both algorithms is approximately the same when a small number of dimensions are varied. As the number of dimensions increases, the complexity of the optimization also increases, and the purely downhill algorithm becomes easily trapped in a local minimum.

ANN.C requires command line input of several parameters before it can begin the optimization process, and prompts the user for these data. The requisite input include number of vanes, number of attenuation steps on each vane and a file which contains the ideal prescribed IMF as described in Chapter 7 of the text. ANN.C assumes that the length of the slit is 20 cm, and divides the slit into vanes of equivalent width based on the user input. ANN.C then determines the available transmission values by allowing equivalent increments of percentage transmission consistent with the user input. Upon completion of the optimization, ANN.C outputs a file which is suitable for input to either EasyPlot™ on a personal computer or Advanced Visual Systems (AVS) software on a SUN SPARCstation™. Due to the large array sizes required for fine vane resolution, it is recommended that ANN.C and its output run exclusively on the SUN.

```
/************************************************************************/
/* Optimization of slit IMF using simulated annealing and downhill simplex.     */
/* Given a prescribed intensity modulation function for a slit intensity        */
/* modulator, this program determines the transmission values required in       */
/* in order to produce the physical IMF which most closely matches the          */
/* prescribed IMF.  The physical IMF may be produced utilizing different        */
/* configurations of the modulation device in order to investigate vane         */
/* and attenuation resolution requirements.                                     */
/* Written in K&R C by Sanford Meeks at Shands Cancer Center, 1993.             */
/************************************************************************/

#include <math.h>
#include <stdio.h>
#include <stdlib.h>
#include<malloc.h>

#define  SQ(x)   ((x)*(x))
#define  GET_PSUM \
             for (n=1;n<=ndim;n++) {\
             for (sum=0.0,m=1;m<=ndim+1;m++) sum += p[m][n];\
             psum[n]=sum;}

/** Constants required for simplex manipulation  **/
#define  ALPHA   1.0    /*  reflection coefficient  */
#define  BETA    0.5    /*  contraction coefficient  */
#define  GAMMA   2.0    /*  expansion coefficient  */
#define  K       200.0  /* anealing schedule coefficient  */

/* Dose calculation constants  */
#define  SAD     100
#define  SSD     98.5   /* Assuming flat water phantom and d_max = SAD */

/**  Constants required for random number generator  **/
#define IA 16807
#define IM 2147483647
#define AM (1.0/IM)
#define IQ 127773
#define IR 2836
#define NTAB 32
#define NDIV (1+(IM-1)/NTAB)
#define EPS 1.2e-7
#define RNMX (1.0-EPS)
#define BACKSPACE  8
```

```
float amotsa();
void amebsa();
float funk();
float ran1();
float *vector();
void free_vector();
void nrerror();
void input();
void nmf();
void dose_calc();

FILE *imf_ptr;
FILE *oar_ptr;
FILE *x_ptr;
FILE *sc_ptr;

/* global variable declarations */
long idum = (-64);
float obj, tt;
float imf[500], sc[500], oar[500], scat[500], tot[500];
int ndim, spinpos;

/*************************************************************************/
/*                        Main                                           */
/*************************************************************************/

void main(argc,argv)
int argc, **argv;
{
  char xfile[15], outfile[15];
  int col, i, iiter, iter, j, jiter, nit, row, m, l, z, nvans, wvan, sched;
  double mul, per;
  float a, ftol, ps, qs, temptr, yb, ybb, nstps, pstps;
  float p[500][500], pb[500], x[500], xtry[500], xpos[500];
  float xhpos[500], y[500], xnew[500], xvan[500];
  FILE *outfp;

        iiter = 500;      /* # of iterations before temp reduction */
        nit = 0;
        yb = 1.0e30;    /* initialization of "best" y-value */
        ybb = 1.0e30;
        ftol = 1.0e-6;  /* fractional convergence tolerance */
        a = 0.1;        /* characteristic length scale */
```

```
/*  Input specific characteristics of intensity modulator.  */

   printf("Number of vanes (10, 20,25,40,50 or 200)?\n");
   scanf("%d", &nvans);
   if( nvans < = 0){
           printf("Number of vanes must be greater than zero\n");
           exit(0);
   }

   ndim = nvans;        /* number of dimensions */
   printf("Number of attenuation values for each vane (1 for unconstrained)?\n");
   scanf("%f", &nstps);

   ps = a*((sqrt((double)ndim + 1.0) + ndim)/(ndim*1.4142));
   qs = a*((sqrt((double)ndim + 1.0) - 1.0)/(ndim*1.4142));

   /* Define input vector, x[1...ndim] */

   printf("Enter input vector file name:\n");
           scanf("%s", xfile);
           if((x_ptr = fopen(xfile,"r")) = = NULL)
           {
                   printf("***  Unable to open input vector file  ***");
                   exit(0);
           }
           for(j = 1; j < = ndim; j+ +){
                   fscanf(x_ptr, "%f", &x[j]);
           }
           fclose(x_ptr);

   /* Define input matrix p[1...ndim+1][1...ndim]. Its ndim+1 rows are ndim
      vectors which form the vertices of the starting simplex.  */

           for(col = 1; col < = ndim; col+ +){
                           p[1][col] = x[col];
           }
           for(row = 2; row < = ndim + 1; row+ +){
                   for(col = 1; col < = ndim; col+ +){
                           if(row = = col + 1)
                           {
                           p[row][col] = x[col] + ps;
                           }
                           else
                           {
                                p[row][col] = x[col] + qs;
                                }
                        }
                }

        /* Define input parameters. */
        input();

        /* Define y[1...ndim+1], which  is a vector whose components are
           preinitialized to the values of funk evaluated at the ndim+1
                vertices (rows) of p[][] */
        for(row = 1; row <= ndim + 1; row++){
                for(col = 1; col <= ndim; col++){
                                xtry[col] = p[row][col];
                }

                        y[row] = funk(xtry);
        }

        spinpos = 0; /* initialize whirly-thing */

        /* Select annealing schedule  */

        printf("Select:  1 -> downhill simplex\n\t 2 -> annealing schedule 1\n\t 3 ->
annealing schedule 2\n");
        scanf("%d", &sched);

        switch(sched)
        {
                case(1):{

                        /* Perform optimization using downhill simplex only. */
                        temptr = 0.0;
                        printf("iteration #  ");
                        for(jiter = 0; jiter < 150; jiter++){
                                iter = iiter;
                                printf("%c%c", BACKSPACE, BACKSPACE);
                                if(jiter > 99){
                                        printf("%c%c",BACKSPACE, BACKSPACE);
                                }
                                else{
                                        if(jiter > 9){
                                                printf("%c", BACKSPACE);
                                        }
                }
                printf("%d ", jiter + 1);
                amebsa(p,y,ndim,pb,&yb,ftol,&iter,temptr);
                nit += iiter - iter;
                if(yb < ybb){
                        ybb = yb;
                }
        }
        break;
}

case(2):{

        /* Simulated annealing optimization. Annealing schedule
           simply reduces the temperature by 0.8 for each of the
          150 iterations.  */
      temptr = 1000.0;
        printf("Annealing ... iteration #  ");
        for(jiter = 0; jiter < 150; jiter++){
                iter = iiter;
                temptr *= 0.8;
                printf("%c%c", BACKSPACE, BACKSPACE);
                if(jiter > 99){
                        printf("%c%c",BACKSPACE, BACKSPACE);
                }
                else{
                        if(jiter > 9){
                                printf("%c", BACKSPACE);
                        }
                }
                printf("%d ", jiter + 1);
                amebsa(p,y,ndim,pb,&yb,ftol,&iter,temptr);
                nit += iiter - iter;
                if(yb < ybb){
                        ybb = yb;
                }
        }
        break;
}

case(3):{

      /*  After iiter amoeba evaluations temptr is reduced
         by SQ(1-jiter/K). This is performed jiter times. */
```

```
                temptr = 1000.0;
                printf("Annealing ... iteration #  ");
                for(jiter = 0; jiter < 150; jiter++){
                        iter = iiter;
                        per = 1 - ((double)jiter/K);
                        mul = pow(per, 2.0);
                        temptr *= mul;
                        printf("%c%c", BACKSPACE, BACKSPACE);
                        if(jiter > 99){
                        printf("%c%c",BACKSPACE, BACKSPACE);
                        }
                        else{
                                if(jiter > 9){
                                        printf("%c", BACKSPACE);
                                }
                        }
                        printf("%d ", jiter + 1);
                        amebsa(p,y,ndim,pb,&yb,ftol,&iter,temptr);
                        nit += iiter - iter;
                        if(yb < ybb){
                        ybb = yb;
                        }
                }
                break;
        }
        default: {
        printf("You may use annealing schedule 1, 2 or 3 =>\n");
        printf("Please restart program and use ");
        printf("one of these schedules\n");
        exit(0);
        }
}

printf("obj = %.4f\n", obj);

if(nstps == 1){
        for(m = 1; m <= ndim; m++){
                xnew[m] = p[1][m];
        }
}
else{
        pstps = 1.00/nstps;
        for(l= 0; l <= nstps; l++){
                if(l == 0){
```

```
                          xpos[l] = 0.006;
                          xhpos[l] = (l + 0.5)*pstps;
                  }
                  else{
                          xpos[l] = l*pstps;
                          xhpos[l] = (l + 0.5)*pstps;
                  }
          }
          for(m = 1; m <= ndim; m++){
                  for(l = 0; l <= nstps; l++){
                          if(p[1][m] >= xpos[l] && p[1][m] < xhpos[l]){
                                  p[1][m] = xpos[l];
                          }
                          if(p[1][m] >= xhpos[l] && p[1][m] < (xpos[l] + pstps)){
                                  p[1][m] = xpos[l] + pstps;
                          }
                  }
                xnew[m] = p[1][m];
          }
  }
  wvan = 200/nvans;
          for(i = 1; i <= nvans; i++){
                  if(i == 1){
                          for(z = 1; z <= wvan; z++){
                                  xvan[z] = xnew[i];
                          }
                  }
                  else {
                          for(z = (wvan*(i - 1) + 1); z <= wvan*i; z++){
                                  xvan[z] = xnew[i];
                          }
                  }
          }

/**  Define and open output vector file  **/

   printf("\n Enter transmission value file name:\n");
        scanf("%s", outfile);
  if((outfp = fopen(outfile, "w")) == NULL)
  {
          printf("***  Unable to open output file %s ***\n", outfile);
          exit(0);
  }
  /*  Print optimized transmission values to file.  */
```

```
        for(j = 1; j <= ndim; j++){
                fprintf(outfp,"%.4f\n", pb[j]);
        }
        printf("\n");
        fclose(outfp);

        /* Calculate optimized physical intensity modulation function.  */
        nmf(xvan);

        /* Calculate 2d dose distribution.  */
        dose_calc();
}

/**************************************************************************/
/*                              Input                                     */
/*    This subroutine is called to open  IMF, OAR and scatter files.      */
/**************************************************************************/

void input()
{
        char imfile[15], outfile[15];
        int m, o, s;

/**  Define and open intensity modulation function file  **/
                if((imf_ptr = fopen("fsin.pre", "r")) == NULL)
                {
                                printf("***  Unable to open IMF file  ***");
                                exit(0);
                }
                for(m = 0; m <= ndim; m++){
                                fscanf(imf_ptr, "%f", &imf[m]);
        }
                fclose(imf_ptr);

/* Open oar and scatter files for specific vane configuration */
switch(ndim)
{
        case(10): {
           /**  Open scatter file  **/

          if((sc_ptr = fopen("sn10.dat", "r")) == NULL)
          {
                        printf("***  Unable to open scatter file  ***");
                        exit(0);
```

```
  }
  for(s = 0; s <= ndim; s++){
            fscanf(sc_ptr, "%f", &sc[s]);
  }
  fclose(sc_ptr);

  /** Open oar file **/

  if((oar_ptr = fopen("oar10.dat", "r")) == NULL)
  {
      printf("***  Unable to open OAR file  ***");
      exit(0);
  }
  for(o = 0; o <= ndim; o++) {
            fscanf(oar_ptr, "%f", &oar[o]);
  }
  fclose(oar_ptr);
break;
}

case(20): {

   /** Open scatter file **/

  if((sc_ptr = fopen("sn20.dat", "r")) == NULL)
  {
            printf("***  Unable to open scatter file  ***");
            exit(0);
  }
  for(s = 0; s <= ndim; s++){
            fscanf(sc_ptr, "%f", &sc[s]);
  }
  fclose(sc_ptr);

  /** Open oar file **/

  if((oar_ptr = fopen("oar20.dat", "r")) == NULL)
  {
      printf("***  Unable to open OAR file  ***");
      exit(0);
  }
  for(o = 0; o <= ndim; o++) {
            fscanf(oar_ptr, "%f", &oar[o]);
  }
  fclose(oar_ptr);
break;
}

case(25): {

        /** Open scatter file **/

  if((sc_ptr = fopen("sn25.dat", "r")) == NULL)
 {
            printf("*** Unable to open scatter file ***");
            exit(0);
  }
  for(s = 0; s <= ndim; s++){
            fscanf(sc_ptr, "%f", &sc[s]);
  }
  fclose(sc_ptr);

  /** Open oar file **/

  if((oar_ptr = fopen("oar25.dat", "r")) == NULL)
  {
      printf("*** Unable to open OAR file ***");
      exit(0);
  }
  for(o = 0; o <= ndim; o++) {
            fscanf(oar_ptr, "%f", &oar[o]);
  }
  fclose(oar_ptr);
break;
}


case(40): {

  /** Open scatter file **/

  if((sc_ptr = fopen("sn40.dat", "r")) == NULL)
 {
            printf("*** Unable to open scatter file ***");
            exit(0);
  }
  for(s = 0; s <= ndim; s++){
            fscanf(sc_ptr, "%f", &sc[s]);
  }
  fclose(sc_ptr);

  /**  Open oar file  **/

  if((oar_ptr = fopen("oar40.dat", "r")) == NULL)
  {
       printf("***  Unable to open OAR file  ***");
       exit(0);
  }
  for(o = 0; o <= ndim; o++) {
              fscanf(oar_ptr, "%f", &oar[o]);
  }
  fclose(oar_ptr);
break;
}

case(50): {

  /**  Open scatter file  **/

  if((sc_ptr = fopen("sn50.dat", "r")) == NULL)
  {
              printf("***  Unable to open scatter file  ***");
              exit(0);
  }
  for(s = 0; s <= ndim; s++){
              fscanf(sc_ptr, "%f", &sc[s]);
  }
  fclose(sc_ptr);

  /**  Open oar file  **/

  if((oar_ptr = fopen("oar50.dat", "r")) == NULL)
  {
       printf("***  Unable to open OAR file  ***");
       exit(0);
  }
  for(o = 0; o <= ndim; o++) {
              fscanf(oar_ptr, "%f", &oar[o]);
  }
  fclose(oar_ptr);
break;
}
```

```
case(100): {

  /**  Open scatter file  **/

  if((sc_ptr = fopen("sn100.dat", "r")) == NULL)
  {
              printf("***  Unable to open scatter file  ***");
              exit(0);
  }
  for(s = 0; s <= ndim; s++){
              fscanf(sc_ptr, "%f", &sc[s]);
  }
  fclose(sc_ptr);

  /**  Open oar file  **/

  if((oar_ptr = fopen("oar100.dat", "r")) == NULL)
  {
      printf("***  Unable to open OAR file  ***");
      exit(0);
  }
  for(o = 0; o <= ndim; o++) {
              fscanf(oar_ptr, "%f", &oar[o]);
  }
  fclose(oar_ptr);
break;
}

case(200): {

  /**  Open scatter file  **/

  if((sc_ptr = fopen("fsn.dat", "r")) == NULL)
  {
              printf("***  Unable to open scatter file  ***");
              exit(0);
  }
  for(s = 0; s <= ndim; s++){
              fscanf(sc_ptr, "%f", &sc[s]);
  }
  fclose(sc_ptr);

  /**  Open oar file  **/
```

```
            if((oar_ptr = fopen("foar.dat", "r")) == NULL)
            {
                printf("***  Unable to open OAR file  ***");
                exit(0);
            }
            for(o = 0; o <= ndim; o++) {
                        fscanf(oar_ptr, "%f", &oar[o]);
            }
            fclose(oar_ptr);
          break;
          }
    default: {

          printf("The only possible mim configurations \n ");
          printf("contain 10,20,25,40,50,100 or 200 vanes\n");
          printf("Please restart program using\n");
          printf("one of these configurations\n");
       exit(0);
       }
   }


          return;
}

/**************************************************************************/
/*                              Amebsa                                    */
/*        This subroutine performs multidimensional minimization of the   */
/*                    function funk(x).  [Pre90]                          */
/**************************************************************************/

void amebsa(p,y,ndim,pb,yb,ftol,iter,temptr)
float p[500][500],*yb,ftol,pb[],temptr,y[500];
int *iter,ndim;
{
        int col, i,ihi,ilo,j,m,n,mpts=ndim+1, row;
        float rtol,sum,swap,yhi,ylo,ynhi,ysave,yt,ytry,psum[500];
        tt = -temptr;
        GET_PSUM

       /* First, we determine which point is the highest (worst), next highest
           and lowest (best).  */

        for (;;) {
```

```
      ilo=1;
      ihi=2;
      ynhi=ylo=y[1]+tt*log(ran1(&idum)+EPS); /* Add a random number */
      yhi=y[2]+tt*log(ran1(&idum)+EPS); /* proportional to temptr. */
      if (ylo > yhi) {
             ihi=1;
             ilo=2;
             ynhi=yhi;
             yhi=ylo;
             ylo=ynhi;
      }

      /*  Loop over the points in the simplex and add more random  */
      /*  thermal fluctuations.  */

      for (i=3;i<=mpts;i++) {
             yt=y[i]+tt*log(ran1(&idum)+EPS);
             if (yt <= ylo) {
                    ilo=i;
                    ylo=yt;
             }
             if (yt > yhi) {
                    ynhi=yhi;
                    ihi=i;
                    yhi=yt;
             } else if (yt > ynhi) {
                    ynhi=yt;
             }
      }
/* Compute fractional range from highest to lowest and return  if   */
/* satisfactory.  If returning, put best point and value in slot 1. */
      rtol=2.0*fabs(yhi-ylo)/(fabs(yhi)+fabs(ylo));
      if (rtol < ftol || *iter < 0) {
             swap=y[1];
             y[1]=y[ilo];
             y[ilo]=swap;
             for (n=1;n<=ndim;n++) {
                    swap=p[1][n];
                    p[1][n]=p[ilo][n];
                    p[ilo][n]=swap;
             }
             break;
      }
      *iter -= 2;
```

```
    /*  printf(".");*/
      /* Begin a new iteration. First extrapolate by a factor -ALPHA through
         the face of the simplex across from the high point, i.e.,
           reflect the simplex from the high point.  */
              ytry=amotsa(p,y,psum,ndim,pb,yb,ihi,&yhi,-ALPHA);
              if (ytry <= ylo) {

       /* Gives a result better than the best point so far, so  */
      /*  try an additional extrapolation by a factor GAMMA.     */
                      ytry=amotsa(p,y,psum,ndim,pb,yb,ihi,&yhi,GAMMA);
              } else if (ytry >= ynhi) {

      /*  The reflected point is worse than the second-highest, so look */
      /*  for an intermediate lower point by performing a one    */
                      /*  dimensional contraction.  */
                      ysave=yhi;
                      ytry=amotsa(p,y,psum,ndim,pb,yb,ihi,&yhi,BETA);
                      if (ytry >= ysave) {

              /* Can't get rid of the high point so contract
                 around the lowest (best) point.  */
                              for (i=1;i<=ndim+1;i++) {
                                      if (i != ilo) {
                                              for (j=1;j<=ndim;j++) {

psum[j]=0.5*(p[i][j]+p[ilo][j]);

                                                      p[i][j]=psum[j];
                                              }
                                              y[i]= funk(psum);
                                      }
                              }

                              *iter -= ndim;
                              GET_PSUM
                      }
              } else ++(*iter);   /* Correct the evaluation count. */
      }
}

/*************************************************************************/
/*                            Amotsa                                     */
/*   Extrapolates by a factor fac through the face of the simplex across */
/*   from the high point, tries it and replaces the high point if the new */
/*                         point is better.  [Pre90]                           */
/******************************************************************************/

float amotsa(p,y,psum,ndim,pb,yb,ihi,yhi,fac)
float p[500][500],*yb,*yhi,fac,*pb,psum[500],y[500];
int ihi,ndim;
{
        char *spinner = {"\\|/-"};
        int j;
        float fac1,fac2,yflu,ytry,ptry[500];
        fac1=(1.0-fac)/ndim;
        fac2=fac1-fac;
        for (j=1;j<=ndim;j++)
                ptry[j]=psum[j]*fac1-p[ihi][j]*fac2;
        printf("%c%c", spinner[spinpos++], BACKSPACE);
        spinpos &= 0x03;
        ytry = funk(ptry);  /* Evaluate the function at the trial point  */
        if (ytry <= *yb) {  /* save the best ever.  */
                for (j=1;j<=ndim;j++) pb[j]=ptry[j];
                *yb=ytry;
        }
        yflu=ytry-tt*log(ran1(&idum)+EPS);  /*  Subtract a thermal fluctuation to */
        if (yflu < *yhi) {              /*  give the simplex a Brownian motion. */
                y[ihi]=ytry;
                *yhi=yflu;
                for (j=1;j<=ndim;j++) {
                        psum[j] += ptry[j]-p[ihi][j];
                        p[ihi][j]=ptry[j];
                }
        }
        return yflu;

}

/******************************************************************************/
/*                                   Funk                                      */
/*                         Function to be minimized.                           */
/******************************************************************************/

float funk(x)
float x[500];
{
        int j;
        register int  bin, i;
        /* initialization */
        obj = 0.0;
        tot[bin] = 0.0;

      /** Profile calculation using semiempirical dose model **/

         for(bin = 1; bin <= ndim; bin++) {
                scat[bin] = 0.0;
            for(i = 1; i <= ndim; i++) {
                    if(bin == 1) {
                            scat[bin] = scat[bin] + x[i]*sc[i]*oar[i];
                    }
                    else {
                            if(i < bin) {
                                    j = bin - i + 1;
                            }
                            else {
                                    j = i - bin + 1;
                            }
                            scat[bin] = scat[bin] + x[i]*sc[j]*oar[i];
                    }
                    tot[bin] = 84.6*x[bin]*oar[bin] + scat[bin];
            }

/** Function to be minimized (objective function) **/

        obj = obj + SQ(tot[bin] - imf[bin]);
              /* Assign a penalty if optimization requires unphysical */
             /*              transmission values  */
              if(x[bin] <= 0.006 || x[bin] >= 1.00){
                      obj = 1000*obj;
              }
        }
        return obj;
}

/***************************************************************************/
/*                              Ran1                                       */
/* Minimal random number generator of Park and Miller with Bays-Durham     */
/* shuffle.  Returns a uniform random number between 0.0 and 1.0.  Use     */
/* idum to call a negative integer to initialize.  RNMX approximates the   */
/* largest float < 1 [Pre90].                                              */
/*                                                                         */
/***************************************************************************/
```

```
float ran1(idum)
long *idum;
{
        int j;
        long k;
        static long iy=0;
        static long iv[NTAB];
        float temp;

        /* Initialize */

        if (*idum <= 0 || !iy) {
                if (-(*idum) < 1) *idum=1;  /* Prevent idum = 0 */
                else *idum = -(*idum);
                /* Load shuffle table */
                for (j=NTAB+7;j>=0;j--) {
                        k=(*idum)/IQ;
                        *idum=IA*(*idum-k*IQ)-IR*k;
                        if (*idum < 0) *idum += IM;
                        if (j < NTAB) iv[j] = *idum;
                }
                iy=iv[0];
        }

        /* Start here when not initializing. */

        k=(*idum)/IQ;
        *idum=IA*(*idum-k*IQ)-IR*k;
        if (*idum < 0) *idum += IM;
        j=iy/NDIV;
        iy=iv[j];       /* Output stored value and refill shuffle table */
        iv[j] = *idum;
        if ((temp=AM*iy) > RNMX) return RNMX;
        else return temp;
}

/****************************************************************************/
/*                              *vector                                     */
/*          Allocates a float vector with range [nl..nh].  [Pre88].          */
/****************************************************************************/

float *vector(nl, nh)

int nl, nh;
```

```
{
      float *v;

      v = (float *)malloc((unsigned) (nh - nl + 1)*sizeof(float));
      if (!v) nrerror("allocation failure in vector()");
      return v - nl;
}

/***********************************************************************/
/*                          free_vector                                */
/*        Frees a float vector allocated by vector() [Pre88]           */
/***********************************************************************/

void free_vector(v, nl, nh)

float *v;
int nl, nh;
{


      free((char*) (v + nl));
}

/***********************************************************************/
/*                            nrerror                                  */
/*      Invoked to terminate program execution when a fatal error is  */
/*      encountered.  From Numerical Recipes in C [Pre88].             */
/***********************************************************************/

void nrerror(error_text)

char *error_text;
{
      fprintf(stderr, "Numerical Recipes run-time error...\n");
      fprintf(stderr, "%s\n", error_text);
      fprintf(stderr, "...now exiting to system...\n");
      exit(1);
}

/***********************************************************************/
/*                              nmf                                    */
/* This subroutine calculates new intensity modulation function on     */
/* millimeter grid in order to force equivalent objective function     */
/* sampling frequencies regardless of mim configuration.               */
```

```
/****************************************************************************/

void nmf(xvan)
float xvan[500];
{
        FILE *out_ptr;
        FILE *foar_ptr;
        FILE *sn_ptr;
        FILE *fimf_ptr;

        float foar[500], sn[500], fimf[500];
        char imfout[15];
        float add, lbin, rbin;
        int j, m, o, s, bin, i;

        /* Open prescription IMF file */

        if((fimf_ptr = fopen("fsin.pre", "r")) == NULL)
                {
                                printf("*** Unable to open IMF file ***");
                                exit(0);
                }
                for(m = 0; m < 201; m++){
                                fscanf(fimf_ptr, "%f", &fimf[m]);
                }
                fclose(fimf_ptr);

        /* Open scatter file */

          if((sn_ptr = fopen("fsn.dat", "r")) == NULL)
          {
                        printf("*** Unable to open scatter file ***");
                        exit(0);
          }
          for(s = 0; s < 201; s++){
                        fscanf(sn_ptr, "%f", &sn[s]);
          }
          fclose(sn_ptr);

          /* Open oar file */

          if((foar_ptr = fopen("foar.dat", "r")) == NULL)
          {
               printf("*** Unable to open OAR file ***");
        exit(0);
  }
  for(o = 0; o < 201; o++) {
                fscanf(foar_ptr, "%f", &foar[o]);
  }
  fclose(foar_ptr);

/* Define and open output IMF file. */

printf("\n Enter output IMF file name:\n");
     scanf("%s", imfout);
if((out_ptr = fopen(imfout, "w")) == NULL)
{
        printf("***  Unable to write output file %s ***\n", imfout);
        exit(0);
}

printf("Calculating optimized physical IMF ...\n");

  /* initialization */

  add = 0.0;
  tot[bin] = 0.0;

/**  Profile calculation (on mm grid) using semiempirical model  **/

for(bin = 1; bin <= 200; bin++) {
           scat[bin] = 0.0;
        for(i = 1; i <= 200; i++) {
                if(bin == 1) {
                        scat[bin] = scat[bin] + xvan[i]*sn[i]*foar[i];
                }
                else {
                        if(i < bin) {
                                j = bin - i + 1;
                        }
                        else {
                                j = i - bin + 1;
                        }
                        scat[bin] = scat[bin] + xvan[i]*sn[j]*foar[i];

                }

                tot[bin] = 84.6*xvan[bin]*foar[bin] + scat[bin];
```

```
            }

                                add = add + SQ(fimf[bin] - tot[bin]);
                                lbin = ((float)bin - 101.0);
                                rbin = ((float)bin - 100.0);

        /* Define and open output IMF file suitable for XY AVS file */

                        fprintf(out_ptr,"%.2f  %.4f\n%.2f  %.4f\n", lbin, tot[bin], rbin,
tot[bin]);
    }
      fclose(out_ptr);
      printf("add = %.4f\n", add);
return;
}

/*************************************************************************/
/*                              dose_calc                                */
/*  This subroutine performs 2d dose calculation using previously calculated    */
/*                      IMF and measured TMR and OAR data.               */
/*************************************************************************/

void dose_calc()
{
char imfile[15], dosout[15];
FILE *dout_ptr;
FILE *tmr_ptr;
float inv_sq, d_prime, r, r_prime, fs, nz, oad, d_max;
float tmr[500], dose[500][500], imf_prime[500][500], d_norm[500][500];
int i, j, k, d, oad_prime, nz_new, fs_new;

        /*  Open tissue-maximum ratio file  */
        if((tmr_ptr = fopen("tmr.prn", "r")) == NULL)
        {
                printf("***  Unable to open tmr file  ***");
                exit(0);
        }
        for(i = 0; i <= 215; i++){
                fscanf(tmr_ptr, "%f", &tmr[i]);
        }
        fclose(tmr_ptr);

       printf("\n Enter 2d dose file name:\n");
          scanf("%s", dosout);
        if((dout_ptr = fopen(dosout, "w")) == NULL)
        {
                printf("***  Unable to open output file %s ***\n", dosout);
                exit(0);
        }
        printf("Calculating 2d dose distribution ...\n");

                /* Dose calculation using semiempirical model.  */
        d_max = 0.0;
        for(d = 0; d< =215; d+ +){
                for(j = 1; j< = 200; j+ +){
                        r = (float)j;
                        d_prime = (float)d/(cos(atan((0.1*r)/SAD)));
                        inv_sq = SQ(SAD*10)/(SQ(SSD*10 + d));
                        dose[d][j] = tmr[d]*tot[j]*inv_sq;
                        if(dose[d][j] > d_max){
                                d_max = dose[d][j];
                        }
                }
        }
        printf("d_max = %.2f\n", d_max);

      /* normalize data and create output file suitable for uniform AVS field */

        for(d = 0; d< =215; d+ +){
                for(j = 1; j< = 200; j+ +){
                        d_norm[d][j] = 100*dose[d][j]/d_max;
                        r_prime = j - 100.5;
                        oad = r_prime*(SSD+d/10.0)/SAD;
                        d_prime = fabs((double)d - 215);
                        fprintf(dout_ptr,"%.1f      %.2f      %.2f\n",   d_prime,   oad,
d_norm[d][j]);
                }
        }
        fclose(dout_ptr);

}
```

REFERENCES

Arm93 J. Armstrong, C. Burman, S. Leibel, D. Fontenla, G. Kutcher, M. Zelefsky, Z. Fuks, "Three-Dimensional Conformal Radiation Therapy May Improve the Therapeutic Ratio of High Dose Radiation Therapy for Lung Cancer," Int. J. Radiation Oncology Biol. Phys. 26:685 (1993)

Arr93 R. Arriagada, H. Mouriesse, A. Rezvani, D. Sarrazin, R. Clark, G. DeBoer, R. Bush, "Radiotherapy Alone in Breast Cancer. Analysis of Tumor and Lymph Node Radiation Doses and Treatment-related Complications," Radiotherapy and Oncology 27:1 (1993)

Bar90 N. Barth, "An Inverse Problem in Radiation Therapy," Int. J. Radiation Biol. Phys. 18:425 (1990)

Boh86 I. Bohachevsky, M. Johnson, M. Stein, "Generalized Simulated Annealing for Function Optimization," Technometrics 28(3):209 (1986)

Bor90 T. Bortfeld, J. Burkelbach, R. Boesecke, W. Schlegel, "Methods of Image Reconstruction From Projections Applied to Conformation Radiotherapy," Phys. Med. Biol. 35:1423 (1990)

Bov90 F. J. Bova, "Radiation Physics," Neurosurgery Clinics of North America 1(4):909 (1990)

Bov91 F. J. Bova, W. A. Friedman, "Stereotactic Angiography: An Inadequate Database for Radiosurgery?" Int. J. Radiation Oncology Biol. Phys. 20:891 (1991)

Bov93 F. J. Bova, W. A. Friedman, W. Mendenhall, "Stereotactic Radiosurgery," Medical Progress through Technology 18:239 (1993)

Bra82 A. Brahme, J. E. Roos, I. Lax, "Solution of an Integral Equation Encountered in Rotation Therapy," Phys. Med. Biol. 27:1221 (1982)

Bra84 A. Brahme, "Dosimetric Precision Requirements in Radiation Therapy," Acta Radiologica Oncology 23:379 (1984)

Bra87 A. Brahme, A. Agren, "Optimal Dose Distribution for Eradication of Heterogeneous Tumors," Acta Oncologica 26:377 (1987)

Bra88 A. Brahme, "Optimization of Stationary and Moving Beam Radiation Therapy Techniques," Radiotherapy and Oncology 12:129 (1988)

Bro91 A. Brown, M. Urie, G. Barest, E. Cheng, L. Coia, N. Emami, J. Galvin, J. Kutcher, J. Manolis, J. Wong, J. Yahalom, "Three-Dimensional Treatment Planning for Hodgkin's Disease," Int. J. Radiation Oncology Biol. Phys. 21:205 (1991)

Coi91 L. Coia, J. Galvin, M. Sontag, P. Blitzer, H. Brenner, E. Cheng, K. Doppke, W. Harms, M. Hunt, R. Mohan, J. Munzenrider, J. Simpson, "Three-Dimensional Treatment Planning in Carcinoma of the Larynx," Int. J. Radiation Oncology Biol. Phys. 21:183 (1991)

Cor87a A. Cormack, "A Problem in Rotation Therapy With X Rays," Int. J. Radiation Oncology Biol. Phys. 13:623 (1987)

Cor87b A. Cormack, R. Cormack, "A Problem in Rotation Therapy With X Rays: Dose Distributions With and Axis of Symmetry," Int. J. Radiation Oncology Biol. Phys. 13:1921 (1987)

Cun72 J. R. Cunningham, "Scatter-Air Ratios," Phys. Med. Biol. 17:42 (1972)

Drz91 R. Drzymala, R. Mohan, L. Brewster, J. Chu, M. Goitein, W. Harms, M. Urie, "Dose-Volume Histograms," Int. J. Radiation Oncology Biol. Phys. 21:71 (1991)

Ema91a B. Emami, J. Lyman, A. Brown, L. Coia, M. Goitein, J. Munzenrider, B. Shank, L. Solin, M. Wesson, "Tolerance of Normal Tissue to Therapeutic Irradiation," Int. J. Radiation Oncology Biol. Phys. 21:109 (1991)

Ema91b B. Emami, J. Purdy, J. Manolis, G. Barest, E. Cheng, L. Coia, K. Doppke, J. Galvin, T. LoSasso, J. Matthews, J. Munzenrider, B. Shank, "Three-Dimensional Treatment Planning for Lung Cancer," Int. J. Radiation Oncology Biol. Phys. 21:217 (1991)

Fli90 J. Flickenger, M. Schell, D. Larson, "Estimation of Complications for Linear Accelerator Radiosurgery with the Integrated Logistic Function," Int. J. Radiation Oncology Biol. Phys. 19:143 (1989)

Fri89 W. A. Friedman, F. J. Bova, "The University of Florida Radiosurgery System," Surg. Neurol. 32:334 (1989)

Fri92 W. A. Friedman, F. J. Bova, R. Spiegalmann, "Linear Accelerator Radiosurgery at the University of Florida," Neurosurgery Clinics of North America 3(1):141 (1992)

Goi83 M. Goitein, M. Abrams, D. Rowell, H. Pollani, J. Wiles, "Multi- Dimensional Treatment Planning: II. Beam's Eye-View, Backprojection, and Projection Through CT Sections," Int. J. Radiation Oncology Biol. Phys. 9:789 (1983)

Goi86 M. Goitein, "Causes and Consquences of Inhomogeneous Dose Distributions in Radiation Therapy," Int. J. Radiation Oncology Biol. Phys. 12:701 (1986)

Goi88 M. Goitein, "Planning Radiation Therapy," in Clinical Radiation Therapy, ed. C. Wang, PSG Publishing Company, Littleton, MA 1988.

Goi90 M. Goiten, "The Inverse Problem," Int. J. Radiation Oncology Biol. Phys. 18:489 (1990)

Goi94 M. Goitein, A. Niemeirko, P. Okunieff, "The Probability of Controlling an Inhomogeneously Irradiated Tumor," Submitted to Int. J. Radiation Oncology Biol. Phys. (1994)

Gra94 W. Grant,"Validation of a Beam-Modeling Algorithm for a 3D Conforomal Theray System Using a Multi-Leaf Collimator for Intensity Modulation," Abstract, Med. Phys. 21(6):946 (1994)

Har94 J. Harmon, "Inverse Radiotherapy Treatment Planning Through Deconvolution and Constrained Optimization," Ph. D. Dissertation, University of Florida (1994)

Hol94 T. Holmes, T. Mackie, "A Filtered Backprojection Dose Calculation Method for Inverse Treatment Planning," Med. Phys. 21:303 (1994)

Hun93a M. Hunt, G. Kutcher, C. Burman, D. Fass, L. Harrison, S. Leibel, Z. Fuks, "The Effect of Setup Uncertainties on the Treatment of Nasopharynx Cancer", Int. J. Radiation Oncology Biol. Phys. 27:437 (1993)

Hun93b M. Hunt, T. Schultheiss, G. Desobry, G. Hanks, "Convolving Setup Uncertainties With Dose Distributions", Abstract, Med. Phys. 20(3):929 (1993)

Jac93 A. Jackson, G. Kutcher, E. Yorke, "Probability of Radiation-Induced Complications for Normal Tissues with Parallel Architecture Subject to Non-Uniform Irradiation," Med. Phys. 20(3):613 (1993)

Joh83 H. Johns, J. Cunningham, The Physics of Radiology, Fourth Edition, Charles C. Thomas, Springfield, IL (1983)

Kal92 P. Kallman, B. Lind, A. Brahme, "An Algorithm for Maximizing the Probability of Complication-Free Tumour Control in Radiation Therapy," Phys. Med. Biol. 37(4):871 (1992)

Kaw75 I. Kawachi, "Calculation of Electron Dose Distribution for Radiotherapy Treatment Planning," Phys. Med. Biol. 20(4):571 (1975)

Kha84 F. M. Khan, The Physics of Radiation Therapy, Williams and Wilkins, New York (1984)

Kje83 R. Kjellberg, K. Davis, S. Lysons, W. Batler, R. Adams, "Bragg Peak Proton Beam Therapy for Arteriovenous Malformations of the Brain," Clin. Neurosurg. 31:248 (1983)

Koo90 H. Kooy, "The Verification of an Inverse Problem in Radiation Therapy," Int. J. Radiation Oncology Biol. Phys. 18:433 (1990)

Kuc91 F. T. Kuchnir, S. Watson-Bullock, C. S. Reft, D. Hallahan, "3-D Treatment Planning and Dose Delivery Verification Integrating a Variety of State of the Art Techniques: A Case Report," Med. Dosimetry 16:225 (1991)

Kut91a G. Kutcher, C. Burman, L. Brewster, M. Goitein, R. Mohan, "Histogram Reduction Method for Calculating Complication Probabilities for Three-Dimensional Treatment Planning Evaluations," Int. J. Radiation Oncology Biol. Phys. 21:137 (1991)

Kut91b G. Kutcher, Z. Fuks, H. Brenner, A. Brown, C. Burman, E. Cheng, L. Coia, K. Krippner, J. Manolis, R. Mohan, J. Simpson, M. Urie, B. Vikram, R. Wallace, "Three-Dimensional Treamtent Planning for Carcinoma of the Nasopharynx," Int. J. Radiation Oncology Biol. Phys. 21:169 (1991)

Kut92 G. Kutcher, "Quantitative Plan Evaluation," in Advances in Radiation Oncology Physics: Dosimetry, Treatment Planning and Brachytherapy, ed. J. Purdy, AIP Press, Woodbury, New York (1992)

Lea91 D. Leavitt, F. Gibbs Jr., M. Heilbrun, J. Moeller, G. Takach Jr., "Dynamic Field Shaping to Optimize Stereotactic Radiosurgery," Int. J. Radiation Oncology Biol. Phys. 21:1247 (1991)

Lei91 S. Leibel, C. Ling, G. Kutcher, R. Mohan, C. Cordon-Cordo, Z. Fuks, "The Biological Basis for Conformal Three-Dimensional Radiation Therapy," Int. J. Radiation Oncology Biol. Phys. 21:805 (1991)

Lek51 L. Leksell, "The Stereotactic Method and Radiosurgery of the Brain," Acta Chir. Scand. 102:316 (1951)

Lek83 L. Leksell, "Stereotactic Radiosurgery," Journal of Neurology, Neurosurgery, and Psychiatry 46:797 (1983)

Lek87 D. Leksell, Stereotactic Radiosurgery: Present Status and Future Trends," Neurological Research 9:60 (1987)

Leo87 J. Leong, "Implementation of Random Positioning Error in Computerised Radiation Treatment Planning Systems as a Result of Fractionation", Phys. Med. Biol. 32(3):327 (1987)

Lim89 E. Limbergen, A. Rijnders, E. Schueren, T. Lerut, R. Christiaens, "Cosmetic Evaluation of Breast Conserving Treatment of Mammary Cancer. 2. A Quantitative Analysis of the Influence of Radiation Dose, Fractionation Schedules and Surgical Treatment Techniques on Cosmetic Results," Radiotherapy and Oncology 16:253 (1989)

Lin93 B. Lind, P. Kallman, B. Sundelin, A. Brahme, "Optimal Radiation Beam Profiles Considering Uncertainties in Beam Patient Alignment", Acta Oncologica 32(3):331 (1993)

LoS93 T. LoSasso, C. Chui, G. Kutcher, S. Leibel, Z. Fuks, C. Ling, "The Use of a Multi-Leaf Collimator for Conformal Radiotherapy of Carcinomas of the Prostate and Nasopharynx," Int. J. Radiation Oncology Biol. Phys. 25:161 (1993)

Lut88 W. Lutz, K. Winston, N. Maleki, "A System for Stereotactic Radiosurgery With a Linear Accelerator," Int. J. Radiation Oncology Biol. Phys. 14:373 (1988)

Lux91 G. Luxton, G. Jozsef, M. Astrahan, "Algorithm for Dosimetry of Multiarc Linear Accelerator Stereotactic Radiosurgery," Med. Phys. 18(6):1211 (1991)

Lym85 J. Lyman, "Complication Probability as Assessed From Dose-Volume Histograms," Radiation Research 104:S-13 (1985)

Mac93 T. Mackie, T. Holmes, S. Swerdloff, P. Rockwendt, J. Deasy, J. Yang. B. Paliwal, T. Kinsella, "Tomotherapy: A New Concept for the Delivery of Dynamic Conformal Radiotherapy," Med. Phys. 20:1709 (1993)

McG92 P. McGinley, E. Butker, I. Crocker, R. Aiken, "An Adjustable Collimator for Stereotactic Radiosurgery," Phys. Med. Biol. 37(2):413 (1992)

Moh92 R. Mohan, G. Mageras, B. Baldwin, L. Brewster, G. Kutcher, S. Leibel, C. Burman, C. Ling, Z. Fuks, "Clinically Relevant Optimization of 3-D Conformal Treatments," Med. Phys. 19(4):933 (1992)

Mos92 D. C. Moss, "Conformal Stereotactic Radiosurgery With a Multileaf Collimator," Ph. D. Dissertation, University of Florida (1992)

Mun91a J. Munzenrider, A. Brown, J. Chu, L. Coia, K. Doppke, B. Emami, G. Kutcher, R. Mohan, J. Purdy, B. Shank, J. Simpson, L. Solin, M. Urie, " Numerical Scoring of Treatment Plans," Int. J. Radiation Oncology Biol. Phys. 21:147 (1991)

Mun91b J. Munzenrider, K. Doppke, A. Brown, C. Burman, E. Cheng, J. Chu, C. Chui, R. Drzymala, M. Goitein, J. Manolis, D. Nori, J. Simpson, L. Solin, M. Urie, "Three-Dimensional Treatment Planning for Para-Aortic Node Irradiation in Patients with Cervical Cancer," Int. J. Radiation Oncology Biol. Phys. 21:229 (1991)

Ned91 L. Nedzi, H. Kooy, E. Alexander, R. Gelman, J. Loeffler, "Variables Associated With the Development of Complications From Radiosurgery of Intracranial Tumors," Int. J. Radiation Oncology Biol. Phys. 21:591 (1991)

Ned92 L. Nedzi, H. Kooy, E. Alexander, G. Svensson, J. Loeffler, "Dynamic Field Shaping for Stereotactic Radiosurgery: A Modeling Study," Int. J. Radiation Oncology Biol. Phys. 25(5):859 (1992)

Nie91 A. Niemierko, B. Maciejewski, "Biologically Normalized Dose-Volume Histograms (BNDVHs)," Abstract, Med. Phys. 18(3):628 (1991)

Nie92 A. Niemierko, "Random Search Algorithm (RONSC) for Optimization of Radiation Therapy With Both Physical and Biological End Points and Constraints," Int. J. Radiation Oncology Biol. Phys. 23:89 (1992)

Nie93 A. Niemierko, M. Goitein, "Implementation of a Model for Estimating Tumor Control Probability for an Inhomogeneously Irradiated Tumor," Radiotherapy and Oncology 29(2):140 (1993)

Niz93 P. Nizin, G. Qian, H. Rashid, ""Zero-Field Dose Data for ^{60}Co and other High-energy Photon Beams in Water", Med. Phys. 20(5):1353 (1993)

Nom94 Nomos corporation, Peacock Plan™ Operator's Manual, Version 1, Nomos Corporation, Sewickley, PA (1994)

Oku93 P. Okunieff, M. Hoeckel, E. Dunphy, K. Schlenger, C. Knoop, P. Vaupel, "Oxygen Tension Distributions are Sufficient to Explain the Local Response of Human Breast Tumors Treated with Radiation Alone", Int. J. Radiation Oncology Biol. Phys. 26:631 (1993)

Par94 J. Parsons, "The Effect of Radiation on Normal Tissues of the Head and Neck," in Management of Head and Neck Cancer: A Multidisciplinary Approach, Second Edition, ed. R. Million and N. Cassisi, J.B. Lippincott Company, Philadelphia (1994)

Per92 C. Perez, L. Brady, Principles and Practice of Radiation Oncology 2nd Edition, J.B. Lippincott Company, Philadelphia (1992)

Pik90 G. Pike, E. Podgorsak, T. Peters, C. Pla, A. Olivier, L. Souhami, "Dose Distributions in Radiosurgery," Med. Phys. 17(2):296 (1990)

Pre91 W.H. Press, B.P. Flannery, S.A. Teukolsky, W.T. Vetterling, Numerical Recipes in C, Cambridge University Press, Cambridge U.K. (1991)

San91 H. Sandler, D. McShan, A. Lichter, Potential Improvement in the Results of Irradiation for Prostate Carcinoma Using Improved Dose Distribution," Int. J. Radiation Oncology Biol. Phys. 22:361 (1991)

Saw87 C. Saw, K. Ayyangar, N. Suntharalingam, "Coordinate Transformations and Calculation of the Angular and Depth Parameters for a Stereotactic System," Med. Phys. 14:1042 (1987)

Sch85 T. Schultheiss, C. Orton, "Models in Radiotherapy: Definition of Decision Criteria," Med. Phys. 12(2):183 (1985)

Sha91a S. Shalev, D. Viggars, M. Carey, P. Hahn, "The Objective Evaluation of Alternative Treatment Plans: II. Score Functions," Int. J. Radiation Oncology Biol. Phys. 20:1067 (1991)

Sha91b B. Shank, T. LoSasso, L. Brewster, C. Burman, E. Cheng, J. Chu, R. Drzymala, J. Manolis, M. Pilepich, L. Solin, J. Tepper, M. Urie, "Three-Dimensional Treatment Planning for Postoperative Treatment of Rectal Carcinoma," Int. J. Radiation Oncology Biol. Phys. 21:253 (1991)

She87 G. Sherouse, C. Mosher, K. Novins, J. Rosenman. E. Cheney, "Virtual Simulation: Concept and Implementation," The Use of Computers in Radiation Therapy, ed. I. Bruinvis, Elsevier Science Publishers, Holland (1987)

Sim91 J. Simpson, J. Purdy, J. Manolis, M. Pilepich, C. Burman, J. Forman, Z. Fuks, E. Cheng, J. Chu, J. Matthews, R. Mohan, L. Solin, M. Urie, "Three-Dimensional Treatment Planning Considerations for Prostate Cancer," Int. J. Radiation Oncology Biol. Phys. 21:243 (1991)

Smi91 A. Smith, J. Purdy, et al., "Evaluation of High Energy Photon External Beam Treatment Planning: Project Summary," Int. J. Radiation Oncology Biol. Phys. 21:3 (1991)

Sof92 E. Soffen, G. Hanks, M. Hunt, B. Epstein, "Conformal Static Field Radiation Therapy Treatment of Early Prostate Cancer Versus Non-Conformal Techniques: A Reduction of Acute Morbidity," Int. J. Radiation Oncology Biol. Phys. 24:485 (1992)

Sol91 L. Solin, J. Chu, M. Sontag, L. Brewster, E. Cheng, K. Doppke, R. Drzylama, M. Hunt, R. Kuske, J. Manolis, B. McCormick, J. Munzenrider, "Three-Dimensional Photon Treatment Planning of the Intact Breast," Int. J. Radiation Oncology Biol. Phys. 21:193 (1991)

Spi92 R. Spiegalmann, W. A. Friedman, F. J. Bova, "Limitations of Angiographic Target Localization in Planning Radiosurgical Treatment," Neurosurgery 30(4):619 (1992)

Suh90 T. S. Suh, "Optimization of Dose Distributions for System of Linac Based Stereotactic Radiosurgery," PhD Dissertation, University of Florida (1990)

Sui92 H. Suit, S. Skates, A. Taghian, P. Okunieff, J. Efird, "Clinical Implications of Heterogeneity of Tumor Response to Radiation Therapy", Radiotherapy and Oncology 25:251 (1992)

Tha91 H. Thames, T. Schultheiss, J. Hendry, S. Tucker, B. Dubray, W. Brock, "Can Modest Escalations of Dose be Detected as Increased Tumor Control?", Int. J. Radiation Oncology Biol. Phys. 22:241 (1991)

The90 Theratronics, "TP-11/Theraplan User's Manual," Volume 2 Edition 9 (1990)

Van93 J. VanDyk, R. Barnett, J. Cygler, P. Shragge, "Commissioning and Quality Assurance of Treatment Planning Computers", Int. J. Radiation Oncology Biol. Phys. 26:261 (1993)

Vij93 S. Vijayakumar, A. Awan, T. Karrison, H. Culbert, S. Chan, J. Kolker, N. Low, H. Halpern, S. Rubin, G. Chen, R. Weichselbaum, " Acute Toxicity During External Beam Radiotherpy for Localized Prostate Cancer: Comparison of Different Techniques," Int. J. Radiation Oncology Biol. Phys. 25:359 (1993)

Wal88 R. Walker, Radiation in Illinois: A Chronology of Selected Events, 1700-1980, Illinois Department of Nuclear Safety, Chicago (1988)

Web89 S. Webb, "Optimisation of Conformal Radiotherapy Dose Distributions by Simulated Annealing," Phys. Med. Biol. 34(10):1349 (1989)

Web91a S. Webb, "Optimization by Simulated Annealing of Three-Dimensional Conformal Treatment Planning for Radiation Fields Defined by a Mulitleaf Collimator", Phys. Med. Biol. 36(9):1201 (1991)

Web91b S. Webb, "Optimization of Conformal Therapy Dose Distributions by Simulated Annealing: 2. Inclusion of Scatter in the 2D Technique", Phys. Med. Biol. 36(9):1227 (1991)

Web92 S. Webb, "Optimization by Simulated Annealing of Three Dimensional, Conformal Treatment Planning for Radiation Fields Defined by a Multileaf Collimator: II. Inclusion of Two-dimensional Modulation of the X-Ray Intensity," Phys. Med. Biol. 37(8):1689 (1992)

Win88 K. Winston, W. Lutz, "Linear Accelerator as a Neurosurgical Tool for Stereotactic Radiosurgery," Neurosurgery 22:454 (1988)

Wit83 H. Withers, H. Thames, L. Peters, "A New Isoeffect Curve for Change in Dose per Fraction," Radiotherapy and Oncology 1:187 (1983)

Woo93 S. Woo, W. Grant, D. Bellazza, R. Grossman, P. Gildenberg, S. Carpenter, M. Carol, E. Butler, "A Comparison of Optimized Conformal Therapy With a Standard External Beam Stereotactic Radiosurgery System for the Treatment of Single and Multiple Intracranial Lesions," Abstract, Int. J. Radiation Oncology Biol. Phys. (1993)

Yan94 C. Yang, "High Precision Treatment for Fractionated Stereotactic Radiotherapy", PhD Dissertation, University of Florida (1994)

Yeu94 D. Yeung, J. Palta, J. Fontanesi, L. Kun, "Systematic Analysis of Errors in Target Localization and Treatment Delivery in Stereotactic Radiosurgery (SRS)", Int. J. Radiation Oncology Biol. Phys. 28:493 (1994)

BIOGRAPHICAL SKETCH

Sanford Lee Meeks was born on May 17, 1968, in Lakeland, Florida. He graduated magna cum laude from Florida Southern College with a Bachelor of Science degree in physics in 1989. He then attended Florida State University, where he obtained a Master of Science degree in physics in 1991. While at Florida State University, he served as a Research Assistant studying the properties of high T_c ceramic superconducting materials. He enrolled in the medical physics program of the University of Florida in August of 1991, and has been pursuing the degree of Doctor of Philosophy since that time. During his stay at the University of Florida, he has been involved in clinical therapy physics and assisted with the Stereotactic Radiosurgery Program at Shands Cancer Center. He is a member of ΣΠΣ (the physics national honor society), ΑΝΣ (the nuclear science national honor society) and ΚΜΕ (the mathematics national honor society) and a student member of the American Association of Physicists in Medicine. He is married to Allyson Thompson Meeks, and their first child, Sanford Alton Meeks, was born April 5, 1994.

I certify that I have read this study and that in my opinion it conforms to acceptable standards of scholarly presentation and is fully adequate, in scope and quality, as a dissertation for the degree of Doctor of Philosophy.

Frank J. Bova, Chair
Professor of Nuclear Engineering Sciences

I certify that I have read this study and that in my opinion it conforms to acceptable standards of scholarly presentation and is fully adequate, in scope and quality, as a dissertation for the degree of Doctor of Philosophy.

G. Ronald Dalton

George R. Dalton
Professor of Nuclear Engineering Sciences

I certify that I have read this study and that in my opinion it conforms to acceptable standards of scholarly presentation and is fully adequate, in scope and quality, as a dissertation for the degree of Doctor of Philosophy.

David E. Hintenlang
Associate Professor of Nuclear Engineering Sciences

I certify that I have read this study and that in my opinion it conforms to acceptable standards of scholarly presentation and is fully adequate, in scope and quality, as a dissertation for the degree of Doctor of Philosophy.

Carl D. Crane
Associate Professor of Mechanical Engineering

I certify that I have read this study and that in my opinion it conforms to acceptable standards of scholarly presentation and is fully adequate, in scope and quality, as a dissertation for the degree of Doctor of Philosophy.

William A. Friedman

William A. Friedman
Professor of Neuroscience

This dissertation was submitted to the Graduate Faculty of the College of Engineering and to the Graduate School and was accepted as partial fulfillment of the requirements for the degree of Doctor of Philosophy.

December 1994

fr

Winfred M. Phillips
Dean, College of Engineering

Karen A. Holbrook
Dean, Graduate School